Volume 18
Number 10
21 May 2025
Pages 4483–5010

Energy & Environmental Science

rsc.li/ees

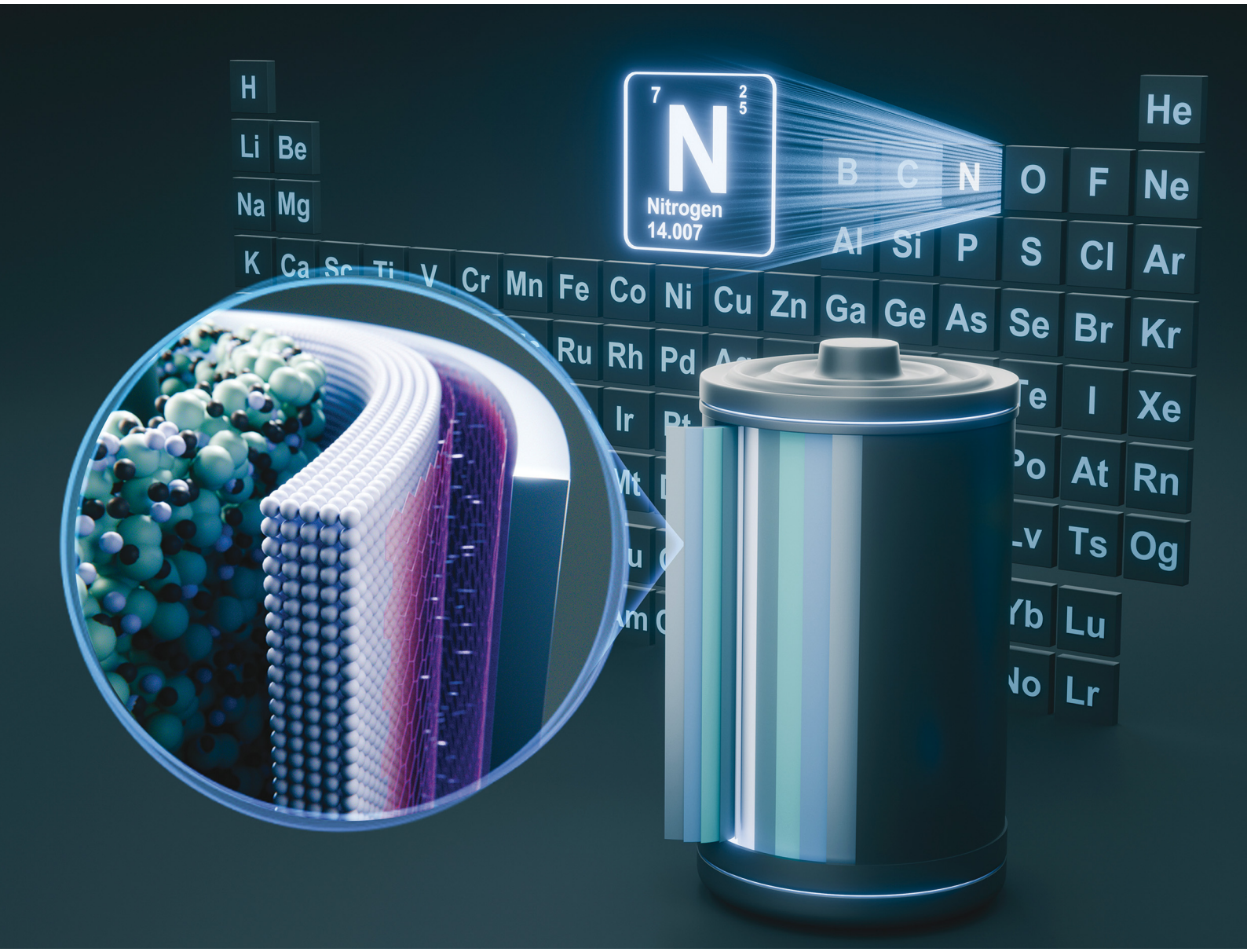

ISSN 1754-5706

ROYAL SOCIETY OF CHEMISTRY

REVIEW ARTICLE
Tsun-Kong Sham, Xueliang Sun *et al.*
Nitride solid-state electrolytes for all-solid-state lithium metal batteries

Energy & Environmental Science

ROYAL SOCIETY OF CHEMISTRY

REVIEW

View Article Online
View Journal | View Issue

Cite this: *Energy Environ. Sci.*, 2025, **18**, 4521

Nitride solid-state electrolytes for all-solid-state lithium metal batteries

Weihan Li,†[acd] Minsi Li,†[bcd] Haoqi Ren,†[c] Jung Tae Kim,[c] Ruying Li,[c] Tsun-Kong Sham*[d] and Xueliang Sun*[ac]

Received 23rd October 2024,
Accepted 24th February 2025

DOI: 10.1039/d4ee04927f

rsc.li/ees

Nitride solid-state electrolytes (SSEs) hold significant potential for addressing critical interfacial issues between SSEs and lithium metal in all-solid-state lithium metal batteries. These batteries are at the forefront of energy storage and materials science, and they promise to revolutionize electric vehicles. This review provides a concise historical overview of nitride SSEs, followed by a summary of recent key advances in their materials, crystal and local structures, and synthesis methods, with an emphasis on the fundamental understanding of lithium-ion diffusion mechanisms. Additionally, recent progress in enhancing the stability of nitride SSEs and their role in enabling all-solid-state lithium metal batteries is discussed in detail. Pathways for the development of practical all-solid-state lithium metal pouch cells with high energy density are explored. Based on these insights, we offer perspectives on the future opportunities and directions for the advancement of nitride SSEs in all-solid-state lithium metal batteries.

Broader context

The transition to sustainable energy hinges on advanced storage technologies, with all-solid-state lithium metal batteries (ASSLMBs) at the forefront. Promising high energy density, safety, and long cycle life, ASSLMBs are pivotal for applications such as electric vehicles (EVs). However, interfacial challenges between lithium metal and solid-state electrolytes (SSEs), including instability, dendrite growth, and insufficient ionic conductivity, remain significant barriers. Nitride-based SSEs offer a compelling solution due to their inherent stability with lithium metal, mechanical toughness, and potential for high ionic conductivity. Recent advancements include vacancy-rich structures and optimized anion frameworks, enabling superior ionic transport and interfacial stability. Progress in scalable synthesis methods, such as ball-milling and thin-film deposition, also positions nitride SSEs as practical candidates for high-energy-density ASSLMBs. These developments could revolutionize EVs by enabling extended ranges, safer operation, and rapid charging, while contributing to decarbonized transportation. By addressing long-standing interfacial challenges, nitride SSEs accelerate the path toward practical ASSLMBs, closing the gap between laboratory innovation and real-world application. This review integrates the latest insights into nitride SSEs, offering a roadmap for future research and development to unlock their full potential in next-generation energy storage systems.

1. Introduction

Rechargeable lithium batteries power our daily lives.[1] The projected exponential growth of the electric vehicle (EV) and grid energy storage markets necessitates advancements in rechargeable lithium batteries, particularly in achieving high energy density, high power density, and long cycling life.[2,3] One crucial goal is to achieve specific energy densities exceeding 350 W h kg^{-1} and potentially reaching up to 500 W h kg^{-1}, which requires the adoption of lithium metal anodes to replace the carbon and silicon anodes used in conventional rechargeable lithium-ion batteries (generations 1 and 2, with energy densities of approximately 125–280 W h kg^{-1} and 320–350 W h kg^{-1}, respectively) (see Fig. 1A).[4] However, similar to the previously commercialized TiS_2-lithium metal batteries (generation 0, see Fig. 1A), lithium–metal batteries with flammable non-aqueous electrolytes often suffer from rapid capacity fading and thermal runaway due to lithium dendrite growth and penetration through separators, leading to serious safety issues and potential fires in organic electrolytes and batteries.[5]

The emerging all-solid-state lithium metal batteries offer new opportunities by using solid-state electrolytes (SSEs) for thin lithium metal anodes, which can address capacity fading

[a] *Ningbo Key Laboratory of All-Solid-State Battery, Eastern Institute for Advanced Study, Eastern Institute of Technology, Ningbo, Zhejiang 315201, China. E-mail: xsun9@uwo.ca*
[b] *Institute of Micro/Nano Materials and Devices, Ningbo University of Technology, Ningbo, Zhejiang 315211, China*
[c] *Department of Mechanical and Materials Engineering, Western University, London, Ontario N6A 5B9, Canada. Tel: +1-519-661-2111 Ext 87759*
[d] *Department of Chemistry and Soochow-Western Centre for Synchrotron Radiation Research, Western University, London, Ontario N6A 5B7, Canada. E-mail: tsham@uwo.ca; Tel: +1-519-661-2111 Ext 86341*
† These authors contributed equally to this work.

and safety issues while meeting the increasing demand for higher energy and safety in rechargeable lithium batteries (see Fig. 1A). However, the research and development of all-solid-state lithium metal batteries face significant challenges at the lithium metal–SSE interfaces.[6–8] As shown in Fig. 1B, unstable interfaces increase interfacial resistance and consume lithium metal, leading to rapid electrochemical performance fading. Uneven lithium stripping and plating leaves voids in lithium metal and increase contact resistance, which also promotes forming lithium dendrites in SSEs. The continuous growth of lithium dendrites in SSEs and lithium nucleation along with grain boundaries can induce internal short circuits and serious safety issues. These interfacial challenges are mainly due to unstable characteristics of most SSEs towards lithium metal, including fluorides, halides, bromides, iodides, oxides, and sulfides (see Fig. 2A). The solution lies on formation of stable, compatible interfaces[9–11] or developing lithium-compatible SSE layers to stabilize lithium metal anodes.[12] Compared to other SSEs, nitride-based electrolytes exhibit thermodynamic stability against lithium metal, making them promising candidates for resolving lithium metal–SSE interfacial challenges. However, nitrides face limitations in their stability with cathode materials and still require further improvement in ionic conductivity to match their sulfide and halide counterparts. Despite these challenges, nitride SSEs remain strong candidates to overcome the interfacial issues in lithium metal batteries, offering potential as an ultimate solution.[13]

Recent advancements in nitride SSEs have demonstrated their capability to prevent severe interfacial reactions with lithium metal anodes and overcome lithium dendrite growth challenges. Practically viable all-solid-state lithium metal batteries with nitride SSEs have been shown to exhibit long cycling life, high areal capacity, and fast charging.[15–18] Given the promising application potential of nitrides in high-energy-density all-solid-state lithium metal batteries, research and development in this area are attracting increasing interest. This review aims to provide an overview of the fundamentals and research history of nitride SSEs, and to summarize recent key progress in materials, structures,

Weihan Li

Weihan Li: He is an Assistant Professor at the Eastern Institute of Technology, Ningbo. He earned his Bachelor's degree from Sichuan University in 2011 and completed his dual PhD degrees at the University of Science and Technology of China (2016) and Western University, Canada (2023). He has undertaken postdoctoral research at Western University and visiting research at the Canadian Light Source. His research interests include the fundamental and applied studies of solid-state batteries, lithium-ion and sodium-ion batteries, and advanced synchrotron-based characterization techniques.

Minsi Li

Minsi Li: She is a Professor at Ningbo University of Technology, China, where her research focuses on synchrotron-based characterization techniques and the development of advanced materials for solid-state batteries. She earned her Bachelor's degree in 2016 from the University of Science and Technology of China and completed her PhD at Western University, Canada, in 2021. Following her doctoral studies, she conducted postdoctoral research at Western University and visiting research at the Canadian Light Source.

Haoqi Ren

Haoqi Ren: He is a PhD candidate in Prof. Xueliang Sun's research group at Western University, Canada. He earned his MS degree from Boston University and his BSc from Fudan University. His research focuses on interface design between anodes and solid electrolytes in all-solid-state batteries.

Jung Tae Kim

Jung Tae Kim: He is currently a PhD candidate in Prof. Yuzhang Li's group at the University of California, Los Angeles. He received his BSc from the University of British Columbia in 2021 and MS from the Western University in 2023 under the supervision of Prof. Xueliang Sun. His research interests include the development of all-solid-state Li–S batteries, Li metal batteries, and cryogenic transmission electron microscopy.

synthesis methods, stability, characterization techniques, and the development of all-solid-state lithium metal batteries. Our objective is to highlight ongoing innovations and breakthroughs in nitride SSEs, to inspire future research and development, and to promote the advancement of all-solid-state lithium metal batteries.

2. Categorizing and comparing nitride solid-state electrolytes

Fig. 2B illustrates the research history of nitride SSEs, which began in 1935 with the proposed crystal structure of α-Li_3N.[19] Since the first report on Li_3N SSEs in 1957,[20] a significant number of nitride SSEs have been developed and studied. Over the decades, significant advancements have been made to overcome the limitations of early materials, such as low ionic conductivity, limited electrochemical stability windows, and poor compatibility with lithium metal. The strategies for improving nitride SSEs have focused on the following key aspects:

(a) Improving ionic conductivity:

Initial efforts centered on understanding lithium-ion conduction in α-Li_3N, which exhibited anisotropic ionic conductivity. Advanced characterizations revealed the critical role of vacancy formation and distribution in facilitating fast lithium-ion diffusion. Subsequent research on LiPON introduced chemical doping (*e.g.*, with Si, B, and metallic elements) to improve ionic conductivity while maintaining mechanical and electrochemical stability. More recently, materials such as lithium nitride halides and nitridophosphates have been developed, leveraging tailored anion frameworks and increased vacancy populations to achieve further improvement in ionic conductivity.

(b) Widening electrochemical stability windows:

Research has also focused on designing nitride-based SSEs with improved stability against lithium metal and compatibility with high-voltage cathodes. For instance, LiPON exhibits a wide electrochemical stability window, making it particularly suitable for thin-film applications.

(c) Optimizing structures and compositions:

Advances in synthesis techniques, including high-energy ball milling and chemical vapor deposition, have enabled precise control over nitride compositions and crystal structures. These innovations have led to the development of materials such as lithium nitride halides and chalcogenides, which exhibit enhanced stability and ionic transport properties.

(d) Broadening material diversity:

Beyond α-Li_3N and LiPON, researchers have explored new classes of nitride SSEs, including lithium nitridophosphates and nitrides incorporating group 14 and group 13 elements. These materials offer tunable properties to balance ionic conductivity, chemical stability, and mechanical robustness.

With the goal of advancing nitride-based SSEs for all-solid-state lithium metal batteries, research has focused on developing new SSEs to improve ionic conductivity, expand electrochemical stability windows, and enhance compatibility with lithium metal. This involves detailed characterizations of crystal and local structures, chemical environments, and the fundamental mechanisms underlying lithium-ion conduction and chemical and electrochemical stability. Guided by these insights, researchers have designed and developed nitride SSEs with optimized compositions and structures to achieve enhanced cycling stability and high-rate performance in all-solid-state lithium metal batteries.

Key nitride SSEs include Li_3N, LiPON and their derivatives, lithium nitride halides, lithium nitride chalcogenides, and lithium nitridophosphates, as well as nitrides containing group 14 and group 13 elements. For each class of nitride SSEs, this review summarizes their compositions, crystal and local structures, and lithium-ion diffusion behaviors. Additionally, a detailed and in-depth discussion of compound- and structure-driven lithium-ion migration mechanisms is provided. This summary establishes essential guidelines for the innovation

Tsun-Kong Sham

Tsun-Kong Sham: He is a Distinguished University Professor and a Canada Research Chair in Materials and Synchrotron Radiation at the University of Western Ontario. He obtained his PhD from the University of Western Ontario (1975) with a BSc from the Chinese University of Hong Kong. He joined the Chemistry Department at Brookhaven National Laboratory in 1977 and returned to Western in 1988. His recent focus is nanostructure phase transition, assembly of nanocomposites, in situ/operando studies of energy materials and devices, X-ray excited optical luminescence, nanomaterials for drug delivery, and micro-beam analysis of cultural and heritage materials.

Xueliang Sun

Xueliang Sun: He is a Chair Professor at Eastern Institute of Technology, Ningbo, and a Foreign Member of the Chinese Academy of Engineering. He is a Fellow of both the Canadian Academy of Engineering and the Royal Society of Canada, as well as the founding Editor-in-Chief of Electrochemical Energy Reviews. His research focuses on advanced materials for electrochemical energy storage and conversion, including all-solid-state batteries, lithium-ion batteries, and fuel cells.

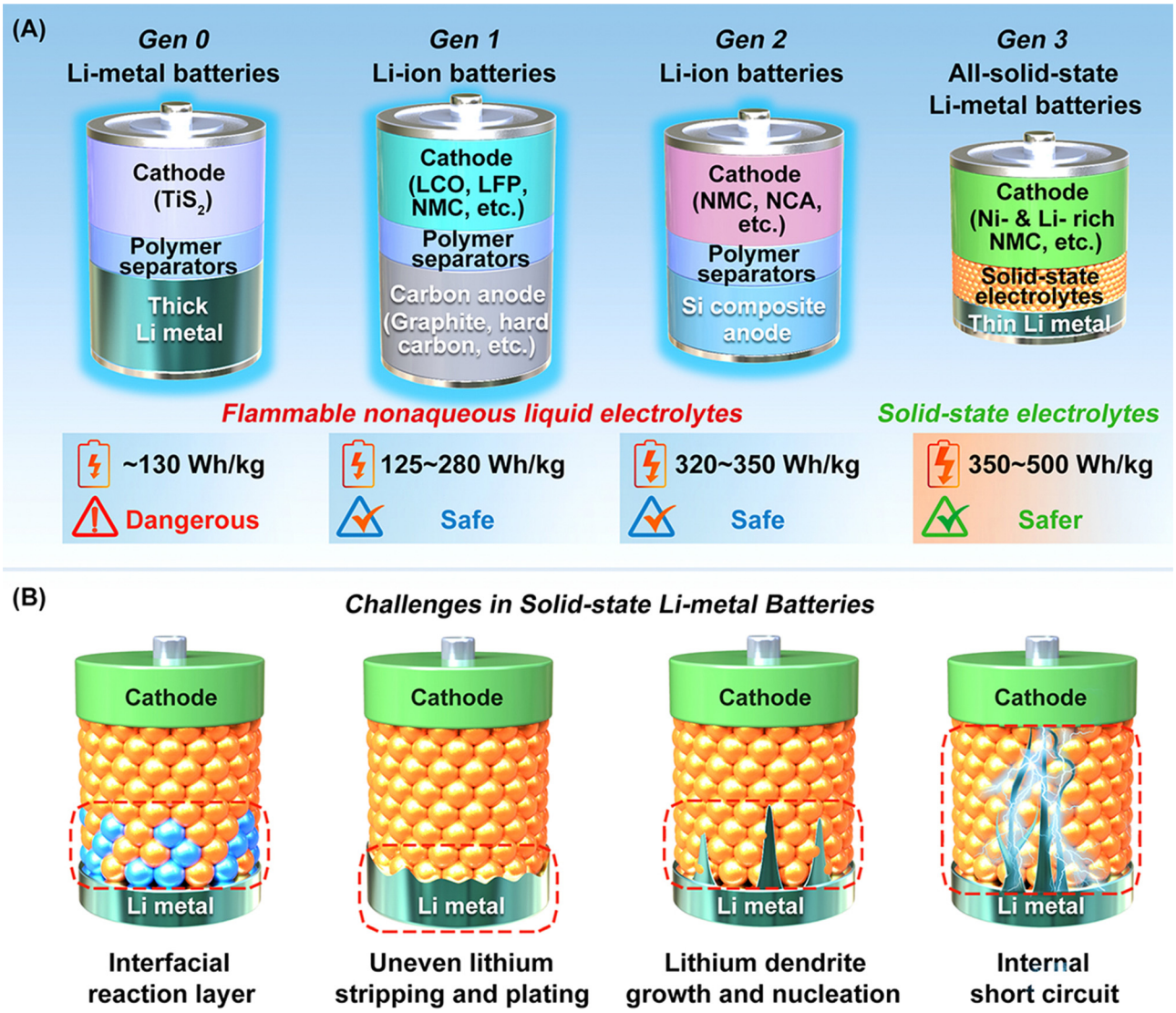

Fig. 1 (A) Research history of rechargeable lithium–metal and lithium-ion batteries and prediction of all-solid-state lithium–metal batteries. (B) Schematic illustrations of lithium metal–SSEs interfacial issues, interfacial reactions, uneven lithium stripping and plating, and lithium dendrite growth and nucleation.

of nitride SSEs, with a focus on optimizing compositions and structures to improve ionic conductivity, chemical and electrochemical stability, and ultimately, the overall performance of all-solid-state lithium metal batteries.

2.1 Li_3N solid-state electrolytes

The research on Li_3N as lithium ionic conductors began with the alpha phase. The crystal structure of α-Li_3N (hexagonal, *P*6/*mmm*) was first proposed by Zintl and Grauer in 1935,[19] and later confirmed by Rabenau and Schulz in 1976.[21] α-Li_3N crystals consist of hexagonal Li_2N layers connected by lithium ions (see Fig. 3). Lithium ions within and between the Li_2N layers can diffuse along open channels formed by nitrogen ions, making α-Li_3N a potential lithium ionic conductor. Masdupuy *et al.* first reported the lithium-ion conductivity of a loose powder of α-Li_3N with a high activation energy of 0.53 eV in 1957.[22,23] Subsequently, Boukamp and Huggins reported the ionic conductivity of sintered α-Li_3N pellets, achieving 10^{-7} to 10^{-8} S cm^{-1} at 25 °C with an activation energy of 0.61 to 0.63 eV in 1976.[22]

In 1977, α-Li_3N single crystals were prepared using the Czochralski method by Schönherr and Müller,[29] allowing Alpen *et al.* to measure anisotropic ionic migration properties perpendicular and parallel to the *c*-axis due to the hexagonal Li_2N layers in α-Li_3N.[26] Through a direct current (DC) polarization method, Alpen *et al.* confirmed α-Li_3N as a pure lithium ionic conductor with high ionic conductivity of 1.2×10^{-3} S cm^{-1} at 25 °C and a low activation energy of 0.29 eV perpendicular to the *c*-axis, but with much lower ionic conductivity of 1×10^{-5} S cm^{-1} and higher activation energy of 0.49 eV parallel to the *c*-axis (see Fig. 3E and Table 1).

The origin of this anisotropic ionic conduction characteristic of α-Li_3N is due to variations in energy barriers for lithium-ion diffusion within and between the hexagonal Li_2N layers.[28]

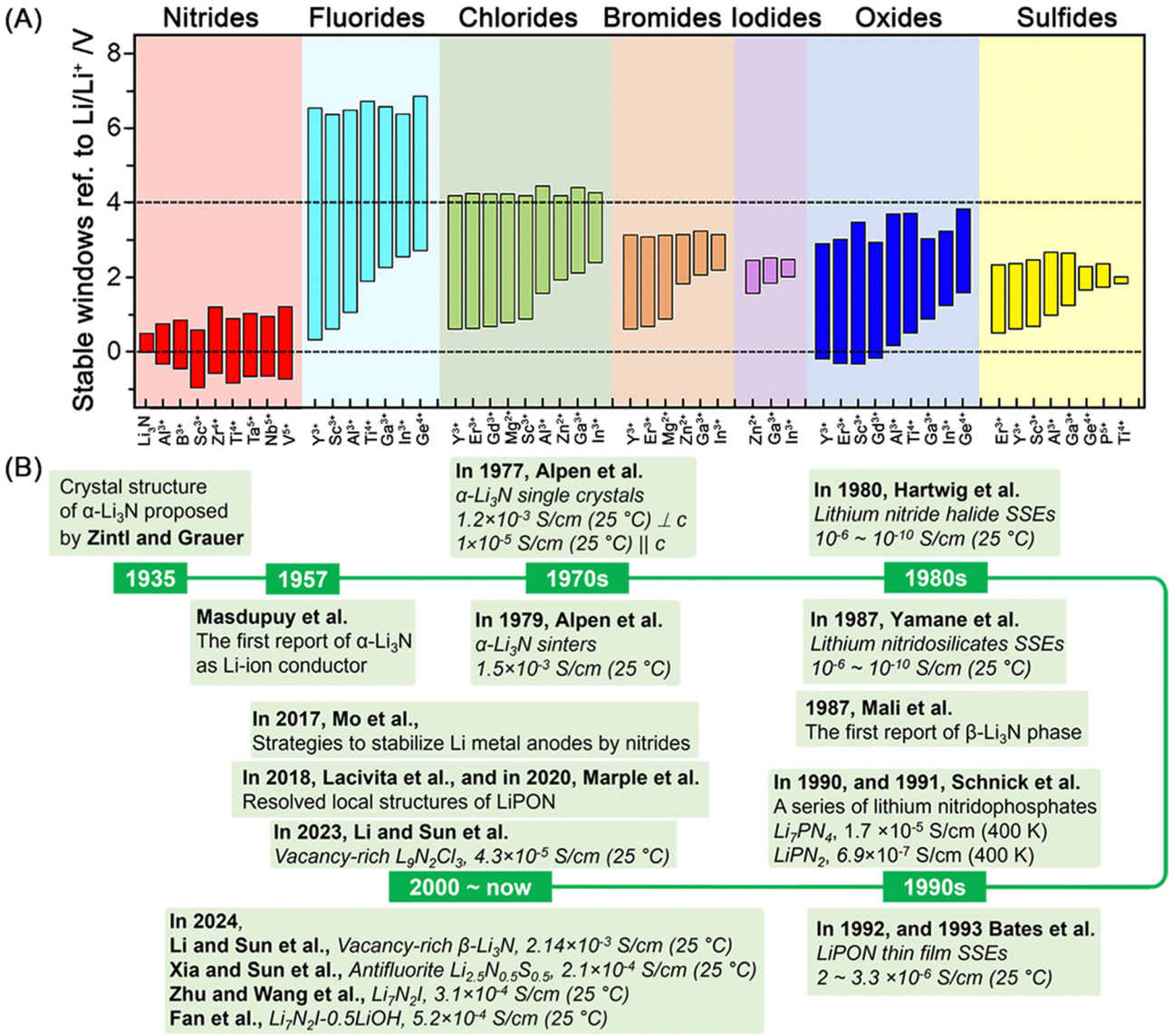

Fig. 2 2 (A) Calculated thermodynamic intrinsic electrochemical windows of Li_3N, Li–M–X ternary nitrides, fluorides, chlorides, bromides, iodides, oxides, and sulfides (M: a metal cation at its highest common valence state), reproduced with permission,[14] Copyright © 2022, American Chemical Society. (B) The brief research history of nitride SSEs.

According to simulation results, the fast lithium-ion diffusion mechanism in α-Li_3N relates to Li-vacancy-driven ion hopping. α-Li_3N crystals have natural vacancies at the Li(2c) sites within the hexagonal Li_2N layers.[37,38] The calculated activation energy for lithium-ion diffusion within hexagonal Li_2N layers (0.007 eV) is significantly lower than that between the layers (0.73 eV and 1.301 eV). With α-Li_3N single crystals showing superionic conduction, Alpen used a hot-pressing method (temperature: 500 to 700 °C, pressure: 0.5 to 3 kbar) to prepare α-Li_3N polycrystal sinters, which presented a high ionic conductivity of $\sim 1.5 \times 10^{-3}$ S cm^{-1} with an activation energy of 0.29 eV and a low electronic conductivity of $<10^{-10}$ S cm^{-1} (see Fig. 3E and Table 1).[27,38] Considering this anisotropic ionic conduction characteristic, Tapia-Ruiz *et al.*[39] reported two types of α-Li_3N nanofibers with hexagonal Li_2N stacked either parallel or perpendicular to the long axis of the nanofibers. Lower activation energies (0.075 and 0.053 eV) were observed for these two types of nanofibers compared to bulk α-Li_3N using ^{7}Li solid-state nuclear magnetic resonance (NMR). The sinters of α-Li_3N nanofibers showed a high ionic conductivity of $\sim 1 \times 10^{-3}$ S cm^{-1}, although it might be lower than the ionic conductivity of single α-Li_3N nanofibers due to grain boundaries in the sinters.

In addition to α-Li_3N, another superionic conducting beta phase, β-Li_3N (hexagonal, $P6_3/mmc$, see Fig. 3B), was discovered by high-pressure chemists and later developed by solid-state electrolyte chemists. Initial reports of α-Li_3N included new X-ray diffraction (XRD) lines found in ground Li_3N powder,[19,21] later confirmed to correspond to β-Li_3N later.[40] In 1987, Mali *et al.*[41] initially observed a phase transformation from α-Li_3N to a new phase under pressure *via* ^{7}Li-NMR, which was later

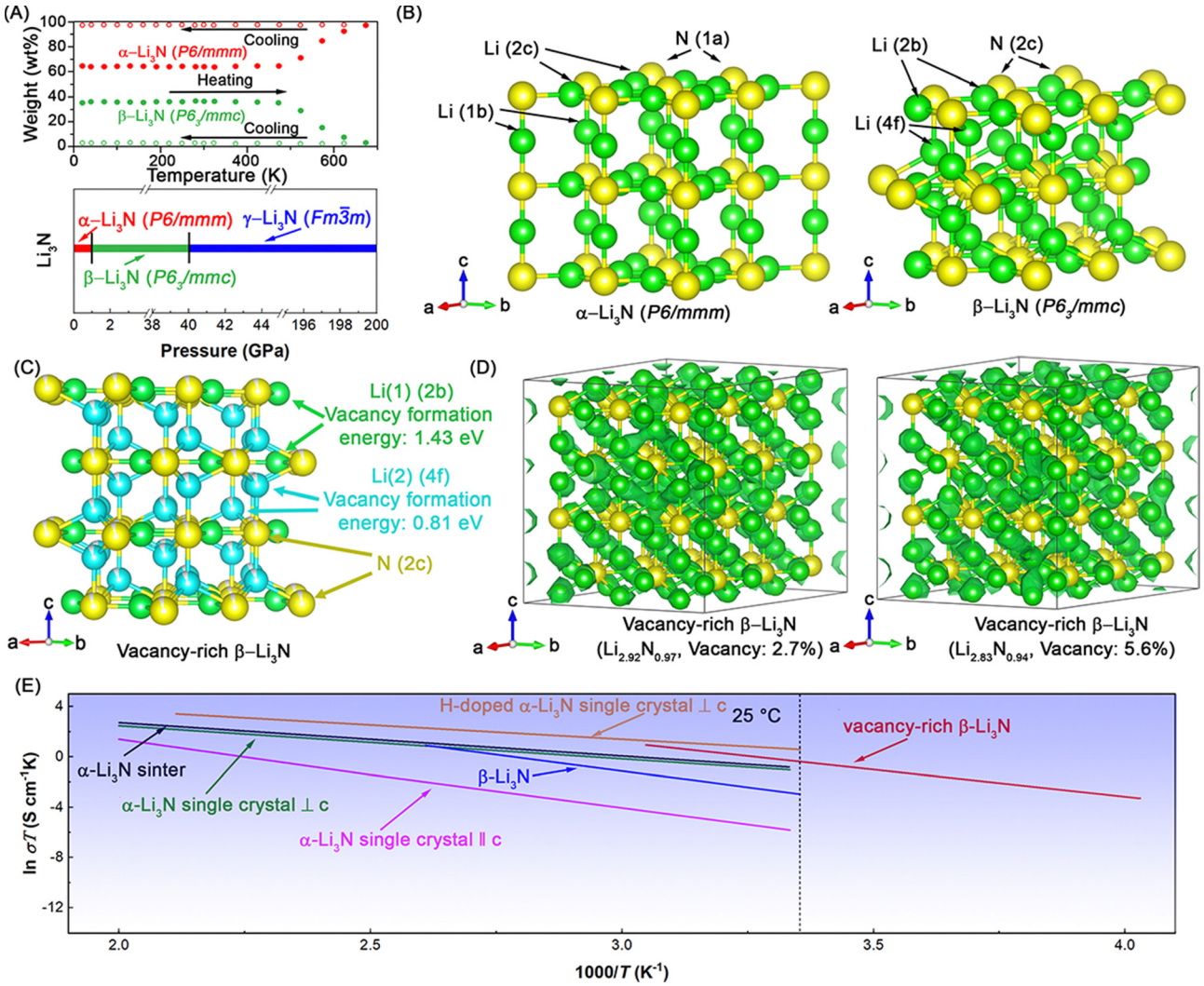

Fig. 3 3 (A) Phase change of Li_3N as a function of temperature and pressure. Reproduced with permission,[24] Copyright © 2006, Elsevier. (B) Crystal structures of two main phases of Li_3N, α-Li_3N and β-Li_3N. (C) Crystal structures of vacancy-rich β-Li_3N and calculated formation energy of single neutral lithium vacancy at 2c and 4f sites in β-Li_3N, respectively. Reproduced with permission,[15] (D) lattice structures and superimposed lithium-ion probability density (marked by green iso-surfaces) in vacancy-rich β-Li_3N with different lithium vacancy concentrations 2.7%, in $Li_{2.92}N_{0.97}$ and 5.6% in $Li_{2.83}N_{0.94}$ based on AIMD simulations at 600 K. (E) Arrhenius plots of several developed Li_3N SSEs, including vacancy-rich β-Li_3N,[15] H-doped α-Li_3N single crystals,[25] α-Li_3N single crystals,[26] α-Li_3N sinter,[27] and β-Li_3N,[28] for comparison.

confirmed to be β-Li_3N through Raman spectra and X-ray diffraction by Beister *et al.* in 1988.[40] Beister found that this transformation from α-Li_3N to β-Li_3N started at around 0.6 GPa, with β-Li_3N maintaining its phase up to ~8 GPa under pressure and remaining stable for months after the pressure release. Recent research confirmed that β-Li_3N remains stable up to 40 GPa, beyond which it transforms to γ-phase (cubic, $Fm\bar{3}m$) at 40 to 200 GPa (see Fig. 3A).[42] β-Li_3N can also revert to α-Li_3N at high temperatures. Huq *et al.*[24] phase transformation from β-Li_3N to α-Li_3N during heating *via* neutron diffraction (see Fig. 3A). This transformation begins at ~200 °C and completes at ~400 °C, with α-Li_3N remaining stable upon cooling to room temperature.

Similar to the hexagonal Li_2N layers in the crystal structure of α-Li_3N, β-Li_3N consists of hexagonal LiN layers stacked in an ABAB sequence along the *c*-axis. The nitrogen atom arrangement in β-Li_3N belongs to close hexagonal packing, while in α-Li_3N it is simple hexagonal packing. Recently, Li and Sun *et al.*[15] reported a vacancy-rich β-Li_3N with high room temperature (25 °C) ionic conductivity of 2.14×10^{-3} S cm^{-1} due to vacancies at Li(4f) sites between hexagonal LiN layers and N(2c) sites. The lithium vacancies are concentrated at Li(4f) sites due to lower vacancy formation energy compared to Li(2b) sites (see Fig. 3C). With high vacancy concentrations at Li(4f) (~8.1(2)%) and N(2c) (~5.4(1)%) sites, this vacancy-rich β-Li_3N displayed a high room-temperature ionic conductivity of 2.14×10^{-3} S cm^{-1}, surpassing nearly all reported pure Li_3N SSEs (see Fig. 3E and Table 1).

Fig. 3D presents the lithium-ion probability density (marked by green iso-surfaces) in this vacancy-rich β-Li_3N with different lithium vacancy concentrations of 2.7% in $Li_{2.92}N_{0.97}$ and 5.6% in $Li_{2.83}N_{0.94}$ based on *ab initio* molecular dynamics (AIMD)

Table 1 Lithium nitride solid-state electrolytes and lithium phosphorus oxynitride (LiPON) and derivative solid-state electrolytes

Lithium nitride solid-state electrolytes			
Materials	Structures	Room-temperature ionic conductivity	Activation energy
α-Li_3N single crystal[26]	Hexagonal (*P*6/*mmm*)	1.2×10^{-3} S cm^{-1} (300 K)$\perp c$ 1.0×10^{-5} S cm^{-1} (300 K)$\parallel c$	0.290 eV$\perp c$ 0.490 eV$\parallel c$
α-Li_3N sinter[27]	Hexagonal (*P*6/*mmm*)	1.5×10^{-3} S cm^{-1} (300 K)	0.290 eV
H-doped α-Li_3N single crystal[25]	N/A[a]	6.0×10^{-3} S cm^{-1} (25 °C)$\perp c$	0.198 eV$\perp c$
β-Li_3N[28]	Hexagonal ($P6_3/mmc$)	2.085×10^{-4} S cm^{-1} (25 °C)	0.448 eV
Vacancy-rich β-Li_3N[15]	Hexagonal ($P6_3/mmc$)	2.14×10^{-3} S cm^{-1} (25 °C)	0.371 eV
Lithium phosphorus oxynitride (LiPON) and derivative solid-state electrolytes			
Materials	Structures	Room-temperature ionic conductivity	Activation energy
$Li_{3.3}PO_{3.9}N_{0.17}$[30]	Amorphous	2.2×10^{-6} S cm^{-1} (25 °C)	0.56 eV
$Li_{2.9}PO_{3.3}N_{0.46}$[31]	Amorphous	3.3×10^{-6} S cm^{-1} (25 °C)	0.54 eV
$Li_{1.35}Si_{0.79}P_{0.21}O_{1.96}N_{0.96}$[32]	Amorphous	2.06×10^{-5} S cm^{-1} (25 °C)	0.45 eV
$Li_{2.9}Si_{0.35}PO_{1.5}N_{1.26}$[33]	Amorphous	1.24×10^{-5} S cm^{-1} (25 °C)	0.479 eV
LiBPON[34]	Amorphous	3.5×10^{-6} S cm^{-1} (25 °C)	0.53 eV
LiPSON[35]	Amorphous	1.58×10^{-5} S cm^{-1} (25 °C)	0.49 eV
LiLaAlPON[36]	Amorphous	1.47×10^{-5} S cm^{-1} (25 °C)	0.54 eV

[a] Up to now, these compounds' crystal structures have not been resolved.

simulations at 600 K. Lithium and nitrogen vacancies induce fast lithium-ion migration observed in three-dimensional channels, and higher vacancy concentration in this vacancy-rich β-Li_3N leads to lower activation energy and higher room-temperature ionic conductivity. The optimized vacancy-rich β-Li_3N presented a high room-temperature ionic conductivity of 2.14×10^{-3} S cm^{-1}, surpassing all reported pure Li_3N SSEs (see Fig. 3E and Table 1). The vacancy-rich β-Li_3N-based all-solid-state lithium metal batteries, including pouch cells, exhibited excellent electrochemical performance with long cycling life and high areal capacities. The discussion on all-solid-state lithium metal batteries will be continued in the following sections.

2.2 Lithium phosphorus oxynitride (LiPON) and derivative solid-state electrolytes

Amorphous LiPON was first reported by Bates *et al.* at Oak Ridge National Laboratory in 1992. It was discovered as a thin-film SSE with nitrogen incorporated into amorphous Li_3PO_4 thin films *via* radio frequency magnetron sputtering.[30] After incorporating 6 atom percentage (at%) of nitrogen into the sputtered Li_3PO_4 thin film, the room-temperature ionic conductivity of LiPON increased by more than 45 times, from 7×10^{-8} S cm^{-1} (Li_3PO_4) to 3.3×10^{-6} ($Li_{2.9}PO_{3.3}N_{0.46}$).[31] This accelerated lithium ion diffusion in LiPON originates from the arrangement of local structures due to the incorporation of nitrogen into LiO_4 and PO_4 tetrahedra. Recent studies have identified three possible nitrogen configurations in the phosphate structures of amorphous LiPON: apical nitrogen (N_a), double bridging nitrogen (N_d), and triple bridging nitrogen (N_t) (see Fig. 4A).[43] However, the exact identification of these amorphous structures remains inconclusive.

Initially, the interpretation of X-ray photoelectron spectroscopy (XPS) by Bates *et al.* suggested two N-related modes of N_d and N_t with two and three $P(ON)_4$ tetrahedra bonded by N atoms, respectively.[30] However, recent simulation and experimental results by Lacivita *et al.*[43,44] and Marple *et al.*[45] suggested the absence of N_t and the presence of N_a and N_d. In 2018, Lacivita *et al.* used *ab initio* molecular dynamics (AIMD) and density functional theory (DFT) simulations and neutron scattering, XPS, and infrared spectroscopy (IR) to resolve the amorphous structures of sputtered LiPON ($Li_{2.94}PO_{3.5}N_{0.31}$) as shown in Fig. 4B. It only has two structure configurations regarding N atoms, N_a (isolated $P(O,N)_4$ tetrahedra), and N_d (two phosphate tetrahedra linked by N atoms). Afterwards, Marple *et al.* also confirmed the lack of N_t in LiPON and further determined local structures in short range order through one-dimensional (1D) and two-dimensional (2D) solid-state NMR, and AIMD simulations. To identify the bridging types, a modified nomenclature, Q_m^n was introduced, where n is the number of bridging atoms and ranges from 3 to 0, and m is the number of N atoms on the $P(ON)_4$ tetrahedra and ranges from 4 to 0. As shown in Fig. 4D, ^{31}P magic angle spinning (MAS) NMR results confirmed the presence of Q_0^0 (*i.e.*, isolated PO_4 tetrahedra), Q_0^1 (*i.e.*, dimeric PO_4 tetrahedra), Q_1^0 (*i.e.*, N_a), and Q_1^1 (*i.e.*, N_d). And the absence of Q_m^2 environment indicated no presence of N_t in sputtered LiPON as shown in Fig. 4C. But the results from Lacivita *et al.* and Marple *et al.* cannot rule out the presence or absence of N_t in other LiPON thin films as reported LiPON thin films vary from compositions and preparation methods.[53]

As reported in other works,[31,46–52] the presence and absence of N_a, N_d, and N_t vary from LiPON compositions (see Fig. 4E). And the compositions determine the lithium-ion diffusion behaviors. When the lithium content in LiPON is low with the Li : P ratio ranges from 1 : 1 to 2.91 : 1, the mainly determining factor for the lithium-ion diffusion is lithium amount and higher lithium content results in higher ionic conductivity. Additionally, the incorporation of N also accounts for the accelerated lithium-ion migration. Among these three N-based configurations, the formation of N_d has a positive effect on ionic conductivity. The bridging N atoms bring two phosphate groups together and closer, which helps open diffusion channels for lithium-ion migration. Moreover, the less electronegative

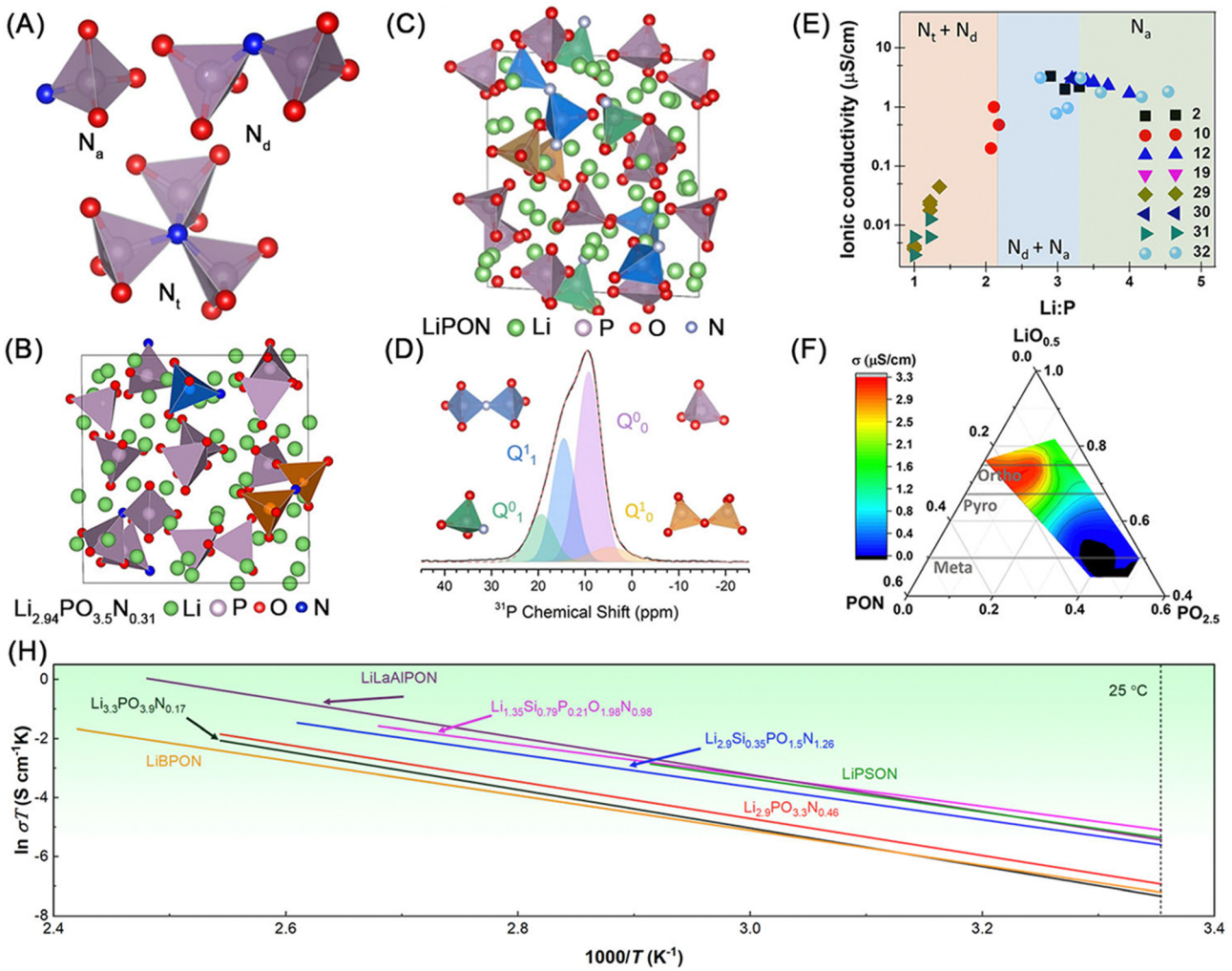

Fig. 4 (A) Schematic illustration of three possible N configurations in LiPON, reproduced with permission,[43] Copyright © 2018 American Chemical Society. (B) Local structures of $Li_{2.94}PO_{3.50}N_{0.31}$ according to AIMD simulations. Reproduced with permission,[44] Copyright © 2018 American Chemical Society. (C) Local structures of sputtered LiPON according to AIMD simulations and (D) ^{31}P MAS NMR spectra of this LiPON spinning at 25 kHz. Polyhedrons: purple Q^0_0, blue Q^1_1, green Q^0_1, and orange Q^1_0 spinning at 25 kHz. Reproduced with permission,[45] Copyright © 2020 Wiley-VCH GmbH. Room temperature ionic conductivity of LiPON as a function of (E) lithium content and (F) compositions. The ionic conductivity data used in (E) was collected from ref. 31 (black squares), ref. 46 (red solid circles), ref. 47 (blue triangles), ref. 48 (magenta triangles), ref. 49 (dark yellow square), ref. 50 (navy triangles), ref. 51 (dark cyan triangles), and ref. 52 (cyan balls). Reproduced with permission,[44] Copyright © 2018 American Chemical Society. (F) Arrhenius plots of LiPON and doped-LiPON-derivatives including $Li_{3.3}PO_{3.9}N_{0.17}$,[30] $Li_{2.9}PO_{3.3}N_{0.46}$,[31] $Li_{1.35}Si_{0.79}P_{0.21}O_{1.96}N_{0.96}$,[32] $Li_{2.9}Si_{0.35}PO_{1.5}N_{1.26}$,[33] LiBPON,[34] LiPSON,[35] and LiLaAlPON[36] for comparison.

character of N than O and strong covalent bonds between N with P reduces interaction between phosphate groups and lithium ions, which lowers down lithium-ion migration barriers. On the sharp contrary, the increase of N_a percentage induces decrease of ionic conductivity. In addition to compositions, amorphous character of LiPON is another importance factor for improved ionic conductivity and smooths the migration pathways of mobile lithium ions.

Owing to an acceptable room-temperature ionic conductivity ($2.0–3.3 \times 10^{-6}$ S cm^{-1}), wide stable electrochemical window (experimental results: 0–5.5 V *vs.* Li/Li$^+$) and high stability towards lithium metal,[54] LiPON shows great potential as SSE layers for thin-film all-solid-state lithium metal batteries.[17,55] In addition to LiPON prepared *via* incorporation of N into Li_3PO_4 structures, a lots of LiPON-derivative SSEs have also been synthesized to further increase ionic conductivity, including Si-doped,[32,33] B-doped,[34] S-doped[35] and metallic element-doped[36] LiPON-derivatives (see Fig. 4H and Table 1). The room-temperature ionic conductivity of LiPON-derivatives reaches higher than 3.3×10^{-6} S cm^{-1} and up to 2.06×10^{-5} S cm^{-1}.

2.3 Lithium nitride halide solid-state electrolytes

The studies of lithium nitride halides dated back to 1960s–1980s. Sattlegger,[56,57] Hartwig,[58–60] Obayashi,[61] and their coworkers conducted the pioneering works and discovered a series of lithium nitride halide SSEs, including $Li_9N_2Cl_3$, $Li_{11}N_3Cl_2$, Li_6NBr_3, $Li_{13}N_4Br$, Li_5NI_2, Li_7N_2I, *etc.* As some lithium nitride halides initially synthesized by Sattlegger, Hartwig and their

co-workers, Hartwig *et al.*[60] firstly reported the phase diagrams of these three binary systems of Li_3N–LiCl, Li_3N–LiBr and Li_3N–LiI (see Fig. 5A–C). In the case of lithium nitride chlorides, $Li_{11}N_3Cl_2$ (crystal structure not determined) and $Li_{1.8}N_{0.4}Cl_{0.6}$ ($Li_9N_2Cl_3$, space group: $Fm\bar{3}m$) are two stable ternary compounds. Among them, $Li_9N_2Cl_3$ presents higher room temperature ionic conductivity of $\sim 1 \times 10^{-6}$ S cm^{-1} and much lower activation energy of 0.495 eV than $Li_{11}N_3Cl_2$ (activation energy: 0.83 eV calculated room-temperature ionic conductivity: $\sim 3.7 \times 10^{-11}$ S cm^{-1}) as shown in Fig. 5E and Table 2.[59] The fast lithium-ion diffusion in $Li_9N_2Cl_3$ results from an antifluorite structure with vacant lithium sites. Hartwig *et al.*[58,59] reported a high lithium site vacancy concentration of 10% while the anionic partial lattice is fully occupied by N and Cl (atom site percentage: 60% and 40% for N and Cl, respectively). Therefore, the chemical formula $Li_{1.8}N_{0.4}Cl_{0.6}$ can describe this lithium nitride chloride. However, the crystal structures with chemical stoichiometry of this lithium halide chloride with the $Fm\bar{3}m$ space group remains inconclusive. In 1997, Marx *et al.*[62] reported the chemical stoichiometry with this $Fm\bar{3}m$ space group of Li_5NCl_2, which has randomly distributed N and Cl atoms (atom ratio: 1 : 2) at the anionic sites and Li atoms occupying the $(N,Cl)_4$ tetrahedral interstitial sites with a 1/6 vacancy concentration. Recently, Li *et al.*[16] synthesize a vacancy-rich $Li_9N_2Cl_3$. According to refining the regulation of average crystal structures and local disorder structures by synchrotron-based X-ray diffraction (SXRD) & pair distribution function analysis (PDF), and time-of-flight (TOF) neutron diffraction, the chemical stoichiometry was further confirmed to be $Li_9N_2Cl_3$ but with higher Li vacancy population and vacant anionic sites (composition: $Li_{8.60(5)}N_{1.911(5)}Cl_{2.867(5)}$) as shown in Fig. 5D. Additionally, the N and Cl atoms should not be totally randomly distributed at the $(N,Cl)_4$ tetrahedral vertices according to the PDF fitting results, while the detailed distribution of N and Cl atoms requires further studies, such as reverse Monte Carlo (RMC) modeling of the PDF data. Owing to the

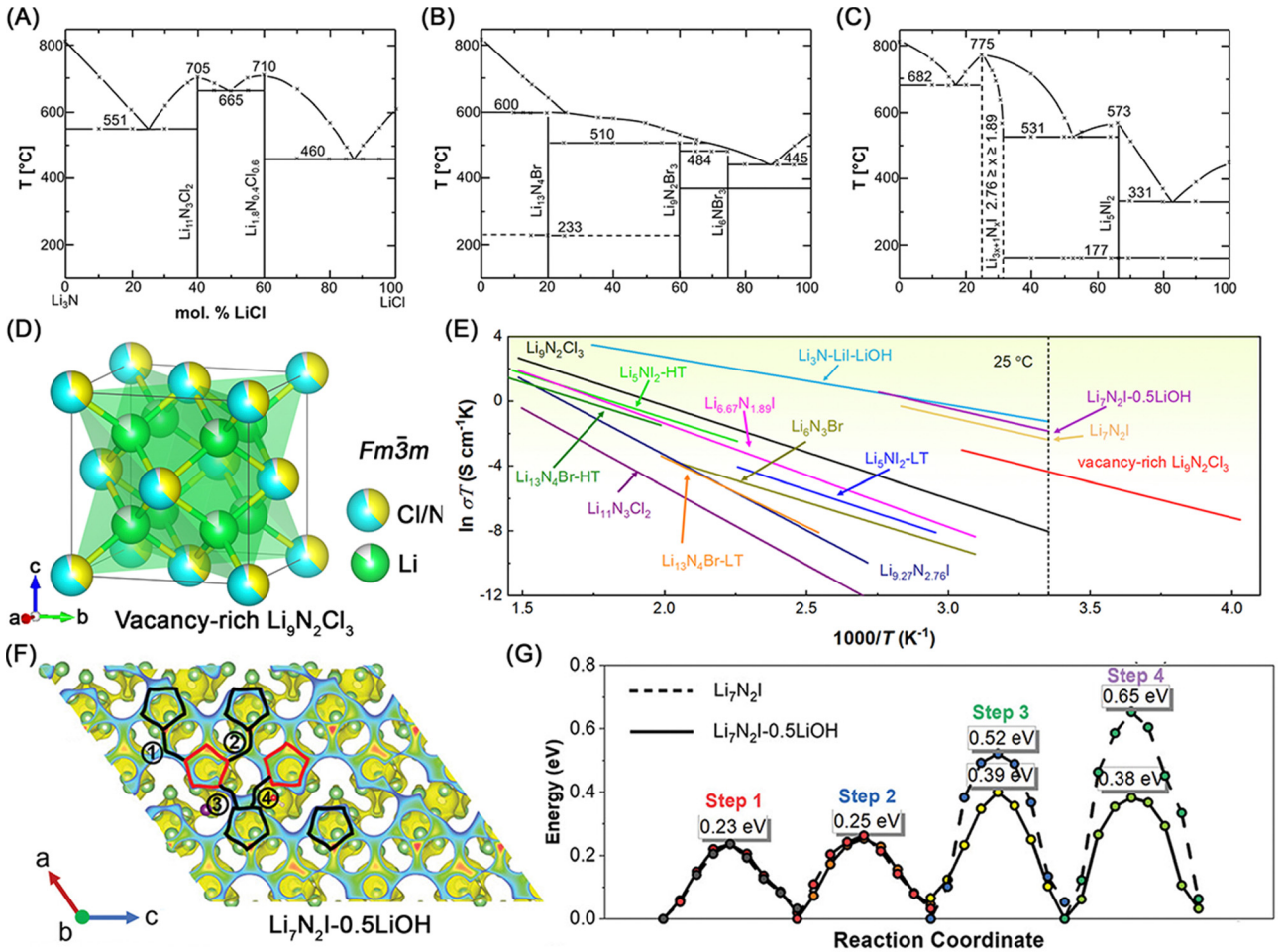

Fig. 5 Phase diagram of the quasi-binary (A) Li_3N–LiCl system, (B) Li_3N–LiBr system, and (C) Li_3N–LiI system. Reproduced with permission,[60] © 1981 Published by Elsevier B.V. (D) Crystal structures of vacancy-rich $Li_9N_2Cl_3$. (E) Arrhenius plots of vacancy-rich $Li_9N_2Cl_3$,[16] $Li_9N_2Cl_3$,[58] $Li_{11}N_3Cl_2$,[59] Li_6NBr_3,[64] $Li_{13}N_4Br$-HT,[64] $Li_{13}N_4Br$-LT,[64] Li_5NI_2-HT,[59] Li_5NI_2-LT,[59] $Li_{6.67}N_{1.89}I$,[59] $Li_{9.27}N_{2.76}I$,[59] Li_3N–LiI–LiOH,[65] Li_7N_2I,[66] and Li_7N_2I–0.5LiOH[67] for comparison. (F) Reference lithium-ion migration steps characterized by isosurfaces for Li_7N_2I and Li_7N_2I–0.5LiOH lattice along the *a*–*c* plane (green spheres represent Li; purple spheres represent I; red spheres represent O; pink spheres represent H). (G) Energy barriers of various lithium-ion migration steps in the Li_7N_2I and Li_7N_2I–0.5LiOH lattice along with *a*–*c* plane. Reproduced with permission,[67] © 2024 Wiley-VCH GmbH.

higher Li-, N-, and Cl-vacancy population, this vacancy-rich $Li_9N_2Cl_3$ increases the room-temperature ionic conductivity by a factor of more than 40 to 4.3×10^{-5} S cm^{-1} from $\sim 1 \times 10^{-6}$ S cm^{-1} and reduces the activation energy to 0.378 eV from 0.495 eV comparing to Hartwig *et al.*'s results (see Fig. 5E and Table 2). In addition to $Li_9N_2Cl_3$, another two phases have been reported and shares the same space group of $R\bar{3}m$, Li_5NCl_2 and Li_4NCl, while their lithium-ion conductivity has not been reported.[62,63]

Fig. 5B shows the phase diagram of the Li_3N–LiBr system reported by Hartwig *et al.*,[60] which includes three stable ternary lithium nitride bromides, $Li_{13}N_4Br$ (a hexagonal structure), $Li_9N_2Br_3$ (a body-centered tetragonal structure), and Li_6NBr_3 (a face-centered cubic crystal structure). Among them, both of Li_6NBr_3 and $Li_{13}N_4Br$ present low room-temperature ionic conductivity (see Fig. 5E and Table 2).[64] The activation energy of Li_6NBr_3 is 0.46 eV and the calculated room-temperature ionic conductivity is 6.59×10^{-8} S cm^{-1}. $Li_{13}N_4Br$ undergoes a phase transition at around 230 °C and there are two phases, $Li_{13}N_4Br$-high temperature ($Li_{13}N_4Br$-HT), and $Li_{13}N_4Br$-low temperature ($Li_{13}N_4Br$-LT). $Li_{13}N_4Br$-LT presents a high activation energy of 0.73 eV and the calculated room-temperature ionic conductivity is only 1.06×10^{-9} S cm^{-1}, while the activation energy decrease to 0.47 eV after this phase transition to $Li_{13}N_4Br$-HT. Later, Marx[68] refined the lithium nitride bromide with the hexagonal structure to a hexagonal space group $P\bar{6}m2$ with a chemical stoichiometry of $Li_{10}N_3Br$. Additionally, Marx *et al.*[69] reported another lithium nitride bromide compound, Li_5NBr_2 (a orthorhombic space group *Immm*), however without conducting lithium-ion diffusion studies.

Hartwig *et al.*[60] also reported the phase diagram of the Li_3N–LiI system (see Fig. 5C) and one stable phase, Li_5NI_2. This Li_5NI_2 was initially reported by Sattlegger *et al.*[57] in 1964 with a space group of $F\bar{4}3m$. And the Li_3N-rich compounds with the compositions of $Li_{3x+1}N_xI$ ($2.76 \geq x \geq 1.89$) was further confirmed to be another stable phase of Li_7N_2I (space group: $Fd3m$).[57,70] Among both phases, Li_5NI_2 showed a phase transition at around 170 °C. The high-temperature phase (Li_5NI_2-HT) delivered a low activation energy of 0.44 eV, while the corresponding low-temperature phase (Li_5NI_2-LT) increased the activation energy to 0.5 eV (see Fig. 5E and Table 2).[59] According to Hartwig *et al.*'s results,[59] a Li_3N-rich lithium nitride iodide, $Li_{6.67}N_{1.89}I$ showed a lower activation energy than another Li_3N-rich phase, $Li_{9.27}N_{2.76}I$. The difference in activation energy should originate from possible low-ionic conducting impurity phases in these two compounds as more amorphous impurity phases in the composition of $Li_{9.27}N_{2.76}I$ if Li_7N_2I is considered as the stable crystalline phase for both compositions. In addition to these two binary Li_3N–LiI phases, Obayashi *et al.*[65] reported the effect of LiOH in Li_3N–LiI (molecular ratio: 1 : 2) on the lithium-ion diffusion behavior. After optimization of the compositions (1Li_3N–2LiI–0.77LiOH), the room-temperature ionic conductivity reaches to 9.5×10^{-4} S cm^{-1} and the activation energy is 0.255 eV (see Fig. 5E and Table 2), which demonstrated the highest room-temperature ionic conductivity and lowest activation energy in lithium nitride halide SSEs. To elucidate the mechanism behind the accelerated lithium-ion diffusion in this ternary Li_3N–LiI–LiOH system, Wang[66] and Fan[67] *et al.*, prepared Li_7N_2I and Li_7N_2I–0.5LiOH SSEs, displaying room-temperature ionic conductivity of 3.1×10^{-4} S cm^{-1} and 5.2×10^{-4} S cm^{-1}, respectively. They found that the incorporation of LiOH into the bulk phase of Li_7N_2I facilitated fast two-dimensional migrating channels by creating interstitial Li sites with reduced lithium hopping energy barriers (see Fig. 5F and G).

2.4 Lithium nitride chalcogenide and lithium nitridophosphate solid-state electrolytes

In the case of lithium nitride chalcogenides (Li–N–S and Li–N–Se compounds), several solid-state electrodes have been reported, including Li_9S_3N,[71] $Li_{2.5}N_{0.5}S_{0.5}$,[72] and Li_8SeN_2.[73]

For lithium nitride sulfides, one stable compound, Li_9S_3N has been reported.[71,74] Li_9S_3N was initially reported by Marx *et al.*[74] and displays an anti-fluorite crystal structure (cubic, $Pm\bar{3}m$) with an face-centered cubic anion sublattice. As this crystal structure shows almost defect-free lattices, it presents a

Table 2 Lithium nitride halide solid-state electrolytes

Lithium nitride halide solid-state electrolytes			
Materials	Structures	Room-temperature ionic conductivity	Activation energy
$Li_9N_2Cl_3$[58]	Cubic ($Fm\bar{3}m$)	2.3×10^{-6} S cm^{-1} (25 °C)	0.495 eV
$Li_{11}N_3Cl_2$[59]	N/A	$\sim 3.7^a \times 10^{-11}$ S cm^{-1} (25 °C)	0.83 eV
Vacancy-rich $Li_9N_2Cl_3$[16]	Cubic ($Fm\bar{3}m$)	4.3×10^{-5} S cm^{-1} (25 °C)	0.378 eV
Li_6NBr_3[64]	Cubic	$6.59^a \times 10^{-8}$ S cm^{-1} (25 °C)	0.46 eV
$Li_{13}N_4Br$[64 *b*]	Hexagonal ($P\bar{6}m2$)	$1.06^a \times 10^{-9}$ S cm^{-1} (25 °C)	0.73 eV (LT) 0.47 eV (HT)
Li_5NI_2[59]	Cubic ($F\bar{4}3m$)	$1.0^a \times 10^{-7}$ S cm^{-1} (25 °C)	0.50 eV (LT) 0.44 eV (HT)
$Li_{6.67}N_{1.89}I$[59]	N/A[c]	$1.5^a \times 10^{-7}$ S cm^{-1} (25 °C)	0.55 eV
$Li_{9.27}N_{2.76}I$[59]	N/A[c]	$4.3^a \times 10^{-10}$ S cm^{-1} (25 °C)	0.80 eV
Li_3N–LiI–LiOH[65]	N/A[c]	9.5×10^{-4} S cm^{-1} (25 °C)	0.255 eV
Li_7N_2I[66]	*Cm*	3.1×10^{-4} S cm^{-1} (25 °C)	0.34 eV
Li_7N_2I–0.5LiOH[67]	*Cm*	5.2×10^{-4} S cm^{-1} (25 °C)	0.35 eV

[a] The room-temperature ionic conductivity is calculated based on Arrhenius plots. [b] The chemical stoichiometry of the corresponding crystal structure was then refined to $Li_{10}N_3Br$ by Marx.[68] [c] Up to now, these compounds' crystal structures have not been resolved.

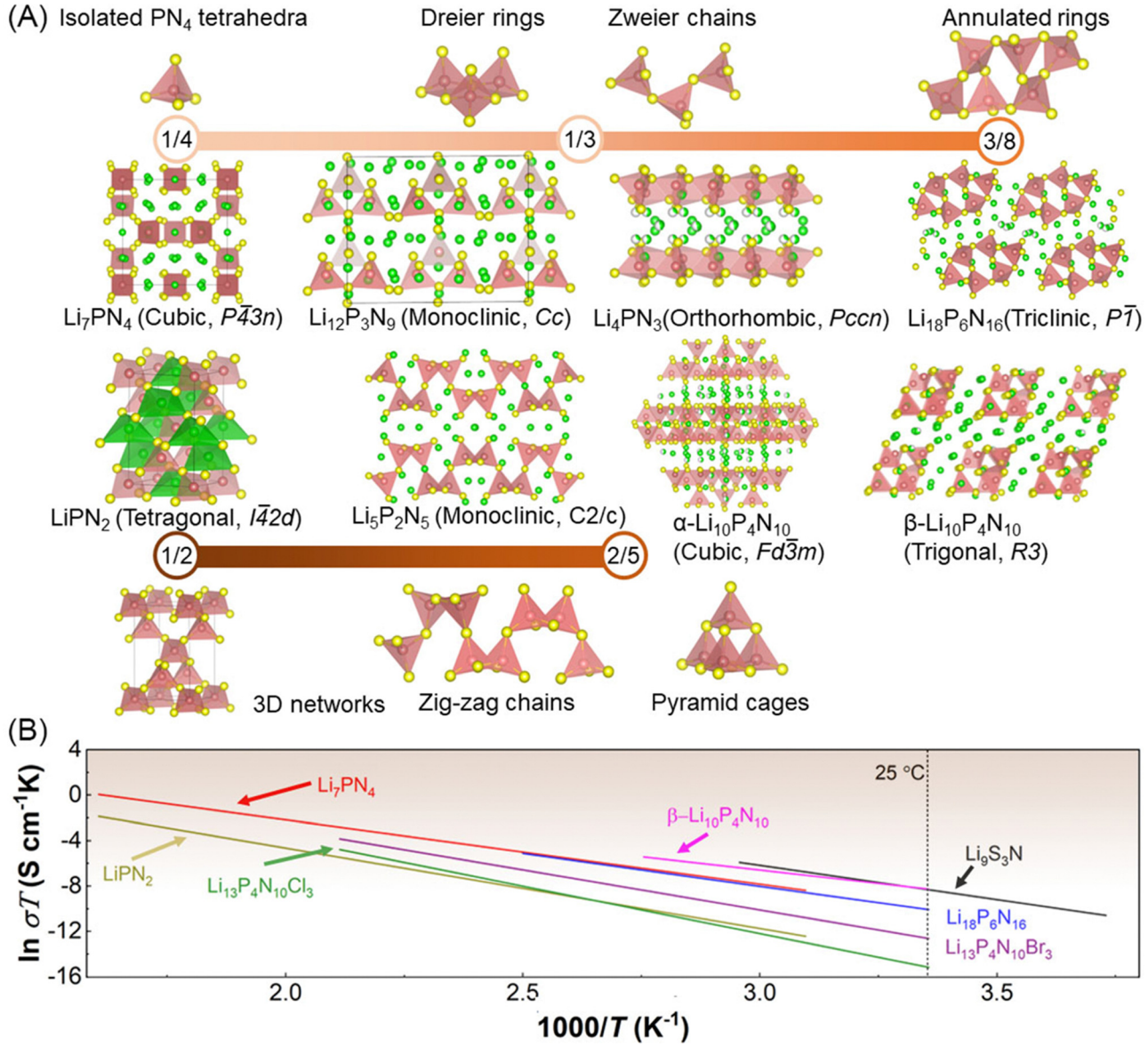

Fig. 6 (A) Crystal structures of a series of lithium nitridophosphates and their corresponding PN_4 tetrahedra networks and degrees of condensation κ (the atomic ratio of central P atoms to vertical N atoms of tetrahedra within one network), green: Li atoms, yellow: N atoms, red: P atoms. (B) Arrhenius plots of Li_9S_3N,[71] Li_7PN_4,[75] $Li_{18}P_6N_{16}$,[76] β-$Li_{10}P_4N_{10}$,[77] $LiPN_2$,[75] $Li_{13}P_4N_{10}Br_3$,[77] and $Li_{13}P_4N_{10}Cl_3$.[77]

high activation energy of 0.52 eV and a low room-temperature ionic conductivity of 8.3×10^{-7} S cm^{-1} (see Fig. 6B and Table 3).[71] Like lithium nitride sulfides, one stable lithium nitride selenide, Li_8SeN_2 has been reported by Bräunling *et al.*[73] and crystallizes in a space group of $I4_1md$ (tetragonal). ^{7}Li-NMR confirmed available lithium motion in Li_8SeN_2, while no room-temperature ionic conductivity has been reported. Recently, Xia and Sun *et al.* reported a new phase of lithium nitride sulfide, anti-fluorite $Li_{2.5}N_{0.5}S_{0.5}$ (space group: $Fm\bar{3}m$),[72] displaying a high room-temperature ionic conductivity of 2.1×10^{-4} S cm^{-1} and the fast lithium diffusion mechanism is due to introducing new interstitial lithium sites.

Schnick and co-workers[78,79] have conducted pioneering research works of lithium nitridophosphates (including $LiPN_2$,[75,80] $Li_{10}P_4N_{10}$,[77,81,82] $Li_{18}P_6N_{16}$,[76] $Li_{12}P_3N_9$,[83] and Li_7PN_4[75]) following initial reports of $LiPN_2$ in 1960 by Eckerlin *et al.*,[84,85] and Li_7PN_4 in 1971 by Brice *et al.*,[86] according to the lattice structures of PN_4 tetrahedra networks, the degree of condensation (*i.e.* the atomic ratio of central P atoms to vertical N atoms of tetrahedra within one network, denoted as κ) is used to describe these lithium nitridophosphates as shown in Fig. 6A. As the κ values increases from 1/4 to 1/2, PN_4 tetrahedra networks display a series of sub-lattice structures, including isolated PN_4 tetrahedra, Dreier rings and Zweier chains (κ = 1/3), annulated rings (κ = 3/8), zig-zag chains and pyramid cages (κ = 2/5), and three-dimensional (3D) networks (κ = 1/2). Based on these sub-lattices consisting of PN_4 tetrahedra, these lithium nitridophosphates display different crystal symmetries, including the triclinic lattice ($Li_{18}P_6N_{16}$ ($P\bar{1}$)), the monoclinic lattice

Table 3 Lithium nitride chalcogenide and lithium phosphorus nitride solid-state electrolytes

Lithium nitride chalcogenide and lithium phosphorus nitride solid-state electrolytes			
Materials	Structures	Room-temperature ionic conductivity	Activation energy
Li_9S_3N[71]	Cubic ($Pm\bar{3}m$)	8.3×10^{-7} S cm^{-1} (25 °C)	0.52 eV
$Li_{2.5}N_{0.5}S_{0.5}$[72]	Cubic ($Fm\bar{3}m$)	2.1×10^{-4} S cm^{-1} (27 °C)	0.35 eV
Li_7PN_4[75]	Cubic ($P\bar{4}3n$)	$1.83^a \times 10^{-7}$ S cm^{-1} (25 °C)	0.487 eV
$Li_{18}P_6N_{16}$[76]	Triclinic ($P\bar{1}$)	7.7×10^{-8} S cm^{-1} (25 °C)	0.497 eV
β-$Li_{10}P_4N_{10}$[77]	Trigonal ($R3$)	8.6×10^{-7} S cm^{-1} (25 °C)	0.41 eV
$LiPN_2$[75]	Tetragonal ($I\bar{4}2d$)	$2.1^a \times 10^{-9}$ S cm^{-1} (25 °C)	0.611 eV
$Li_{13}P_4N_{10}Br_3$[77]	Cubic ($Fm\bar{3}m$)	1.1×10^{-8} S cm^{-1} (25 °C)	0.61 eV
$Li_{13}P_4N_{10}Cl_3$[77]	Cubic ($Fm\bar{3}m$)	8.8×10^{-10} S cm^{-1} (25 °C)	0.72 eV

[a] The room-temperature ionic conductivity is calculated based on Arrhenius plots.

($Li_{12}P_3N_9$ (*Cc*), and $Li_5P_2N_5$ (*C*2/*c*)), the orthorhombic lattice (Li_4PN_3 (*Pccn*)), the tetragonal lattice ($LiPN_2$ ($I\bar{4}2d$)), the trigonal lattice (β-$Li_{10}P_4N_{10}$ (*R*3)), and the cubic lattice (Li_7PN_4 ($P\bar{4}3n$), α-$Li_{10}P_4N_{10}$ ($Fd\bar{3}m$). Among these compounds, $LiPN_2$, β-$Li_{10}P_4N_{10}$, Li_7PN_4 and $Li_{18}P_6N_{16}$ were investigated as lithium-ion conductors (see Fig. 6B and Table 3). The room-temperature ionic conductivity ranges from 10^{-9} S cm^{-1} to 10^{-7} S cm^{-1} and the activation energy ranges from 0.4 eV to 0.7 eV. The lithium-ion diffusion of these lithium nitridophosphates requires increasing mobile lithium-ion population and reducing lithium-ion migration energy barriers to further boost the room-temperature ionic conductivity. According to the PN_4 tetrahedra-based lattice structures, compositions' modification and aliovalent dopant elements to reduce the interaction between nitridophosphate groups and lithium ions and increase vacancy population.

2.5 Lithium nitride solid-state electrolytes with group 14 elements (C, Si and Ge)

Regarding the lithium nitrides containing carbon elements, several compounds have been reported up to now, including lithium cyanide (LiCN),[87] lithium cyanamide (Li_2CN_2),[88–90] lithium dicyanamide $Li[N(CN)_2]$,[91] lithium tricyanomethanide $Li[C(CN)_3]$,[92] lithium tetracyanoethylene $Li(C_6N_4)$.[93] LiCN displays a orthorhombic symmetric lattice (space group: *Pnma*),[94] while Li_2CN_2 crystalizes in a tetragonal space group of *I*4/*mmm*.[89] Regarding LiCN, it displays a crystal structure of edge-sharing $LiCN_3$ tetrahedra layers bonded by C–N bonds.[94] Li_2CN_2 consists of NCN sublattices and lithium ions locate at the central positions of LiN_4 tetrahedra, which share edges and form layer structures bonded by C atoms.[89,90,95] $Li[N(CN)_2]$ crystalizes in a monoclinic space group *P*2/*c* and contains edge-sharing LiN_4 tetrahedra and LiN_6 octahedra, which form one-dimensional chains.[91] In the case of $Li[C(CN)_3]$, it crystalizes in a orthorhombic space group *Ima*2, and zig-zag chains consisting of edge-sharing LiN_4 tetrahedra are connected by centered C4 triangles.[92] $Li(C_6N_4)$ shares the same space group (*P*2/*c*) with $Li[N(CN)_2]$ but consists of isolated LiN_4 tetrahedra which are C atoms.[93] Among these compounds, only Li_2CN_2 has been reported as a lithium-ion conductor however delivers low a room-temperature ionic conductivity of 1.1×10^{-6} S cm^{-1} when synthesized as a amorphous nitride (see Fig. 7B and Table 4).[96,97] When it crystalizes, the room-temperature ionic conductivity reduces to 4.6×10^{-10} S cm^{-1} (see Fig. 7B and Table 4). This low ionic conductivity might result from long lithium-ion migration pathways along the *c* axis while the edge-sharing LiN_4 tetrahedra is not a most migration-facilitating structure regarding layers perpendicular to the *c* axis. Amorphization can help accelerating lithium-ion diffusion in Li_2CN_2.

Up to now, several lithium nitridosilicates have been reported including $LiSi_2N_3$,[98,104–106] Li_2SiN_2,[98,107,108] Li_5SiN_3,[98,109,110] $Li_{21}Si_3N_{11}$,[98,99] $Li_{18}Si_3N_{10}$,[98] and Li_8SiN_4.[98,108] Among these compounds, crystal structures of $LiSi_2N_3$,[104,105] Li_2SiN_2,[107] Li_5SiN_3,[109,110] and $Li_{21}Si_3N_{11}$[99] has been resolved and summarized in Fig. 7A, which also displays the sublattices consisting of LiN_4, SiN_4, and (Li/Si)N_4 tetrahedra, while Li_8SiN_4 has not been resolved but should crystalize in an antifluorite-driven crystal structure.[98] $LiSi_2N_3$ crystalizes in a orthorhombic space group $Cmc2_1$ and consists of LiN_4 zig-zag chains and SiN_4 honeycomb rings.[104] In the case of Li_2SiN_2, it crystalizes in a orthorhombic space group *Pbca* and displays a lattice constructed by corner-sharing SiN_4 pyramid cages with lithium ions involved in several coordination geometries, including distorted trigonal LiN_3, distorted LiN_4 tetrahedra, and another five-coordinated geometry with N^{3+}.[107] Li_5SiN_3 and $Li_{21}Si_3N_{11}$ share the antifluorite structure with edge-sharing (Li/Si)N_4 tetrahedra, which is similar to the crystal structure of $Li_9N_2Cl_3$. While Li_5SiN_3 crystalizes in a cubic space group $Ia\bar{3}$,[110] $Li_{21}Si_3N_{11}$ crystalizes in a tetragonal space group *I*4.[99] Regarding the lithium-ion diffusion behavior in these lithium nitridosilicates, Yamene *et al.*[98,111] conducted the pioneering works regarding lithium-ion conduction in lithium nitridosilicates and firstly reported the ionic conductivity of $LiSi_2N_3$, Li_2SiN_2, Li_5SiN_3, $Li_{21}Si_3N_{11}$, $Li_{18}Si_3N_{10}$, and Li_8SiN_4 (see Fig. 7B and Table 4). The lithium nitridosilicates present low room-temperature ionic conductivities (10^{-6}–10^{-10} S cm^{-1} (25 °C)) and high activation energy (0.47–0.66 eV). The sluggish lithium migration behaviors should result from high lithium ion hopping energy (corner-sharing and edge-sharing lithium coordination geometries and long hopping distance between available lithium sites) and low mobile lithium-ion population (low defect population).

Isostructural to lithium nitridosilicates, several lithium nitridogermanates have been reported including $LiGe_2N_3$,[106,112] Li_2GeN_2,[112] Li_5GeN_3,[109,110,112] and Li_8GeN_4.[112] Among these compounds, the crystal structures of $LiGe_2N_3$ (orthorhombic, space group: $Cmc2_1$),[106,112] and Li_5GeN_3 (cubic, space group: $Ia\bar{3}$)[109,112] have been resolved with same space groups

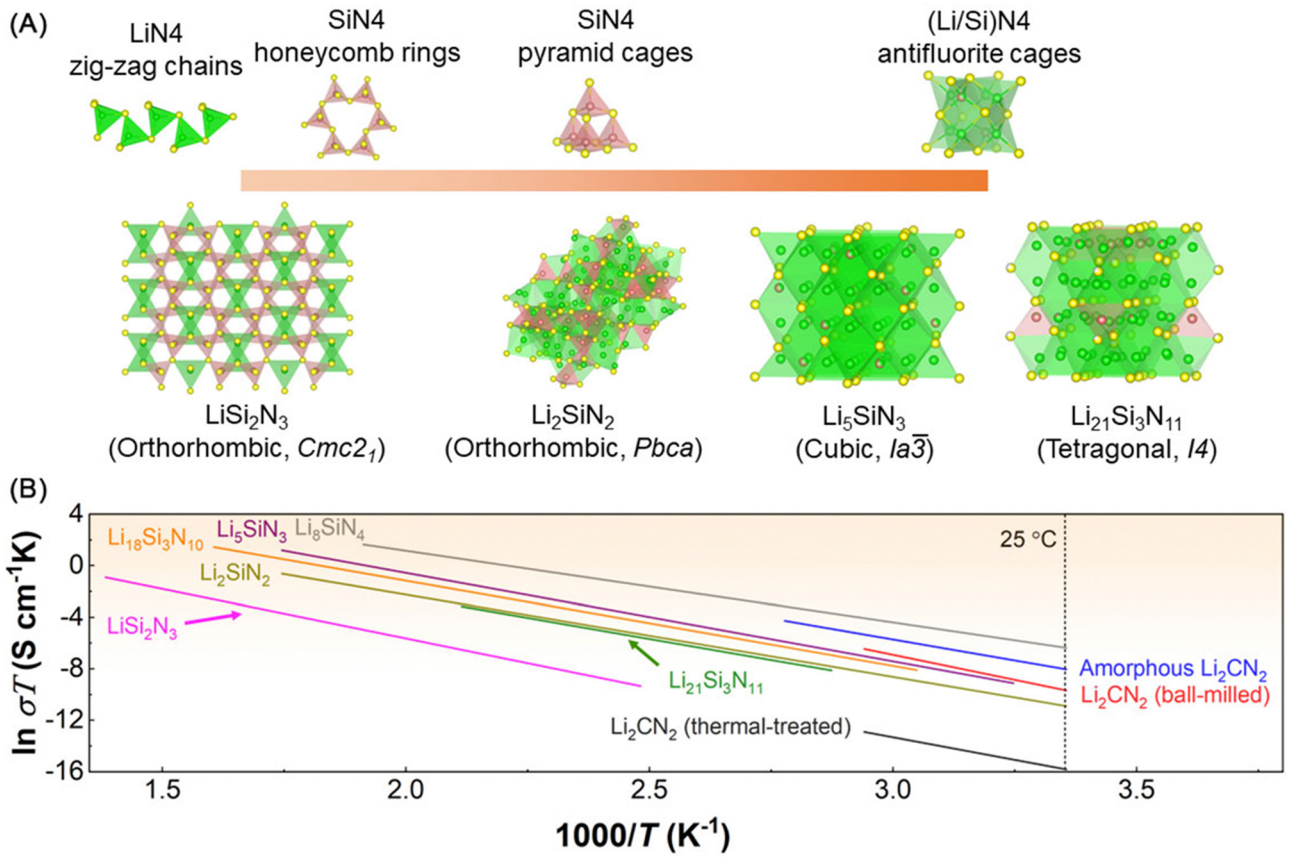

Fig. 7 (A) Crystal structures of a series of lithium nitridosilicates and their corresponding LiN_4, SiN_4, $(Li/Si)N_4$ tetrahedra networks, green: Li atoms, yellow: N atoms, red: Si atoms. (B) Arrhenius plots of amorphous Li_2CN_2,[96] Li_2CN_2 (ball-milled),[96] Li_2CN_2 (thermal-treated),[96] $LiSi_2N_3$,[98] Li_2SiN_2,[98] Li_5SiN_3,[98] $Li_{21}Si_3N_{11}$,[98] $Li_{18}Si_3N_{10}$,[98] and Li_8SiN_4.[98]

Table 4 Lithium nitride solid-state electrolytes with group 14 elements (C, Si, and Ge) and group 13 elements (B, Al, Ga, and In)

Lithium nitride solid-state electrolytes with group 14 elements (C, Si and Ge)			
Materials	Structures	Room-temperature ionic conductivity	Activation energy
Li_2NC_2 (thermal-treated)[96]	Tetragonal ($I4/mmm$)	4.6×10^{-10} S cm^{-1} (25 °C)	0.601 eV
Li_2NC_2 (ball-milled)[96]	Tetragonal ($I4/mmm$)	3.1×10^{-7} S cm^{-1} (25 °C)	0.674 eV
Amorphous Li_2NC_2[96]	Amorphous	1.1×10^{-6} S cm^{-1} (25 °C)	0.560 eV
$LiSi_2N_3$[98]	Orthorhombic ($Cmc2_1$)	$3.5^a \times 10^{-10}$ S cm^{-1} (25 °C)	0.663 eV
Li_2SiN_2[98]	Orthorhombic ($Pbca$)	6.3×10^{-8} S cm^{-1} (25 °C)	0.549 eV
Li_5SiN_3[98]	Cubic ($Ia\bar{3}$)	$1.8^a \times 10^{-7}$ S cm^{-1} (25 °C)	0.591 eV
$Li_{21}Si_3N_{11}$[98]	Tetragonal ($I4$)[99]	$4.5^a \times 10^{-8}$ S cm^{-1} (25 °C)	0.560 eV
$Li_{18}Si_3N_{10}$[98]	Antifluorite[c]	$1.4^a \times 10^{-7}$ S cm^{-1} (25 °C)	0.570 eV
Li_8SiN_4[98]	N/A[b]	5.9×10^{-6} S cm^{-1} (25 °C)	0.477 eV
Lithium nitride solid-state electrolytes with group 14 elements (B, Al, Ga and In)			
Materials	Structures	Room-temperature ionic conductivity	Activation energy
α-Li_3BN_2[100]	Tetragonal ($P4_2/mnm$)[c]	$1.3^a \times 10^{-10}$ S cm^{-1} (25 °C)	0.808 eV
β-Li_3BN_2[100]	Monoclinic ($P2_1/c$)	$1.0^a \times 10^{-9}$ S cm^{-1} (25 °C)	0.663 eV
Li_3BN_2 glass[101]	Amorphous	3.1×10^{-6} S cm^{-1} (25 °C)	0.455 eV
Li_3AlN_2[102]	Cubic ($Ia\bar{3}$)	5.0×10^{-8} S cm^{-1} (25 °C)	0.54 eV

[a] The room-temperature ionic conductivity is calculated based on Arrhenius plots. [b] Up to now, these compounds' crystal structures have not been resolved. [c] The originally reported space group (tetragonal, $P4_22_12$) of α-Li_3BN_2[100] was revised by Cenzual *et al.* to $P4_2/mnm$.[103]

comparing to their isostructural lithium nitridosilicates, while others crystal structures have not been resolved. However, up to now, no work reports the lithium-ion conductivity of these lithium nitridogermanates.

2.6 Lithium nitride solid-state electrolytes with group 13 elements (B, Al, Ga, and In)

Several lithium nitrides containing group 13 elements (*i.e.* B, Al, Ga, and In) have been reported but share the similar compound, Li_3MN_2 (M = B, Al, Ga, and In). In the case of Li_3BN_2, three phases have been reported, including α-Li_3BN_2 (tetragonal, space group: $P4_2/mnm$),[100,103] β-Li_3BN_2 (monoclinic, space group: $P2_1/c$),[100,113] and another new phase (tetragonal, space group: $I4_1/amd$).[114] For Li_3MN_2 (M: Al, Ga, and In), only one phase for each nitride compound, including: Li_3AlN_2 (cubic, space group: $Ia\bar{3}$),[109,115–118] Li_3GaN_2 (cubic, space group: $Ia\bar{3}$),[116,118,119] and Li_3InN_2 (non-resolved crystal structure).[120] Among these lithium nitrides containing group 13 elements, only α-Li_3BN_2, β-Li_3BN_2, and Li_3AlN_2 have been reported as lithium-ion conductors. However, the room-temperature ionic conductivity of crystalized compounds is low (10^{-8}–10^{-10} S cm^{-1}) and the activation energy is high (0.54–0.808 eV) (see Fig. 8D and Table 4). The unsatisfied lithium-ion conduction properties are due to their crystal structures consisting of LiN_4 and MN_4 (M = B, and Al) tetrahedra. The corner-sharing and edge-sharing tetrahedra sublattices hinder fast lithium-ion diffusion. Recently, one Li_3BN_2 glass delivered a higher room-temperature ionic conductivity of 3.1 × 10^{-6} S cm^{-1} with much lower activation energy of 0.455 eV owing to amorphization.[101] It suggests that creating defects or amorphization can help boosting lithium-ion diffusion in these compounds.

2.7 Other nitride solid-state electrolytes

In addition to these nitride solid-state electrolytes discussed above, other ternary lithium nitrides have reported, such as Li_3ScN_2 (cubic, space group: $Ia\bar{3}$),[121] Li_5TiN_3 (cubic, space group: $Ia\bar{3}$),[110] Li_2ZrN_2 (trigonal, space group: $P\bar{3}m1$),[122,123] Li_2HfN_2 (trigonal, space group: $P\bar{3}m1$),[123] α-Li_7VN_4 (tetragonal, space group: $P4_2/nmc$),[124] β-Li_7VN_4 (cubic, space group: $Pa\bar{3}$),[124] γ-Li_7VN_4 (cubic, space group: $P\bar{4}mn$),[124] Li_7NbN_4 (cubic, space group: $Pa\bar{3}$),[125] Li_7TaN_4 (cubic, space group: $Pa\bar{3}$),[126,127] *etc.*[79,128,129] Among these nitrides, only a few compounds have been reported lithium-ion conductors, such as Li_6MoN_4-Li_7NbN_4 solid-solutions, and Li_6WN_4-Li_7TaN_4 solid-solutions.[130] To explore promising nitride SSE candidates for all-solid-state lithium metal batteries, innovation of SSEs in terms of crystal structures, and ionic conductivity requires more efforts to screen nitrides and doping nitrides.

3. Synthesis methods of nitride solid-state electrolytes

Up to now, numerous nitride SSEs in terms of single crystals, polycrystal powder, and thin films have been prepared through several synthesis methods, including the Czochralski single crystal growth method, the solid-state reaction method, the phase transformation method, and the deposition method (including RF magnetron sputtering, pulsed laser deposition, ion beam assisted deposition, atomic layer deposition, and metal–organic chemical vapor deposition) (see Fig. 9 and Table 5). We will summarize these synthesis methods with a focus on compounds, crystal and local structures, and structure-driven lithium-ion conduction properties.

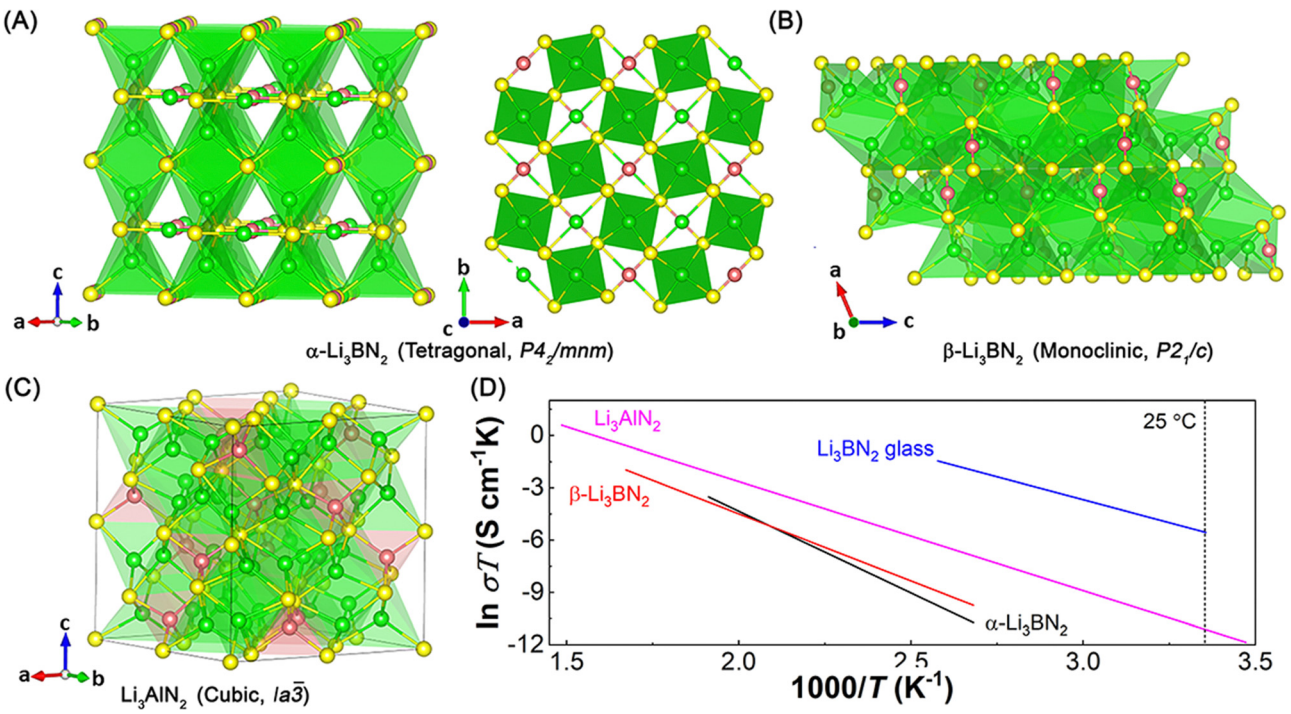

Fig. 8 Crystal structures of a series of lithium nitride solid-state electrolytes with group 13 elements (B, Al, Ga, and In): (A) Li_3BN_2 (green: Li atoms, yellow: N atoms, red: B atoms), (B) β-Li_3BN_2 (green: Li atoms, yellow: N atoms, red: B atoms), and (C) Li_3AlN_2 (green: Li atoms, yellow: N atoms, red: Al atoms). (D) Arrhenius plots of α-Li_3BN_2,[100] β-Li_3BN_2,[100] Li_3BN_2 glass,[101] and Li_3AlN_2.[102]

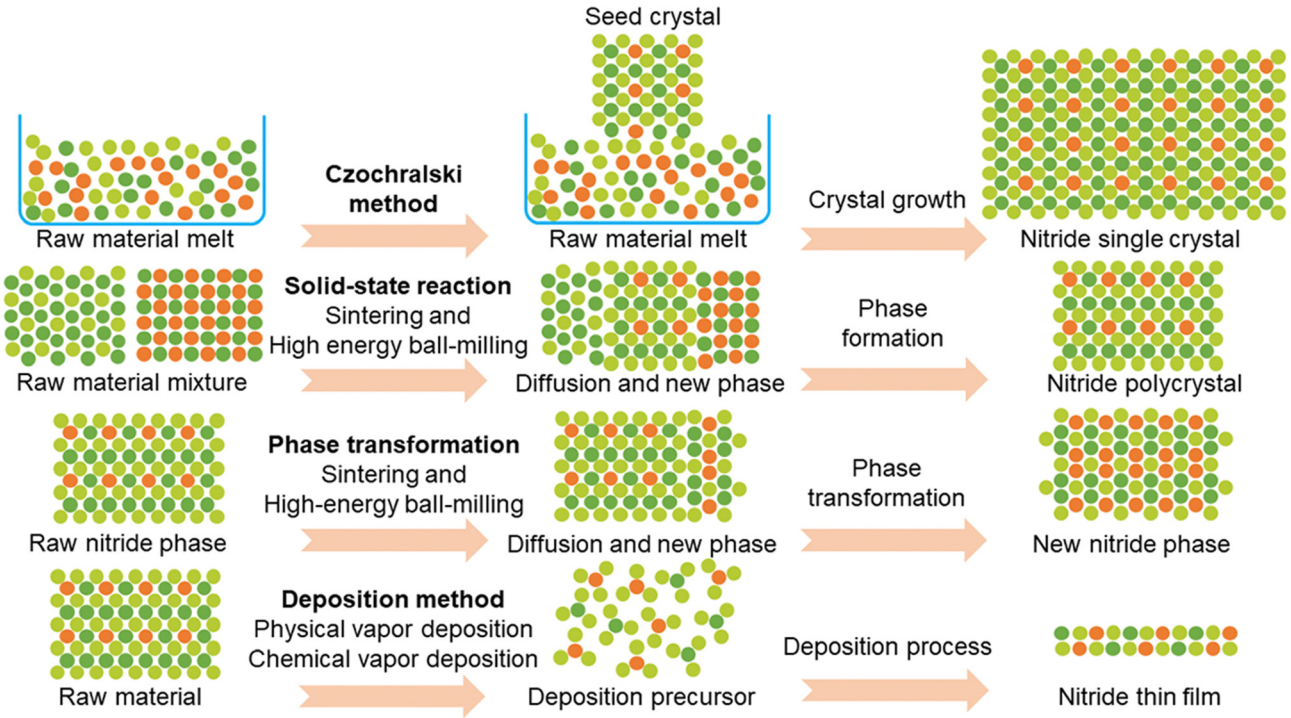

Fig. 9 Schematic illustration of synthesis methods of nitride SSEs, the Czochralski single crystal growth method, the solid-state reaction method, the phase transformation method, and the physical and vapor deposition methods (including radio frequency magnetron sputtering, pulsed laser deposition, ion beam assisted deposition, atomic layer deposition, and metal–organic chemical vapor deposition).

3.1 The Czochralski single crystal growth method

The Czochralski method is a general way to fabricate single crystals.[131] Fig. 9 shows the growth mechanism using raw material melt as the growth source of single crystals and seed crystals to guide the recrystallization process of melt to fabricate single crystals. In 1977, the α-Li_3N single crystal was fabricated by Schönherr and Müller[29] through this method and then its lithium ionic conductivity perpendicular and parallel to the *c* axis was measured by Alpen *et al.*[26] During this Czochralski growth process, Li_3N melt was placed in a deoxidized tungsten crucible and the growth chamber was filled with pure N_2, which was used to prevent decomposition of Li_3N melt at the melting temperature (814 °C). With the seed crystals, the growth rate of α-Li_3N single crystal was ~5 mm h^{-1} and the final single crystal product reached a large size up to 3 cm in diameter and 5 cm in length. To the best of our knowledge, this α-Li_3N single crystal was the only one reported large single crystal. As large single crystals help conduct studies of anisotropic properties (*e.g.*, anisotropic ionic conduction properties), which have been reported in oxide and sulfide SSEs,[132–135] the preparation of large single crystals of other nitride SSEs (*e.g.*, lithium nitride halide SSEs) is required and crucial to the development of nitride SSEs. In a short summary, this Czochralski single crystal growth method enables the production of high-quality single crystals with well-defined anisotropic properties, such as ionic conductivity, which is essential for fundamental studies and advanced characterization. However, the method requires high temperatures and controlled environments (*e.g.*, pure N_2 atmosphere) to prevent decomposition of nitride materials. Additionally, the process is time-intensive and limited in scalability, making it unsuitable for large-scale production (see Table 6).

3.2 Solid-state reaction and phase transformation methods

Among these reported methods, the solid-state reaction and phase transformation methods are the most common synthesis strategies. Fig. 9 shows the progress mechanism of these two methods. In the case of this solid-state reaction, once raw materials are mixed together and different compounds contact each other, interdiffusion of atoms and solid-state reactions can be observed theoretically but require external driven forces, such as a high-temperature or a high-pressure environment.[136] Regarding SSEs, the high-temperature environment achieves two synthesis strategies, sintering (*e.g.*, oxides and sulfides),[137,138] and co-melting (halides).[139,140] Due to the high melting point of Li_3N (*i.e.*, 814 °C), the solid-state reaction method with sintering is usually conducted to prepared nitride SSEs, such as lithium nitride halide.[58,59,64,65] Li_3N and corresponding lithium halides (*e.g.*, LiCl, LiBr, and LiI) were mixed together based on the stoichiometric ratio as raw materials, which were then sintered at specific temperature. To prevent Li_3N from decomposing at high temperature, this sintering process were conducted under a pure N_2 environment. The final products were corresponding lithium nitride halide SSEs. As discussed in the section of lithium nitride halide SSEs, the phase diagrams provide guidelines to the synthesis process, including compositions and required temperature (see Fig. 5A–C). In addition to high temperature, mechanical milling-driven high pressure also acts as a driven-force to promote

Table 5 Typical synthesis methods of nitride solid-state electrolytes

Synthesis method	Nitride SSEs	Ionic conductivity
Czochralski method (single crystals)		
	α-Li_3N[26]	1.2×10^{-3} S cm^{-1} (300 K) $\perp c$
		1.0×10^{-5} S cm^{-1} (300 K) $\parallel c$
	H-doped α-Li_3N[25]	6.0×10^{-3} S cm^{-1} (25 °C) $\perp c$
Solid-state reaction		
Sintering	$Li_9N_2Cl_3$[58]	2.3×10^{-6} S cm^{-1} (25 °C)
	Li_6NBr_3[64]	$6.59^a \times 10^{-8}$ S cm^{-1} (25 °C)
	Li_5NI_2[59]	$1.0^a \times 10^{-7}$ S cm^{-1} (25 °C)
	Li_3N–LiI–LiOH[65]	9.5×10^{-4} S cm^{-1} (25 °C)
	Li_7PN_4[75]	$1.83^a \times 10^{-7}$ S cm^{-1} (25 °C)
	$LiPN_2$[75]	$2.1^a \times 10^{-9}$ S cm^{-1} (25 °C)
	$Li_{18}P_6N_{16}$[76]	7.7×10^{-8} S cm^{-1} (25 °C)
	β-$Li_{10}P_4N_{10}$[77]	8.6×10^{-7} S cm^{-1} (25 °C)
	$Li_{13}P_4N_{10}Br_3$[77]	1.1×10^{-8} S cm^{-1} (25 °C)
	$Li_{13}P_4N_{10}Cl_3$[77]	8.8×10^{-10} S cm^{-1} (25 °C)
	$LiSi_2N_3$[98]	$3.5^a \times 10^{-10}$ S cm^{-1} (25 °C)
	Li_2SiN_2[98]	6.3×10^{-8} S cm^{-1} (25 °C)
	Li_5SiN_3[98]	$1.8^a \times 10^{-7}$ S cm^{-1} (25 °C)
	$Li_{21}Si_3N_{11}$[98]	$4.5^a \times 10^{-8}$ S cm^{-1} (25 °C)
	$Li_{18}Si_3N_{10}$[98]	$1.4^a \times 10^{-7}$ S cm^{-1} (25 °C)
	Li_8SiN_4[98]	5.9×10^{-6} S cm^{-1} (25 °C)
	α-Li_3BN_2[100]	$1.3^a \times 10^{-10}$ S cm^{-1} (25 °C)
	β-Li_3BN_2[100]	$1.0^a \times 10^{-9}$ S cm^{-1} (25 °C)
Mechanical milling	Vacancy-rich $Li_9N_2Cl_3$[16]	4.3×10^{-5} S cm^{-1} (25 °C)
	$Li_{2.5}N_{0.5}S_{0.5}$[72]	2.1×10^{-4} S cm^{-1} (27 °C)
	Amorphous Li_2NC_2[96]	1.1×10^{-6} S cm^{-1} (25 °C)
	Li_2NC_2 (ball-milled)[96]	3.1×10^{-7} S cm^{-1} (25 °C)
	Li_3BN_2 glass[101]	3.1×10^{-6} S cm^{-1} (25 °C)
	Li_3AlN_2[102]	5.0×10^{-8} S cm^{-1} (25 °C)
Mechanical milling and sintering	Li_7N_2I[66]	3.1×10^{-4} S cm^{-1} (25 °C)
	Li_7N_2I–0.5LiOH[67]	5.2×10^{-4} S cm^{-1} (25 °C)
	Li_9S_3N[71]	8.3×10^{-7} S cm^{-1} (25 °C)
	Li_2NC_2 (thermal-treated)[96]	4.6×10^{-10} S cm^{-1} (25 °C)
Phase transformation		
Sintering	α-Li_3N sinter[27]	1.5×10^{-3} S cm^{-1} (300 K)
Mechanical milling	β-Li_3N[28]	2.085×10^{-4} S cm^{-1} (25 °C)
	Vacancy-rich β-Li_3N[15]	2.14×10^{-3} S cm^{-1} (25 °C)
Physical and chemical vapor deposition		
	$Li_{3.3}PO_{3.9}N_{0.17}$[30]	2.2×10^{-6} S cm^{-1} (25 °C)
	$Li_{2.9}PO_{3.3}N_{0.46}$[31]	3.3×10^{-6} S cm^{-1} (25 °C)
	$Li_{1.35}Si_{0.79}P_{0.21}O_{1.96}N_{0.96}$[32]	2.06×10^{-5} S cm^{-1} (25 °C)
	$Li_{2.9}Si_{0.35}PO_{1.5}N_{1.26}$[33]	1.24×10^{-5} S cm^{-1} (25 °C)
	LiBPON[34]	3.5×10^{-6} S cm^{-1} (25 °C)
	LiPSON[35]	1.58×10^{-5} S cm^{-1} (25 °C)
	LiLaAlPON[36]	1.47×10^{-5} S cm^{-1} (25 °C)

[a] The room-temperature ionic conductivity is calculated based on Arrhenius plots.

atoms interdiffusion, and high-energy ball-milling is usually used to prepare SSEs. The high-energy ball-milling can not only provide a high-pressure environment but also pulverise and mix raw materials, which together trigger solid-state reaction between

Table 6 Comparison of synthesis methods for nitride SSEs

Synthesis method	Advantages	Disadvantages	Suitable forms
Czochralski growth (single crystals)	• High-quality single crystals • Enables study of anisotropic properties	• High temperatures; controlled environments • Time-intensive • Low scalability	Single crystals
Solid-state reaction and phase transformation	• Versatile • Compatible with large-scale production • Suitable for various nitride SSEs	• High temperatures or mechanical forces may induce side reactions • Moisture-sensitive precursors	Polycrystalline powders
Physical and chemical vapor deposition	• Precise control over film composition and thickness • Suitable for thin films and micro-devices	• Expensive • Less scalable • Complex processing conditions • Limited to thin-film applications	Thin films

raw materials, such as the preparation process of this vacancy-rich $Li_9N_2Cl_3$.[16] During this ball-milling process, Li_3N and LiCl were starting materials and placed in the ball-milling jars. Along with the high-energy ball-milling process, Li_3N and LiCl started to react with each other and thus this vacancy-rich $Li_9N_2Cl_3$ SSE was obtained. As Li_3N is sensitive to moisture, the whole preparation process was conducted under Ar including raw materials and the ball-milling process. In the case of ball-milling-driven vacancy-rich lattices in this vacancy-rich $Li_9N_2Cl_3$, the formation mechanism and effect on lithium-ion diffusion will be discussed in the phase transformation method section. In some cases, mechanical milling is also used to generate precursor mixtures before subsequent sintering, as demonstrated by Li_7N_2I-based compounds,[66,67] thus showcasing the versatility of mechanical milling for preparing SSEs.

The phase transformation method mechanism is similar to that of solid-state reaction and requires self-diffusion of atoms in origin phases to form new phases, where no solid-state reaction happens among different raw materials (see Fig. 9). Fig. 3A shows a phase diagram of Li_3N at different temperature and pressure. The phase transformation from β-Li_3N to α-Li_3N under high temperature started at ~200 °C and almost completed at ~400 °C.[24] While high pressure also induce a phase transformation from α-Li_3N to β-Li_3N, which started at ~0.6 GPa and underwent another phase transformation to γ-Li_3N at ~40 GPa.[40,42] According to this phase diagram, α-Li_3N and β-Li_3N SSEs have been prepared by the sintering method and the high-energy ball-milling method.[28] In the case of β-Li_3N, Li *et al.*[15] reported vacancy-rich β-Li_3N SSEs prepared from raw commercial Li_3N (a mixture of α-Li_3N and β-Li_3N) by the high-energy ball-milling method. The formation mechanism of a vacancy-rich phase in β-Li_3N is due to the weak interaction between Li^+ and N^{3-} (see Fig. 10A) and the high-energy ball-milling process results in increase of Li and N vacancy population. As the Arrhenius equation can describe the lithium-ion diffusion behavior in SSEs, the determining parameters of ionic conductivity regarding crystal and local structures are activation energy (E_a) and mobile lithium-ion concentration (n) (see Fig. 10B). The vacant N sites reduce the hopping energy of lithium ions between available sites and thus lower the activation energy. Furthermore, the vacant Li sites provide available lithium-ion hopping sites and increase the concentration of mobile lithium ions. The lower E_a and the higher n contribute to higher ionic conductivity, which reaches up to 2.14×10^{-3} S cm^{-1} (see Fig. 3E and 10C). The vacancy-driven improvement of ionic conductivity has been also observed in the reported $Li_9N_2Cl_3$ prepared by the high-energy ball-milling method.[16]

In a short summary, these solid-state reaction and phase transformation methods are versatile and widely applicable to synthesize various nitride SSEs, such as lithium nitride halides and vacancy-rich compounds. High-temperature sintering or high-energy ball-milling enables efficient mixing and reaction of raw materials, and the methods are compatible with large-scale production. However, high temperatures or mechanical

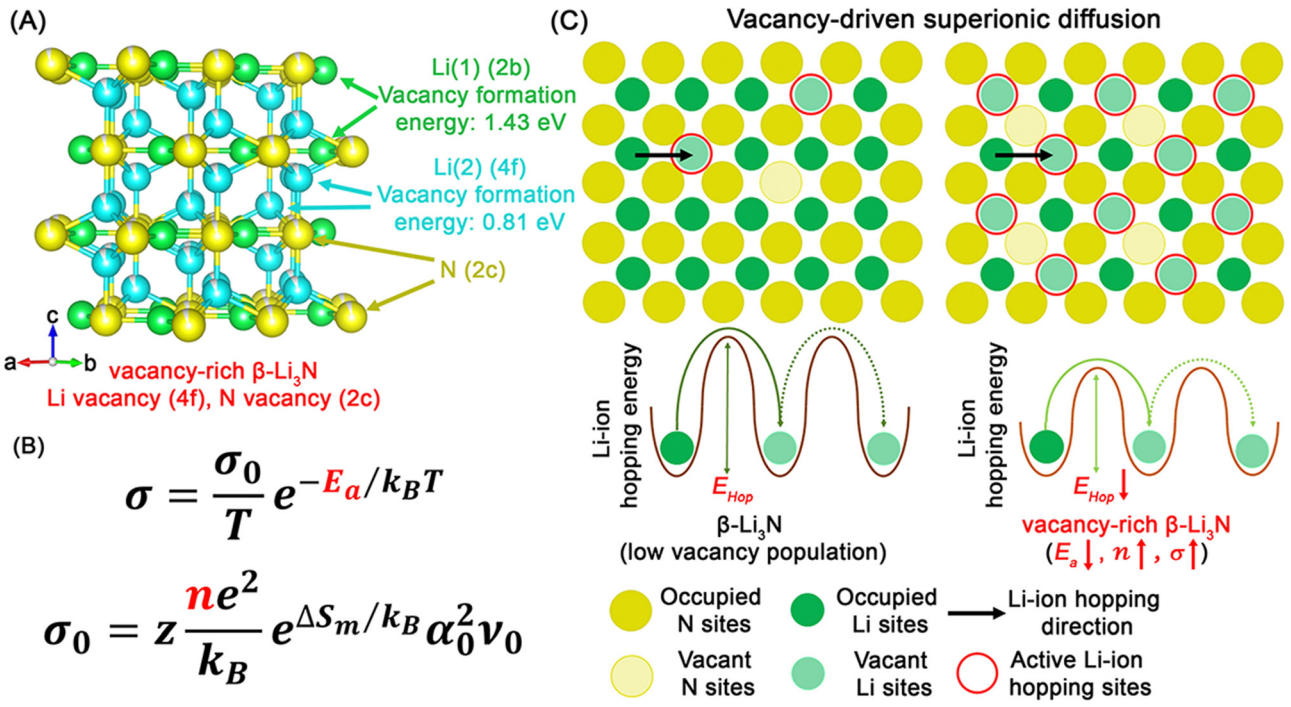

Fig. 10 (A) Crystal structure of vacancy-rich β-Li_3N and the calculated formation energy of single neutral lithium vacancy at 2c and 4f sites, respectively. (B) Arrhenius relationship used to describe lithium-ion conduction, σ_0 the pre-factor, T the temperature, E_a the activation energy for lithium-ion conduction, k_B the Boltzmann constant, z the geometric factor, n the concentration of mobile lithium ions, ΔS_m the entropy of lithium-ion hopping, α_0 the lithium-ion hopping distance, and ν_0 the attempt frequency. (C) Schematic illustration of vacancy-driven superionic diffusion mechanism of vacancy-rich β-Li_3N. Reproduced with permission.[15]

forces may lead to undesired side reactions or loss of phase purity. Moisture sensitivity of nitride precursors necessitates stringent control of environmental conditions, such as Ar or N_2 atmospheres, during the process (see Table 6).

3.3 Physical and chemical vapor deposition methods

In addition to nitride SSEs single crystals and polycrystal powder, LiPON and derivative solid-state electrolytes are usually fabricated in the form of deposited thin films (see Fig. 9). Since the initial report of LiPON thin film prepared by radio frequency magnetron sputtering,[30,31] several deposition methods have been conducted, including pulsed laser deposition,[141] ion beam assisted deposition,[142] atomic layer deposition,[143,144] and metal–organic chemical vapor deposition.[145] In the case of physical vapor deposition strategies (*i.e.*, radio frequency magnetron sputtering, pulsed laser deposition, and ion beam assisted deposition), Li_3PO_4 solid targets transfer to gas phases and then deposited on the substrates with N_2 gas as the source of N. Among these physical vapor deposition process, N_2 gas pressure, substrate temperature, and transition rate of Li_3PO_4 targets to gas determine the compositions and ionic conductivity of LiPON films.[53,146] Through the physical vapor deposition method, a LiPON thin film with the composition of $Li_{2.9}PO_{3.3}N_{0.46}$ prepared by radio frequency magnetron sputtering achieves high room-temperature ionic conductivity of 3.3×10^{-5} S cm^{-1}.[31] The deposition progress of the physical vapor deposition makes it unsuitable for substrates with complex shapes (*e.g.* foams), while the chemical vapor deposition strategies (atomic layer deposition, and metal–organic chemical vapor deposition) overcome this challenge by depositing LiPON film on substrates' surface with chemical reactions. In the case of a typical atomic layer deposition process, lithium *tert*-butoxide, deionized H_2O, trimethylphosphate, and plasma N_2 work as deposition precursors[144] and then form LiPON thin films. While other precursors have also been reported to use in the atomic layer deposition process, lithium hexamethyldisilazide and diethyl phosphoramidate were used in the deposition cycles of LiPON.[143] The metal–organic chemical vapor deposition method is another chemical vapor deposition strategy to fabricate LiPON thin film with lithium dipivaloylmethane, triethyl phosphate, and NH_3 as precursor materials.[145] In a short summary, this deposition methods are particularly suitable for fabricating thin-film SSEs, such as LiPON and its derivatives, with precise control over film composition and thickness. These methods allow the integration of SSEs onto various substrates, enabling applications in micro-batteries and thin-film devices. However, physical vapor deposition (*e.g.*, RF magnetron sputtering) is less suitable for substrates with complex geometries, whereas chemical vapor deposition methods (*e.g.*, atomic layer deposition) are more versatile but involve complex precursor selection and processing conditions. Additionally, deposition methods are relatively expensive and less scalable compared to bulk synthesis techniques (see Table 6).

4. Chemical and electrochemical stability

Nitride SSEs have been developed to overcome the lithium metal–SSE interfacial challenges. Taking all-solid-state lithium metal batteries into account, the stability of nitrides including thermal stability, air stability, and chemical and electrochemical stability with electrodes are crucial to safety, electrochemical, working life performance. Recent reported results regarding stability studies will be summarized and the influences on all-solid-state lithium metal batteries will also be discussed and emphasized in this section.

4.1 Thermal stability

Conventional lithium-ion batteries with liquid electrolytes can meet serious safety issues when temperature increases, such as failure and thermal runaway.[5,147] Along with increasing temperature, solid electrolyte interphases begin to decompose with the release of gas (CO_2, O_2, C_2H_4, *etc.*) (80–120 °C). Then polymer separators will melt (~130 °C) and it can induce internal short-circuit. The further increasing temperature can trigger the decomposition of cathode materials and release of O_2. All count for safety issues of conventional lithium-ion batteries.[148] One promising solution is to replace liquid electrolytes and polymer separators with SSEs, which are usually considered to be stable at high temperature. Therefore, the thermal stability of nitride SSEs and nitride–lithium metal interfaces is crucial to evaluate the safety of all-solid-state lithium metal batteries.[148] Up to now, just a few reports studied the unusual ionic conductivity variation as a function of temperature.[59] Two lithium nitride halides ($Li_{13}N_4Br$, and Li_5NI_2) displayed phase transformation at around 200–250 °C (see Fig. 5E). Vacancy-rich $Li_9N_2Cl_3$ display decrease of room-temperature ionic conductivity with thermal treatment at 150–250 °C.[16] However, no report presents the variation of crystal or local structures of nitride SSEs upon elevated temperature and the nitride–lithium metal interfacial thermal stability has not been reported either. Therefore, more efforts are required to study the thermal stability of not only nitride SEEs but also nitride–lithium metal interfaces to evaluate the safety performance of all-solid-state lithium metal batteries.

4.2 Air stability

The air stability of nitride SSEs is a critical factor that determines their storage and manufacturing environments. Lithium nitride (Li_3N), like many nitride-based SSEs, exhibits sensitivity to moisture in the air, leading to surface reactions that compromise its stability and performance. When exposed to ambient air, lithium nitride reacts with moisture, forming LiOH and other byproducts, often accompanied by exothermic reactions that exacerbate degradation. This behavior mirrors the moisture sensitivity observed in other SSEs, such as sulfides and halides, which release toxic gases like H_2S and HCl upon exposure to humid air.[149–151] As reported, dry rooms promise reasonable environment for manufacturing of sulfide-based all-solid-state lithium batteries.[152] In the case of nitride SSEs, Li *et al.* reported the studies of air stability of vacancy-rich β-Li_3N[15] and vacancy-rich $Li_9N_2Cl_3$ SSEs[16] through *operando* synchrotron-based X-ray diffraction (SXRD) and *in situ* X-ray absorption fine structure (XAFS) studies (see Fig. 11A and B).[151] In the case of *operando* and *in situ* XRD studies of vacancy-rich

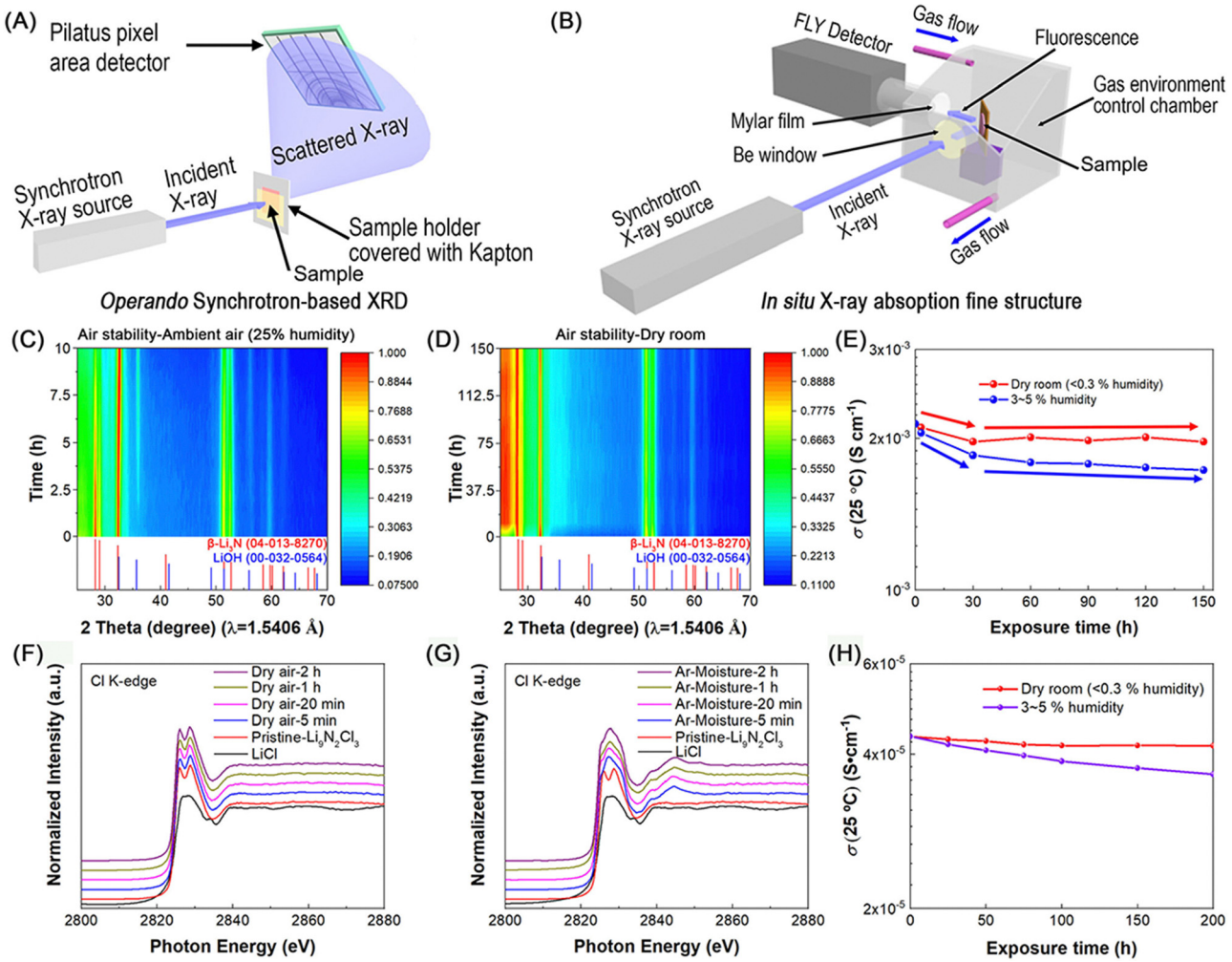

Fig. 11 Schematic illustration of (A) *operando* synchrotron-based X-ray powder diffraction (SXRD) study and (B) *in situ* synchrotron-based X-ray absorption fine structure (XAFS) study of air stability of SSEs. Reproduced with permission,[151] Copyright © 2020, American Chemical Society. (C)–(E) Air stability study of vacancy-rich β-Li_3N: (C) *operando* X-ray diffraction pattern evolution of vacancy-rich β-Li_3N during exposure process to air with 25% relative humidity for 10 h. (D) *In situ* X-ray diffraction pattern evolution of vacancy-rich β-Li_3N upon different exposure times in a dry room with a low dew point of −50 to −60 °C (<0.3% relative humidity) for 150 h. (E) The lithium-ion conductivity evolution at 25 °C of vacancy-rich β-Li_3N after different exposure times in a dry room with a low dew point of −50 to −60 °C (<0.3% relative humidity) and ambient air with 3–5% humidity level for 150 h. Reproduced with permission.[15] (F)–(H) Air stability study of vacancy-rich $Li_9N_2Cl_3$: *in situ* Cl K-edge XANES studies of vacancy-rich $Li_9N_2Cl_3$ during exposure process to (F) dry air and (G) the mixture of Ar and moisture for 2 h, (H) the lithium-ion conductivity evolution at 25 °C of vacancy-rich $Li_9N_2Cl_3$ upon exposure to dry air. Reproduced with permission.[16]

β-Li_3N SSEs,[15] LiOH forms on the surface and works as protection layers preventing further degradation in ambient air (25% humidity), while β-Li_3N SSEs maintain the main phase without obvious formation of LiOH upon exposure to dry room for 150 h and high room-temperature ionic conductivity of $>10^{-3}$ S cm^{-1} upon exposure to dry room and 3–5% humidity for 150 h (see Fig. 11C–E). For vacancy-rich $Li_9N_2Cl_3$ SSEs,[16] *operando* XAFS studies indicate that this nitride SSE is stable to dry air but sensitive to moisture and can maintain high room-temperature ionic conductivity when stored in dry rooms or low humid environment. These two studies suggest that these two nitride SSEs also promise good manufacturing properties in industrial dry rooms, while the decrease of ionic conductivity in dry rooms should result from degradation. The air stability of nitrides requires further improvement through innovation of degradation mechanism studies and structural and composition optimization to meet ultimate requirements for battery manufacturing industries (*e.g.*, stable for months or years).

4.3 Interfacial stability in all-solid-state lithium metal batteries

In addition to SSEs and electrodes, the interfacial stability (chemical and electrochemical stability, mechanical stability, and thermal stability) is also crucial to the electrochemical performance and safety issues of all-solid-state lithium metal batteries.[6,153] Regarding the configuration of all-solid-state lithium metal batteries (see Fig. 1), several interfaces are formed, including SSE–electrode (*i.e.*, lithium metal anode, and cathodes) interfaces, SSE–SSE interlayer interfaces, and electrode–current collector interfaces. Among these interfaces,

the SSE-related interfaces are mainly determined by electrochemical windows, extended by kinetic-originated overpotential and formed interphases (see Fig. 2A, 12A, and B). Interfacial resistance contributes to electrochemical performance and interfacial stability determines the working stability and life of all-solid-state lithium metal batteries. Fig. 2A and 12B show the calculated thermodynamic intrinsic electrochemical windows of nitride SSEs, which possess stable windows of 0–1.0 V (*vs.* Li/Li^+) for most nitrides (*e.g.*, Li_3N (0–0.48 V *vs.* Li/Li^+), $Li_9N_2Cl_3$ (0–0.50 V *vs.* Li/Li^+)) and a narrow stable window for LiPON (0.69–1.07 V *vs.* Li/Li^+).[15,16] Due to forming electronic insulating phases, the stable windows of $Li_9N_2Cl_3$ are extended to 0–1.68 V *vs.* Li/Li^+. LiPON also display stable window extension to 0–4.82 V *vs.* Li/Li^+ if the formation of gas from interfaces cannot pulverize and break down this LiPON layers at higher voltage,[154] which is consistent with the application of LiPON in all-solid-state lithium metal batteries.[17,55]

As most nitrides decompose at high voltage close to 4.0 V, only LiPON has been reported to be employed as nitride SSE layers for cathode materials up to now.[17,55,156] As discussed, LiPON also decomposes after the voltage reaches higher than 1.07 V *vs.* Li/Li^+, while the theoretical thermodynamic calculation,[154,155] XPS,[156] and cryogenic electron microscopy experimental results[157] present the formation of stable LiPON–cathode interphases (nitrogen-containing species for lithium cobalt oxide cathodes, and no obvious decomposition for spinel-type $LiNi_{0.5}Mn_{1.5}O_4$). And the formed interphases prevent further decomposition of LiPON and provide rational lithium-ion diffusion pathways, which account for long working life of LiPON-based all-solid-state lithium metal batteries up to 10 000 cycles.[17]

For the lithium metal anode side, LiPON and other nitrides have been reported to be promising SSE candidates for all-solid-state lithium metal batteries. While most nitride SSEs (*e.g.*, Li_3N, $Li_9N_2Cl_3$) show thermodynamic stability towards lithium metal, LiPON stabilizes lithium metal anodes through forming rational LiPON–lithium metal interphases. To study the interfacial stability towards lithium metal anodes, Li *et al.*,[15,16] Schwöbel *et al.*,[158] Cheng *et al.*,[159] and Hood *et al.*[160] developed *operando* & *ex situ* X-ray analytical techniques and *in situ* transmission electron microscopy (TEM) strategies (see Fig. 13). Owing to the low angle of incidence X-rays, the scattered X-rays and fluorescent X-rays mainly come from the interfaces and can track evolution of crystal phases and chemical environment of interphases in real time (see Fig. 13A–C). The *operando* SXRD and XAFS results indicate that vacancy-rich $Li_9N_2Cl_3$ is stable towards lithium metal anode during contact and lithium stripping & plating processes (see Fig. 13D–G).[16] Li *et al.*[15] also carried out synchrotron X-ray based scanning transmission X-ray microscopy (STXM) to present the high stability of vacancy-rich β-Li_3N towards lithium metal. Compared to X-ray based analytical techniques, electron

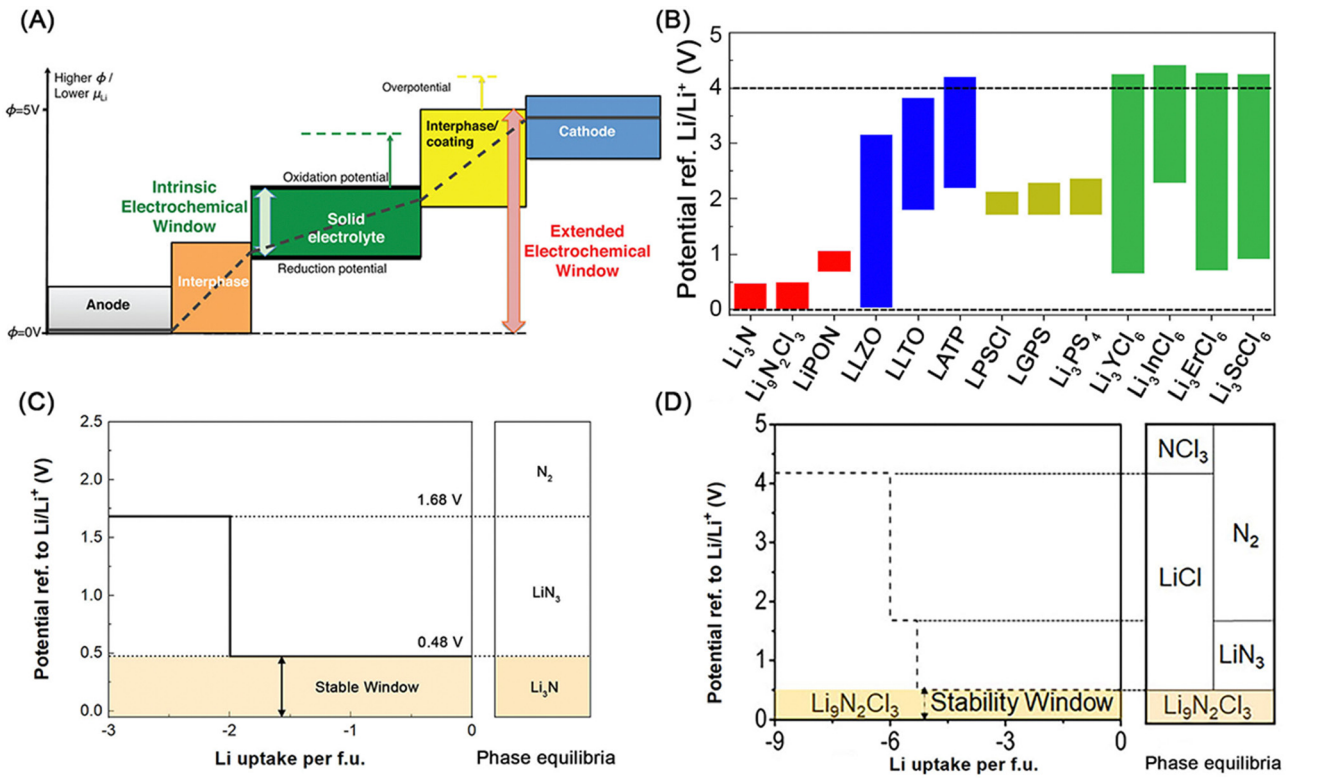

Fig. 12 (A) Schematic diagram about the electrochemical window (color bars) and the Li chemical potential profile (black line) in the all-solid-state lithium-ion battery. The electrochemical window is extended by the overpotential and the formed interphases. Reproduced with permission,[155] Copyright © 2015 American Chemical Society. (B) Calculate thermodynamics intrinsic electrochemical windows of vacancy-rich β-Li_3N, vacancy-rich $Li_9N_2Cl_3$, LiPON, and other common SSEs, including oxides, sulfides, and halides. Calculated thermodynamic equilibrium voltage profile and phase equilibria of (C) vacancy-rich β-Li_3N and (D) vacancy-rich $Li_9N_2Cl_3$. Reproduced with permission.[15,16]

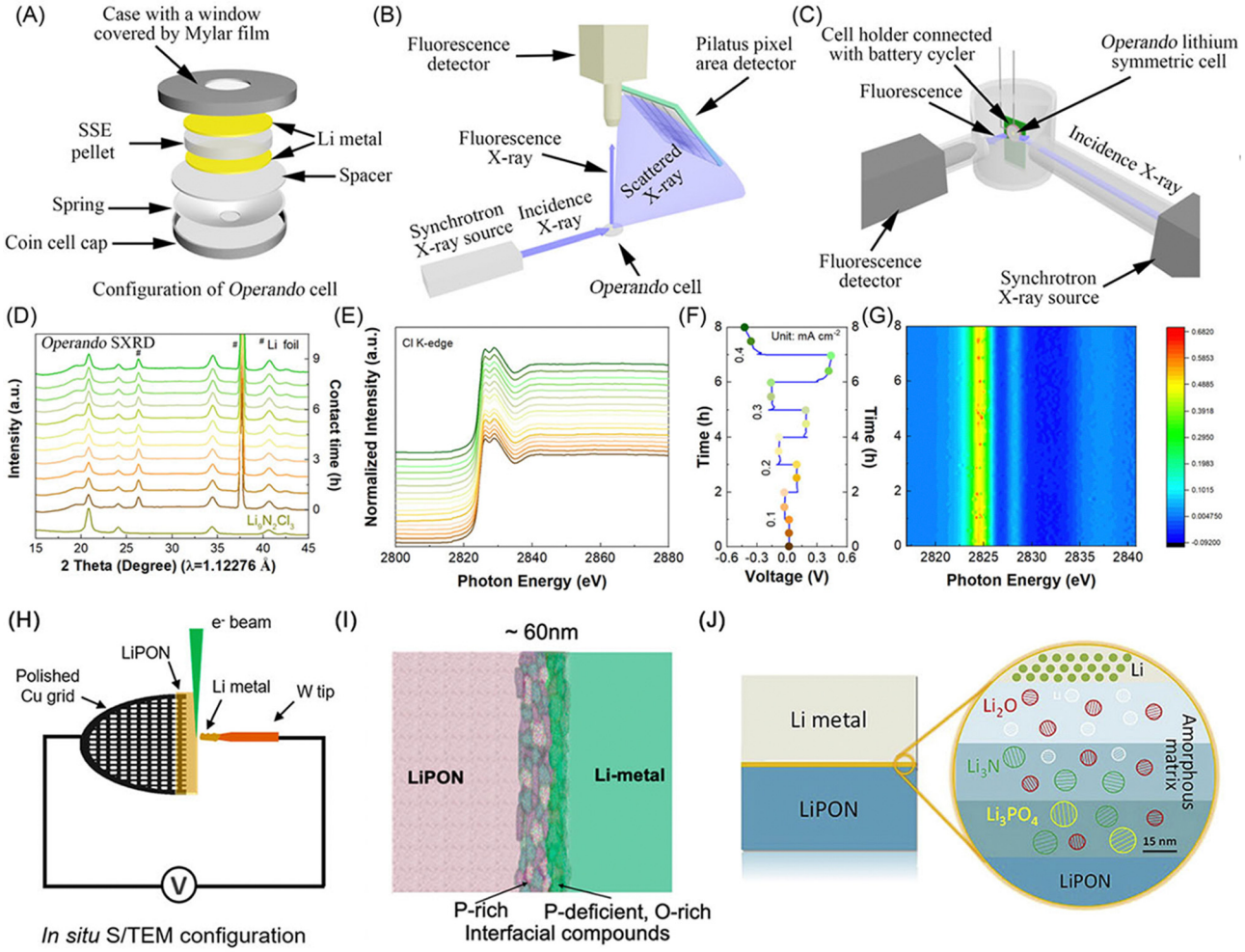

Fig. 13 Schematic illustration of the configuration of (A) the *operando* cell and (B) and (C) the *operando* SXRD and XAFS studies of chemical stability of SSEs towards lithium metal anode. (D) *Operando* SXRD pattern evolution of $Li_9N_2Cl_3$ during contact with lithium metal for several hours. (E) *Operando* XAFS spectra at Cl K-edge with (F) the corresponding discharge/charge voltage profiles of the Li cycling in the *operando* cell at several current densities (*i.e.*, 0.1, 0.2, 0.3, and 0.4 mA cm^{-2}) and (G) with first derivative mapping of $Li_9N_2Cl_3$ during lithium plating/stripping process. Reproduced with permission.[16] (H) Experimental setup for observing the interface between LiPON and lithium metal using *in situ* TEM and (I) schematic representation of the interphase formation between LiPON and lithium metal. Reproduced with permission,[160] Copyright © 2021, American Chemical Society. (J) Schematic of Li/LiPON multilayered interphase obtained by employing cryogenic electron microscopy (cryo-EM) and XPS depth profiling. Reproduced with permission,[159] Copyright © 2020 Published by Elsevier Inc.

microscopy not only presents chemical environment of the interphases but also achieves high spatial resolution and provides spatial distribution in the interphases (see Fig. 13H–J). Cheng *et al.*,[159] conducted *in situ* TEM and found that the LiPON–lithium metal interphase consists of two sub-layers of corresponding binary compounds (most likely Li_3N, Li_3P and Li_2O), where P-rich interphases are formed close to the LiPON side, while P-deficient, O-rich interphases are observed close to the lithium metal side (see Fig. 13H and I). Hood *et al.*[160] reported similar results for the LiPON–lithium metal interphases but present the distribution of interfacial reaction products (*i.e.*, Li_2O, Li_3N, and Li_3PO_4) with N and P gradients as shown in Fig. 13J. These two reports indicate that the combination of interfacial reaction products of LiPON and lithium metal forms a kinetic stable interface for lithium metal, which is the origin of LiPON employed as key SSEs for lithium metal anodes in all-solid-state batteries.[17,157,161,162]

Achieving stable interfaces between SSEs and electrodes is vital for ensuring the long-term performance and safety of all-solid-state lithium metal batteries. For electrochemical stability, selecting SSEs with suitable stability windows and applying protective coatings, such as LiPON or lithium nitride, is essential to mitigate adverse reactions and extend operational voltage ranges. Chemical stability can be enhanced through interfacial engineering techniques, including chemical doping and surface treatments, which stabilize interphases and inhibit undesirable reactions. To optimize interfacial conductivity, it is crucial to minimize resistance by incorporating conductive interlayers or designing interfaces with tailored structures that facilitate efficient ion and electron transport. Furthermore,

mechanical stability must be addressed by optimizing the mechanical properties of SSEs, such as modulus and fracture toughness, to prevent dendrite formation and accommodate volume changes. The use of buffer layers or compliant interlayers can effectively relieve mechanical stress and maintain consistent contact at the interfaces, further enhancing system stability.

Furthermore, taking narrow electrochemical windows of nitrides close to 0 V *vs.* Li/Li^+ into account, most nitride SSEs are usually required to be coupled with other cathode-stable SSEs. The nitride-other SSE interface and its resistance and stability will affect the batteries performance and safety, however, which haven't been studied in all-solid-state lithium metal batteries. Even for the nitride–electrode interfaces, the studies of interfacial stability regarding mechanical and thermal properties are missing, but which can help unveil how stability determines working life and safety issues of batteries. Therefore, these interfacial studies are required to be conducted in the future and can help achieve high safe, long cycling nitride-based all-solid-state lithium metal batteries.

5. All-solid-state lithium batteries with nitride solid-state electrolytes

As discussed, nitride SSEs display high stability towards lithium metal anodes and have been used as rational SSE layers to stabilize lithium metal in all-solid-state batteries, including all-solid-state thin-film lithium metal batteries, nitride SSEs acting as coating layers or interlayers, and all-solid-state lithium metal pouch cells.

Since the initial reports in 1992,[30,31] the deposited LiPON thin film enables the rapid development of all-solid-state thin-film lithium metal batteries, which power microelectronics and micro-/nano- electromechanical systems through forming the compact system-on-chip.[146,163] Fig. 14A shows a typical all-solid-state thin-film lithium metal batteries consisting of a sputtered LiPON SSE layer, a sputtered $LiNi_{0.5}Mn_{1.5}O_4$ cathode, a thermal-evaporation-deposited lithium metal anode and a sputtered Pt current collector.[17] Owing to forming stable LiPON–Li and LiPON–$LiNi_{0.5}Mn_{1.5}O_4$ interfaces as discussed in the interfacial stability section, this high-voltage all-solid-state thin-film lithium metal batteries delivered extremely long working life up to 10 000 cycles at 5.0C, much better than other liquid batteries (see Fig. 14B). In addition to this high-voltage cathode, LiPON has also been used for other cathode materials in all-solid-state thin-film lithium metal batteries, including V_2O_5,[31] $Li_{1.3}V_2O_5$,[164] $LiCoO_2$,[165–167] $LiMn_2O_4$,[168] $LiCr_{0.05}Ni_{0.45}Mn_{1.5}O_{4-\delta}$,[169] a Prussian blue $LiFeFe(CN)_6$,[170] and $Li_2Ag_{0.5}V_2O_5$.[171]

Furthermore, nitrides can also function as coating layers to stabilize lithium metal for other SSEs to overcome their remaining challenges (*e.g.* poor wetting of lithium on the SSEs' surfaces, serious interfacial reaction between SSEs and lithium metal), such as oxides,[173] sulfides,[161] and composite solid electrolytes.[162] The nitride coating layers include two types, nitride SSEs (*e.g.*, LiPON, Li_3N),[161,162,172–174] and non-Li-containing binary nitrides (*e.g.*, BN coating layers for $Li_{1.3}Al_{0.3}Ti_{1.7}(PO_4)_3$,[175] and Si_3N_4 coating layers for garnet $Li_7La_3Zr_2O_{12}$[176]). The latter coating with non-Li-containing binary nitrides is due to the lithiation mechanism of these nitrides and subsequent formation of corresponding lithium-containing nitrides during the initial cycles, which function as lithium-ion conductors and stabilization layers for lithium metal anodes. Moreover, the direct deposition of nitride SSEs on the surface of other SSEs is another promising method. As shown in Fig. 14C and D, the deposited LiPON coated on the surface of Li_6PS_5Cl SSE layers induces wetting of lithium metal on the surface and helps achieve intimate contact between SSE and lithium metal, which enhances lithium symmetric cell performance and increases the critical current density to 4.1 mA cm^{-2}.[161] Similar to this LiPON coating strategy, Li_3N coating layers were deposited on the surface garnet $Li_{6.5}La_3Zr_{1.5}Ta_{0.5}O_{12}$ (LLZT) SSEs and improved the wetting of lithium metal on SSEs and protect LLZT from lithium dendrite growth and further serious interfacial reaction with lithium metal (see Fig. 14E). This Li_3N-coating strategy leads to good cycling of all-solid-state lithium metal batteries at 40 °C (see Fig. 14F).

In addition to the utilization of nitride SSEs as ionic-conductive and electronic-insulating coating layers for lithium metal anodes, Wang *et al.*[66,177,178] recently introduced the concept of tuning ionic conductivity by incorporating SSEs, electronic conductivity by introducing carbon or metal, and lithiophobicity by using SSEs in interlayers to control lithium growth within the interlayer, thereby preventing further dendrite growth into SSE layers. As depicted in Fig. 15A–F, the high lithiophobicity of nitride SSEs, such as Li_7N_2I SSE, inhibits lithium growth into these nitride SSEs, whereas lithium tends to grow into lithiophilic interlayers along cracks or holes. Furthermore, Wang *et al.* identified a universal interlayer design for lithium metal: the Li nucleation region should be smaller than the Li growth region and the interlayer length. The Li nucleation region can be a mixed ionic and electronic conducting layer, achieved by mixing SSEs with electronically conductive carbon or metal. This design facilitates Li growth within the interlayer while confining it to the interlayer itself. Additionally, an extra lithiophobic interlayer, such as a pure nitride SSE layer, further stabilizes the grown Li beyond the nucleation region (Fig. 15G). Implementing this interlayer design significantly improved the cycling stability of all-solid-state lithium metal batteries, increasing the cycle life from just 5 cycles to 180 and 350 cycles (Fig. 15H).

In addition to the former two strategies employing nitrides, another promising option is to directly use nitride SSEs as lithium-ion conducting layers and separators with high toughness to suppress lithium dendrites in all-solid-state lithium metal batteries. Ji *et al.* (Li_3N/LiF),[18] Ma *et al.* (Li_7N_2I–LiOH)[67] and Li *et al.* ($Li_9N_2Cl_3$ and β-Li_3N)[15,16] recently report nitride SSEs coupled with sulfide and halide SSEs for all-solid-state lithium metal batteries. Furthermore, the latter studies achieve breakthroughs to suppress lithium dendrite growth at high current densities & high cycling capacity (7.5 mA cm^{-2} and 7.5 mA h cm^{-2}) with vacancy-rich β-Li_3N SSEs and achieve high

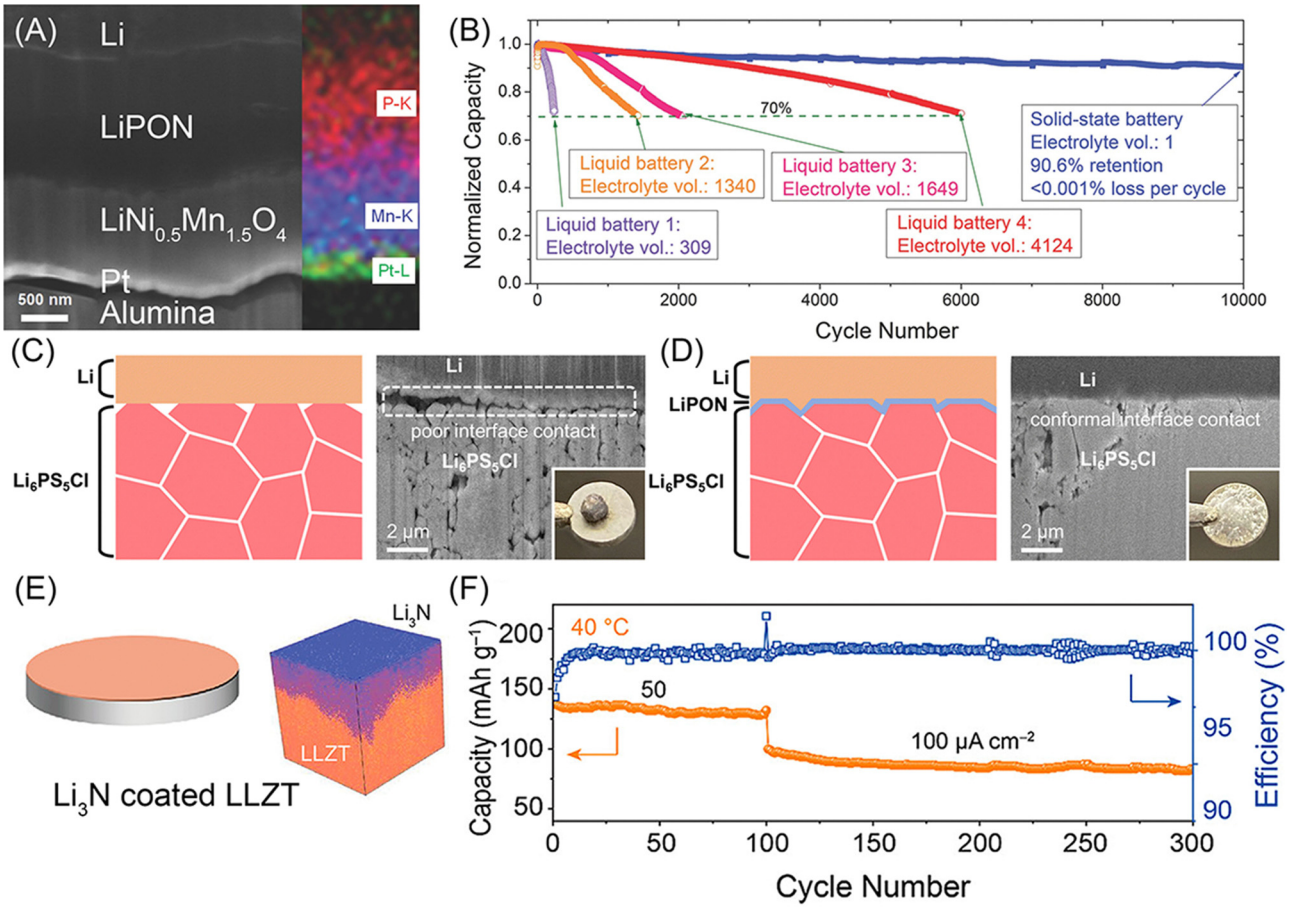

Fig. 14 (A) and (B) Li–LiPON–$LiNi_{0.5}Mn_{1.5}O_4$ solid-state battery: (A) SEM images and EDX mapping of the cross section of the solid-state battery after 1000 cycles and (B) capacity retention of this solid-state battery and other liquid lithium batteries cycled at 5C up to 10 000 cycles. Reproduced with permission,[17] Copyright © 2014 WILEY-VCH Verlag GmbH & Co. KGaA, Weinheim. (C) and (D) Schematic and SEM images of LiPON coated Li_6PS_5Cl for lithium metal and LiPON coating layers help achieve good contact between Li and Li_6PS_5Cl. Reproduced with permission,[161] Copyright © The Royal Society of Chemistry 2022. (E) and (F) Li_3N modified garnet SSE ($Li_{6.5}La_3Zr_{1.5}Ta_{0.5}O_{12}$, LLZT) for all-solid-state lithium metal batteries: (E) schematic and element distribution of N, Zr, and La in the time-of-flight secondary-ion mass spectroscopy of a Li_3N coated LLZT pellet (blue: N, red: La, orange: Zr), and (F) electrochemical performance of the all-solid-state Li/LN-LLZT/$LiFePO_4$ tested at 40 °C. Reproduced with permission,[172] Copyright © 2018, American Chemical Society.

areal capacity of >4.0 mA h cm^{-2} and fast charging & discharging up to 5.0C (see Fig. 16).[15] The excellent lithium symmetric cell performance originates from intrinsic stability towards lithium metal anodes and high room-temperature ionic conductivity of vacancy-rich β-Li_3N SSEs (see Fig. 3C–E and 16A–C). Then the cathode/halides/vacancy-rich β-Li_3N/Li all-solid-state lithium metal batteries delivery ultra-long cycling life up to 5000 cycles (5000 cycles for $LiCoO_2$, and 3500 cycles for NCM83), high cathode loading of up to 30.31 mg cm^{-2} (cathode: NCM83, initial reversible areal capacity: 4.47 mA h cm^{-2}) (see Fig. 16D and E). Employing solvent-free dry-film SSE techniques,[179] vacancy-rich β-Li_3N-based all-solid-state lithium metal pouch cells also achieve a high areal capacity of $\sim$1.97 mA h cm^{-2} (see Fig. 16F and G). The promising progress in nitride-based all-solid-state lithium metal batteries will be a key relief for generation 3 lithium metal batteries to achieve high energy density and to meet the demands of the fast-developing electric vehicle and grid energy storage markets.

Regarding the practical application of all-solid-state lithium metal batteries in EVs, pouch cells are a rational battery form for industrial manufacturing and are promising to achieve energy density targets of more than 350 W h kg^{-1} and up to 500 W h kg^{-1}.[4,185,186] We also evaluate the energy density of nitride-based all-solid-state lithium metal pouch cells using typical $LiNi_{0.8}Mn_{0.1}Co_{0.1}O_2$ (NMC811) cathodes and lithium metal anodes and also taking other inactive materials (*e.g.*, current collectors) into account (see Fig. 17). Typical halide (*i.e.*, Li_3InCl_6) and sulfide (*i.e.*, $Li_{10}GeP_2S_{12}$ (LGPS)) SSEs are used to be coupled with β-Li_3N nitride SSEs for the cathode sides based on the electrochemical stability windows of SSEs. Based on the calculation in the form of pouch cells, it is crucial to increase cathode areal capacities, reduce the areal capacity ratio of negative to positive electrodes (N/P ratio), and use light-weight Al & Cu current collectors to meet the requirement of energy density. Regarding 350 W h kg^{-1} as the critical energy density, the all-solid-state lithium metal batteries require a critical areal

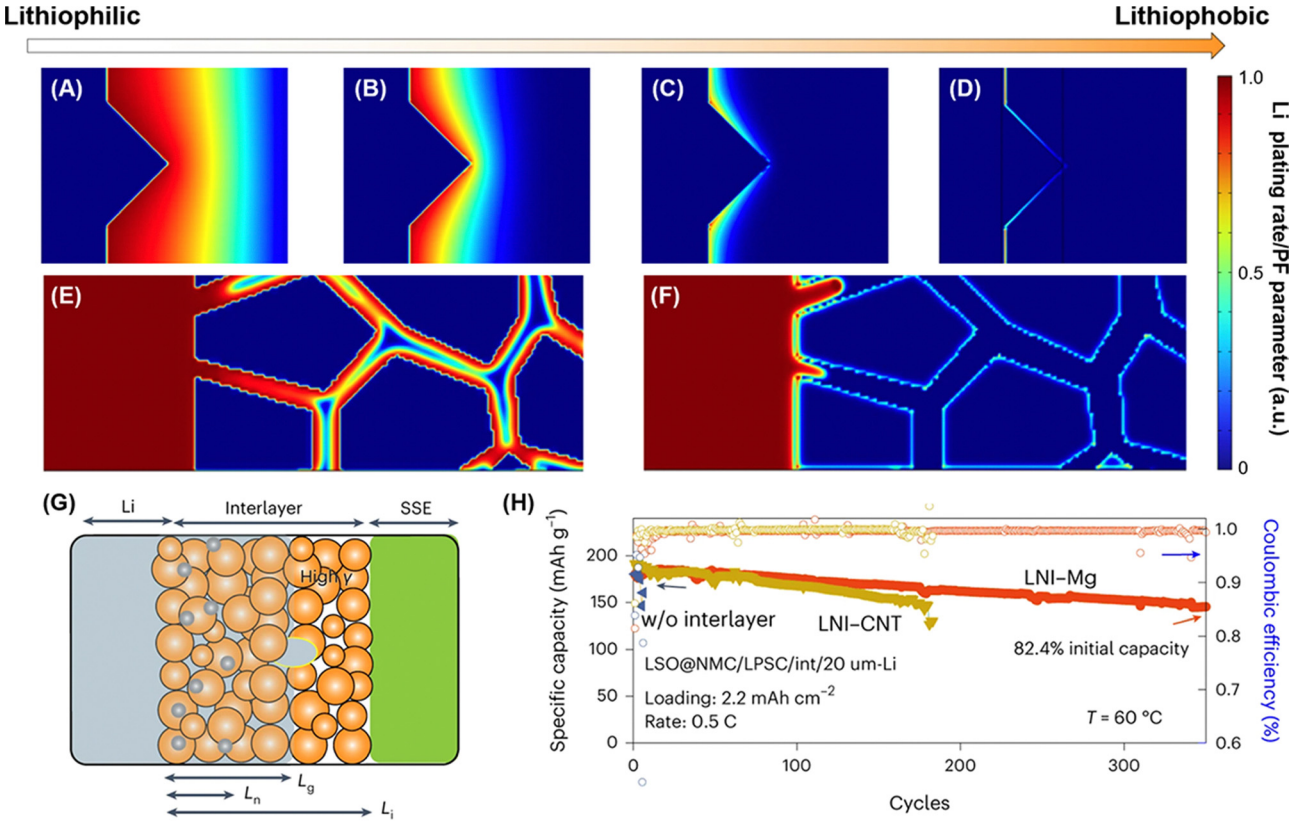

Fig. 15 (A)–(D) Spatial distribution of lithium nucleation in interlayers as a function of lithiophobicity, showing normalized Li growth and nucleation rates. Li growth behavior is illustrated for both lithiophilic interlayers (E) and lithiophobic interlayers (F). The color map represents the normalized Li nucleation rate or the phase field (PF) parameter, where a PF parameter of 1 indicates Li metal. (G) Schematics of mixed conductive interlayers, highlighting the Li nucleation length (L_n) being smaller than the growth length (L_g) and the interlayer length (L_i). Li plating beyond the nucleation region remains stable if the interlayer is lithiophobic (high γ). (H) Cycling performance of solid-state LSO@NMC811/LPSC/interlayer/20 μm-Li full cells (with interlayers: LNI–CNT or LNI–Mg) at a rate of 0.5C and an areal capacity of 2.2 mA h cm^{-2}. The LSO@NMC811/LPSC/20 μm-Li full cell without an interlayer (w/o) is used as a reference. LSO@NMC811: Li_4SiO_4-coated NMC811 cathode, LPSC: Li_6PS_5Cl SSE, LNI: Li_7N_2I SSE. Reproduced with permission,[66] Copyright © 2024, The Author(s), under exclusive licence to Springer Nature Limited.

capacity of 4 mA h cm^{-2} and a critical thickness of 100 μm for SSEs layers with an areal capacity of 10 mA h cm^{-2} and 20 μm for SSEs layers with an areal capacity of 4 mA h cm^{-2}. Regarding the N/P ration, the critical value is 10 for an areal capacity of 4 mA h cm^{-2} and 1.2 for an areal capacity of 4 mA h cm^{-2}. In the case of Al & Cu current collectors, light weight foils (8 μm Al, and 4 μm Cu) can help compromise the requirement of critical areal capacities to 2 mA h cm^{-2} for 10 μm SSEs and 3 mA h cm^{-2} for 20 μm SSEs and critical thickness of 80 μm for SSEs with an areal capacity of 7 mA h cm^{-2} and 40 μm for SSEs with an areal capacity of 4 mA h cm^{-2}. The current design of all-solid-state batteries with low areal capacities (1–2.5 mA h cm^{-2}), thick SSE layers (1000 μm), Li–In alloy or thick Li metal anodes (N/P: 20–200) requires revolution and innovation of cell configurations.[187]

Conclusions and perspectives

In this review, we review the research and development of nitride SSEs for all-solid-state lithium metal batteries. Firstly, the progress of all-solid-state lithium metal batteries are summarized with the promise of high energy density and remaining challenges of lithium metal–SSE interfaces. Then nitride SSEs are introduced as promising SSE candidates to stabilize lithium metal anodes and the development history of nitrides SSEs is highlighted with several milestones. For recently developed nitride SSEs, several types of nitrides have been categorized according to their compositions and crystal & local structures. Additionally, the synthesis strategies of nitride SSEs are detailed, including the Czochralski single crystal growth method, solid-state reaction and phase transformation methods, and the physical and chemical vapor deposition methods. It should be highlighted that vapor deposition methods have been widely conducted for thin-film batteries and the high-energy ball-milling method is suitable for mass production. Furthermore, some deep insights have been achieved in the lithium-ion diffusion behaviors and mechanisms of these nitrides according to compositions, crystal & local structures, and fabrication methods through a synergy between experimental and simulation results. It has been clearly demonstrated that the chemical and electrochemical stability (*i.e.*, thermal stability, air stability, and interfacial stability) is crucial

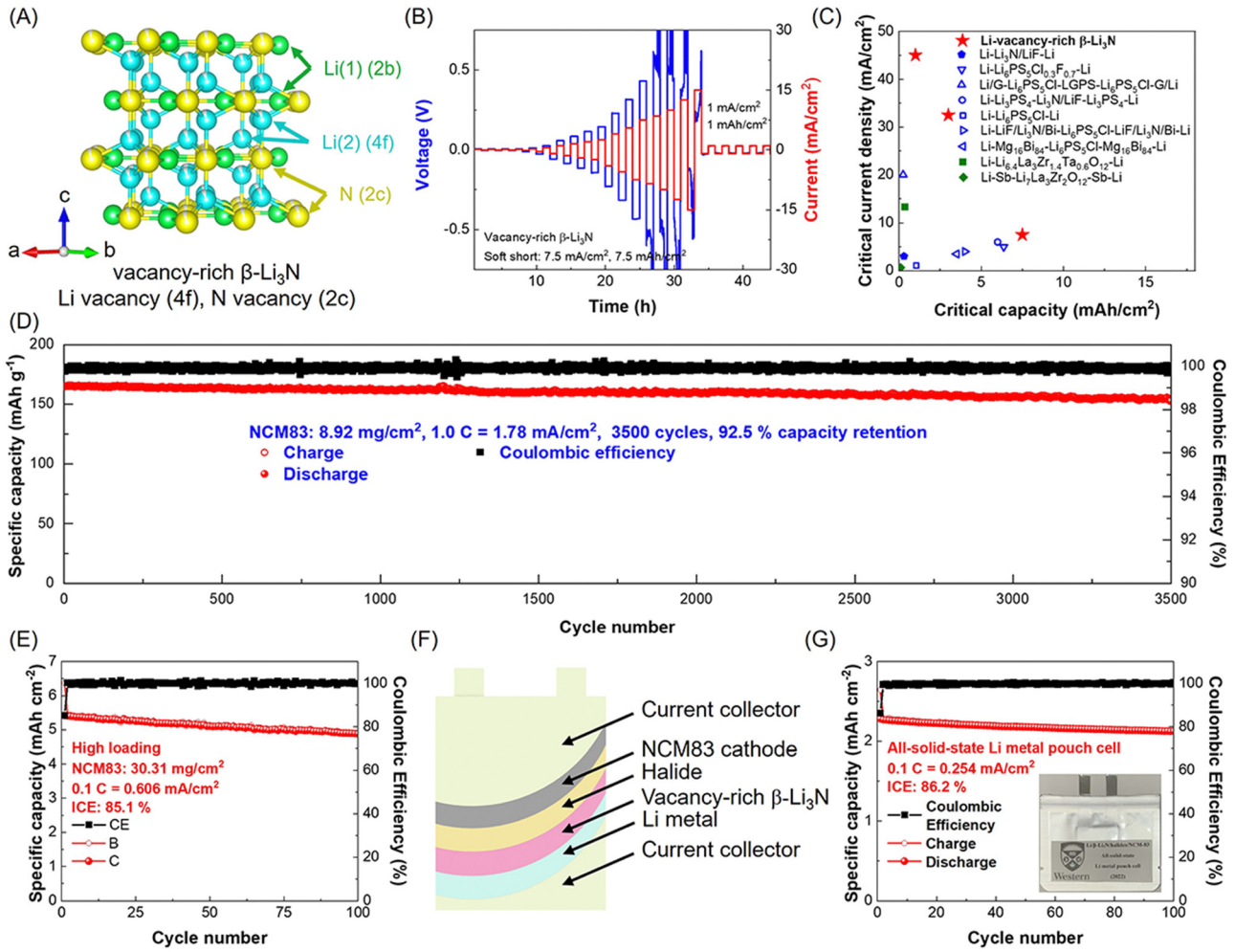

Fig. 16 Vacancy-rich β-Li_3N SSE for all-solid-state lithium metal batteries: (A) crystal structures of vacancy-rich β-Li_3N. (B) Voltage profiles of Li-vacancy-rich β-Li_3N–Li symmetric all-solid-state cell with incremental current densities and capacities (lithium plating/stripping for fixed 1 h). (C) Comparison of the critical current densities and capacity for lithium symmetric cells using sulfide-, oxide-, and nitride-based SSEs: Li-vacancy-rich β-Li_3N–Li, $Li_6PS_5Cl_{0.3}F_{0.7}$,[180] G–Li_6PS_5Cl–LGPS–Li_6PS_5Cl–G,[181] Li_3PS_4–Li_3N/LiF–Li_3PS_4,[18] Li_3N/LiF,[18] Li_6PS_5Cl,[182] $Li_{6.4}La_3Zr_{1.4}Ta_{0.6}O_{12}$,[183] and Sb–$Li_7La_3Zr_2O_{12}$–Sb.[184] (D)–(G) Long-term electrochemical performance of the NCM83/halides/vacancy-rich β-Li_3N/Li all-solid-state lithium metal batteries at 25 °C: (D) charge–discharge capacity and the Coulombic efficiency as a function of cycle number for all-solid-state lithium metal batteries cycled at 1.0C the NCM83 loading of 8.92 mg cm^{-2}. (E) Charge–discharge capacity and Coulombic efficiency as a function of cycle number of high loading all-solid-state lithium metal batteries performance (areal loading of NMC83: 30.31 mg cm^{-2}, initial reversible areal capacity: 5.42 mA h cm^{-2}). (F) Schematic of and (G) charge–discharge capacity and Coulombic efficiency as a function of cycle number of an all-solid-state pouch cell with a high areal capacity (initial reversible areal capacity: 2.28 mA h cm^{-2}). Reproduced with permission,[15] Copyright © 2024, Springer Nature Limited.

to practical all-solid-state lithium metal batteries applications and manufacturing. We also provide a detailed review of the application of nitride SSEs in all-solid-state lithium metal batteries, including thin film LiPON and derivative SSEs used for thin-film batteries, and nitride thin coating layers and SSEs coupled with other SSEs for laboratory-research small cells and pouch cells. As highlighted, all-solid-state lithium metal pouch cells are technically considered a rational form for electric vehicles. It is clear that the practical pouch cell design meeting requirements of high energy densities (350–500 W h kg^{-1}) needs to adopt thin SSE layers, (<100 μm), low N/P ratios, (<10), and high areal capacity loading, (>3 mA h cm^{-2}). Reducing thickness of current collectors (8 μm Al foils, and 4 μm Cu foils) helps achieve the energy density objectives with less limitations.

Although some remarkable progress has been made on the nitride SSEs for all-solid-state lithium metal batteries, the achievement of its promise of high energy densities in the cell level requires great advances. Here, we outline several remaining crucial challenges and future research directions for nitride SSEs, which may lead to the pathways for practical applications.

(a) Materials discovery and preparation methods

Continuing efforts must be made on exploring new nitrides compositions and structures to achieve fast lithium-ion diffusion, good air stability, and excellent interfacial stability. Firstly, higher ionic conductivity is always an ultimate target for SSEs. Additionally, to meet requirements of fast charging targets of all-solid-state lithium metal batteries (*i.e.*, 15 min or less charge time), the ionic conductivity of nitride SSEs should

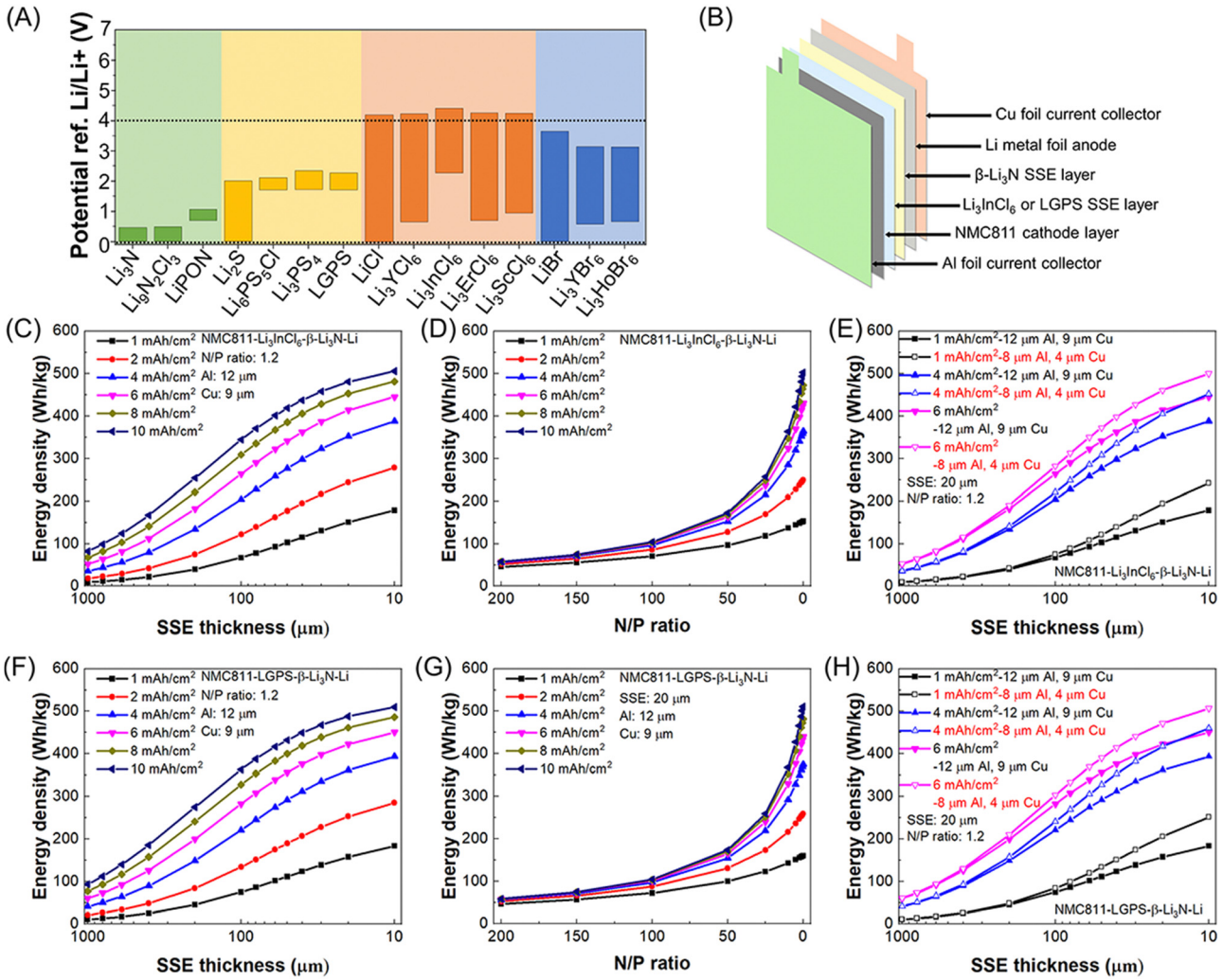

Fig. 17 (A) Thermodynamic intrinsic electrochemical windows of various nitrides (Li_3N, $Li_9N_2Cl_3$, LiPON), sulfides (Li_2S, Li_6PS_5Cl, Li_3PS_4, and $Li_{12}GeP_2S_{12}$ (LGPS)), and halides (LiCl, Li_3YCl_6, Li_3InCl_6, Li_3ErCl_6, Li_3ScCl_6, LiBr, Li_3YBr_6, and Li_3HoBr_6) SSEs, calculated for comparative assessment. Reproduced with permission,[16,155,188,189] Copyright © 2015 American Chemical Society, and Copyright © 2019 Wiley-VCH Verlag GmbH & Co. KGaA, Weinheim. (B) Schematic of an all-solid-state pouch cell Al/NMC811/Li_3InCl_6 or LGPS/β-Li_3N/Li/Cu. Energy density evaluation of all-solid-state lithium metal pouch cells. Gravimetric energy densities of all-solid-state lithium metal batteries with the configuration of (C)–(E) Al–NMC811–Li_3InCl_6–β-Li_3N–Li–Cu and (F)–(H) Al–NMC811–LGPS–β-Li_3N–Li–Cu, where the weight of Al and Cu current collectors are considered into the calculation of energy density. Gravimetric energy densities as a function of (C) and (F) SSE thickness, (D) and (G) N/P ratio, and (E) and (H) SSE thickness with lighter-weight Al and Cu foils. (NMC811, capacity: 200 mA h g^{-1}, nominal voltage: 3.75 V, weight percentage: 90 wt% mixed with SSEs (10 wt%); lithium metal: capacity: 3500 mA h g^{-1}; Li_3InCl_6, density: 2.59 g cm^{-3}; LGPS, density: 2.04 g cm^{-3}; Li_3N, density: 1.27 g cm^{-3}; Al foil, density: 2.7 g cm^{-3}; Cu foil, density: 8.9 g cm^{-3}.

reach 10^{-3} S cm^{-1} and up to 10^{-2} S cm^{-1}. Furthermore, the current battery manufacturing industry will process nitride in dry rooms (dew point: < -40 °C) and even store nitrides in ambient air environment, which demands of good stability of nitrides in dry rooms or further in ambient air (*e.g.*, no chemical reaction of nitrides or remaining >80% room-temperature ionic conductivity after long-term storage in these types of environments for weeks and even months). With regard to interfacial stability in full cells, nitride SSEs should be compatible with lithium metal anodes and cathodes. The target regarding the stability of nitrides towards lithium metal needs to meet these demands of high areal capacity (>3 mA h cm^{-2}) for high energy density in the cell level (350 W h kg^{-1} and up to 500 W h kg^{-1}) and fast charging (>4C) for short charge time (<15 min). It suggests that promising nitride SSEs can prevent serious interfacial reactions and dendrite growth at high critical current densities (>12 mA h cm^{-2}) and high critical stripping/plating capacities (>3 mA h cm^{-2}). Regarding cathodes, nitride SSEs are required to be either compatible with cathodes (*i.e.*, electrochemical window extended to >4.0 V or nitride–cathode interfaces remained stable at >4.0 V) or stable towards other cathode-compatible SSEs (*e.g.*, oxides, halides, and sulfides). The accomplishment of these multiple targets for nitrides materials needs several strategies. As modifying known materials works in other SSEs, we should explore doping, tuning crystal structures (*e.g.*, vacancy population), and local disorders (*e.g.*, amorphization), and surface engineering to overcome these challenges. Additionally, high-throughput computational methods together

with experimental synthesis can help discover new nitride SSE materials with designated characteristics.[13,190–192]

While several preparation strategies have been reported for nitride SSEs, it is crucial to develop other methods to meet demands for practically accessible all-solid-state lithium metal batteries, including mass production, low cost, the elimination of waste (*e.g.*, gas, liquid, and solid wastes) and the accommodation to various application situations (*e.g.*, SSE layers, and coating layers). As highlighted, solid-state reaction strategies with high-energy ball-milling and sintering can meet industrial manufacturing demands. Other strategies can be considered as promising solutions, such as solution-based methods,[193–195] deposition methods,[172,196] and surface ammonification methods.[197,198] Since the energy density of all-solid-state lithium metal batteries is partially decided by the thickness of SSE layers, these strategies help prepare thin-film SSE layers and reach high-energy-density targets.

(b) Fundamental understanding

In addition to materials, there will be increasing research interest in fundamental understanding of lithium-ion diffusion mechanisms in nitrides, mechanical properties of nitrides, air stability and interfacial stability (*i.e.*, nitride SSE–Li metal anode, -cathode, and -other SSE interfacial stability. In the case of lithium-ion diffusion mechanisms in nitrides, incorporation with N, distortion of polyanions and vacancy-driven low hopping energy & high mobile Li-ion population have been reported to be main reasons resulting in fast lithium-ion diffusion.[15,43,44] More research efforts can be made on greater understanding of the relevance between lithium-ion diffusion mechanism and other issues, including compositions, local ion coordination structures, anion frameworks, and grain boundaries. Crucial for the understanding will be advanced structural characterizations of average crystal structures and local structure (*e.g.* X-ray and neutron powder diffraction, pair distribution function, and X-ray absorption fine structure) and simulations of lithium-ion diffusion.

Mechanical properties, including elastic moduli (Young's modulus (E), shear modulus (G), and bulk modulus (K)), hardness, modulus-to-hardness ratio (E/H), Poisson's ratio, and fracture toughness (K_C), play critical roles in influencing cell fabrication, operation, and cycling stability in all-solid-state lithium metal batteries.[199–201] These properties directly impact factors such as fabrication and stack pressures, as well as failure mechanisms like lithium dendrite growth and plating-induced cracking in SSEs.[202,203] For instance, LiPON with an E/H ratio of approximately 23, exhibits significantly higher ductility compared to typical oxide glasses (E/H = 10–13). This enhanced ductility allows LiPON to densify and undergo shear deformation under stress, effectively reducing stress intensity and contributing to its exceptional mechanical robustness, fracture resistance, and reliable performance in thin-film solid-state batteries.[204–207] Nonetheless, further characterization and in-depth investigations of mechanical properties of nitrides, are necessary to better understand failure mechanisms and establish design guidelines for parameters such as stack pressure and mechanical loading tolerances.

For air stability, Li *et al.*[15,16] reported forming protection surface on β-Li_3N and $Li_9N_2Cl_3$ and these two nitride SSEs possess good air stability in dry room and ambient air. The exploration of other nitrides and mechanisms with regard to air stability will need novel experimental design to detect evolution of nitrides in structures and possible formation of gas (preferably *in situ* and *operando* approaches). Furthermore, interfacial stability is a determining factor in the electrochemical performance of all-solid-state lithium metal batteries, including three main types of interfaces, nitride–lithium metal interfaces, nitride–cathode interfaces, and nitride-other SSE interfaces. For these interfaces, interfacial reactions, interfacial evolution together with volume change, forming voids and dendrite growth need to be clarified through advanced characterizations, such as X-ray absorption fine structure, electron energy loss spectroscopy, and X-ray computed tomography.

(c) Materials processing, batteries manufacturing and operation

Regarding all-solid-state lithium metal pouch cells as the feasible form providing high energy density in the cell level, rational fabrication strategies of thin nitride SSE films should be developed. As a time- & cost- efficient strategy, the dry-film method using polytetrafluoroethylene (PTFE) binder has been used to prepare β-Li_3N SSE thin films.[15,185] More optional binders should be tested and the mechanical properties can be further optimized to fit the industrial batteries manufacturing processes. Additionally, to further increase energy density, other optional optimization designs of cell configurations are required, including anode free cells, stacking strategies, and thin current collectors. Furthermore, recently developed all-solid-state lithium metal batteries need significant amounts of stack pressure to enable good operation states. The stack pressure value required for nitride-based lithium metal batteries should be clarified. And the target of operation of all-solid-state lithium metal pouch cells should be to lower and even eliminate the use of external pressing modules.

Overall, the emerging nitride SSEs provide promising opportunities to overcome remaining SSE–Li metal interfacial issues and fulfil all-solid-state lithium metal batteries promise of high energy density. The future advance of nitride SSEs in these challenging directions can bring pathways for practical all-solid-state lithium metal batteries for electric vehicles.

Data availability

This review does not involve new primary research, software, or code. As no new data were generated or analyzed, data availability is not applicable.

Conflicts of interest

The authors declare no competing interests.

Acknowledgements

This work was funded by the Eastern Institute of Technology (EIT), Ningbo, the Ningbo University of Technology, the Natural Sciences and Engineering Research Council of Canada (NSERC), the Canada Research Chair Program, the Canada Foundation for Innovation (CFI), the Ontario Research Fund, the Canada Light Source (CLS) at the University of Saskatchewan, the University of Western Ontario. CLS was supported by CFI, NSERC, NRC, CHIR, and the University of Saskatchewan. Weihan Li, Minsi Li, and Haoqi Ren acknowledge the receipt of support from the CLSI Graduate and Post-Doctoral Student Travel Support Program. Weihan Li appreciates the funding support from Mitacs Accelerate Fellowships.

References

1 A. Yoshino, The birth of the lithium-ion battery, *Angew. Chem., Int. Ed.*, 2012, **51**(24), 5798–5800.
2 X. Zeng, M. Li, D. Abd El-Hady, W. Alshitari, A. S. Al-Bogami and J. Lu, *et al.*, Commercialization of lithium battery technologies for electric vehicles, *Adv. Energy Mater.*, 2019, **9**(27), 1900161.
3 Y. Huang and J. Li, Key Challenges for Grid-Scale Lithium-Ion Battery Energy Storage, *Adv. Energy Mater.*, 2022, 2202197.
4 J. Liu, Z. Bao, Y. Cui, E. J. Dufek, J. B. Goodenough and P. Khalifah, *et al.*, Pathways for practical high-energy long-cycling lithium metal batteries, *Nat. Energy*, 2019, **4**(3), 180–186.
5 X. Feng, D. Ren, X. He and M. Ouyang, Mitigating thermal runaway of lithium-ion batteries, *Joule*, 2020, **4**(4), 743–770.
6 A. Banerjee, X. Wang, C. Fang, E. A. Wu and Y. S. Meng, Interfaces and interphases in all-solid-state batteries with inorganic solid electrolytes, *Chem. Rev.*, 2020, **120**(14), 6878–6933.
7 Y. Pang, J. Pan, J. Yang, S. Zheng and C. Wang, Electrolyte/electrode interfaces in all-solid-state lithium batteries: a review, *Electrochem. Energy Rev.*, 2021, **4**(2), 169–193.
8 X.-B. Cheng, C.-Z. Zhao, Y.-X. Yao, H. Liu and Q. Zhang, Recent advances in energy chemistry between solid-state electrolyte and safe lithium–metal anodes, *Chem*, 2019, **5**(1), 74–96.
9 X. Chen, C. Qin, F. Chu, F. Li, J. Liu and F. Wu, Contriving a gel polymer electrolyte to drive quasi-solid-state high-voltage Li metal batteries at ultralow temperatures, *Energy Environ. Sci.*, 2025, **18**, 910–922.
10 D. Luo, L. Zheng, Z. Zhang, M. Li, Z. Chen and R. Cui, *et al.*, Constructing multifunctional solid electrolyte interface *via in situ* polymerization for dendrite-free and low N/P ratio lithium metal batteries, *Nat. Commun.*, 2021, **12**(1), 186.
11 M. Mao, X. Ji, Q. Wang, Z. Lin, M. Li and T. Liu, *et al.*, Anion-enrichment interface enables high-voltage anode-free lithium metal batteries, *Nat. Commun.*, 2023, **14**(1), 1082.
12 Y.-C. Yin, J.-T. Yang, J.-D. Luo, G.-X. Lu, Z. Huang and J.-P. Wang, *et al.*, A LaCl3-based lithium superionic conductor compatible with lithium metal, *Nature*, 2023, **616**(7955), 77–83.
13 Y. Zhu, X. He and Y. Mo, Strategies based on nitride materials chemistry to stabilize Li metal anode. Advanced, *Science*, 2017, **4**(8), 1600517.
14 H. Kwak, S. Wang, J. Park, Y. Liu, K. T. Kim and Y. Choi, *et al.*, Emerging Halide Superionic Conductors for All-Solid-State Batteries: Design, Synthesis, and Practical Applications, *ACS Energy Lett.*, 2022, **7**(5), 1776–1805.
15 W. Li, M. Li, S. Wang, P.-H. Chien, J. Luo and J. Fu, *et al.*, Superionic conducting vacancy-rich β-Li_3N electrolyte for stable cycling of all-solid-state lithium metal batteries, *Nat. Nanotechnol.*, 2024, **20**, 265–275.
16 W. Li, M. Li, P.-H. Chien, S. Wang, C. Yu and G. King, *et al.*, Lithium-compatible and air-stable vacancy-rich Li9N2Cl3 for high–areal capacity, long-cycling all–solid-state lithium metal batteries, *Sci. Adv.*, 2023, **9**, eadh4626.
17 J. Li, C. Ma, M. Chi, C. Liang and N. J. Dudney, Solid electrolyte: the key for high-voltage lithium batteries, *Adv. Energy Mater.*, 2015, **5**(4), 1401408.
18 X. Ji, S. Hou, P. Wang, X. He, N. Piao and J. Chen, *et al.*, Solid-State Electrolyte Design for Lithium Dendrite Suppression, *Adv. Mater.*, 2020, **32**(46), 2002741.
19 E. Zintl and G. Brauer, Konstitution des Lithiumnitrids, *Z. Elektrochem. Angew. Phys. Chem.*, 1935, **41**(2), 102–107.
20 B. Boukamp and R. Huggins, Fast ionic conductivity in lithium nitride, *Mater. Res. Bull.*, 1978, **13**(1), 23–32.
21 A. Rabenau and H. Schulz, Re-evaluation of the lithium nitride structure, *J. Less-Common Met.*, 1976, **50**(1), 155–159.
22 B. Boukamp and R. Huggins, Lithium ion conductivity in lithium nitride, *Phys. Lett. A*, 1976, **58**(4), 231–233.
23 F. Gallais and E. Masdupuy, Chimie physique-sur la constitution du nitrure de lithium et lexistenee de lion N3, *C. R. Seances Acad. Sci.*, 1948, **227**(13), 635–637.
24 A. Huq, J. W. Richardson, E. R. Maxey, D. Chandra and W.-M. Chien, Structural studies of Li_3N using neutron powder diffraction, *J. Alloys Compd.*, 2007, **436**(1–2), 256–260.
25 T. Lapp, S. Skaarup and A. Hooper, Ionic conductivity of pure and doped Li_3N, *Solid State Ionics*, 1983, **11**(2), 97–103.
26 U. V. Alpen, A. Rabenau and G. Talat, Ionic conductivity in Li_3N single crystals, *Appl. Phys. Lett.*, 1977, **30**(12), 621–623.
27 U. Alpen, M. Bell and T. Gladden, Lithium ion conduction in lithium nitride single crystals and sinters, *Electrochim. Acta*, 1979, **24**(7), 741–744.
28 W. Li, G. Wu, C. M. Araújo, R. H. Scheicher, A. Blomqvist and R. Ahuja, *et al.*, Li+ ion conductivity and diffusion mechanism in α-Li_3N and β-Li_3N, *Energy Environ. Sci.*, 2010, **3**(10), 1524–1530.
29 E. Schönherr, G. Müller and E. Winckler, Czochralski growth of Li_3N crystals, *J. Cryst. Growth*, 1978, **43**(4), 469–472.
30 J. Bates, N. Dudney, G. Gruzalski, R. Zuhr, A. Choudhury and C. Luck, *et al.*, Electrical properties of amorphous lithium electrolyte thin films, *Solid State Ionics*, 1992, **53**, 647–654.
31 J. Bates, N. Dudney, G. Gruzalski, R. Zuhr, A. Choudhury and C. Luck, *et al.*, Fabrication and characterization of

amorphous lithium electrolyte thin films and rechargeable thin-film batteries, *J. Power Sources*, 1993, **43**(1–3), 103–110.

32 T. Famprikis, J. Galipaud, O. Clemens, B. Pecquenard and F. Le Cras, Composition dependence of ionic conductivity in LiSiPO (N) thin-film electrolytes for solid-state batteries, *ACS Appl. Energy Mater.*, 2019, **2**(7), 4782–4791.

33 S.-J. Lee, J.-H. Bae, H.-W. Lee, H.-K. Baik and S.-M. Lee, Electrical conductivity in Li–Si–P–O–N oxynitride thin-films, *J. Power Sources*, 2003, **123**(1), 61–64.

34 F. Wu, Y. Zheng, L. Li, G. Tan, R. Chen and S. Chen, Novel Micronano Thin Film Based on Li–B–P–O Target Incorporating Nitrogen as Electrolyte: How Does Local Structure Influence Chemical and Electrochemical Performances?, *J. Phys. Chem. C*, 2013, **117**(38), 19280–19287.

35 F. Michel, F. Kuhl, M. Becker, J. Janek and A. Polity, Electrochemical and Optical Properties of Lithium Ion Conducting LiPSON Solid Electrolyte Films, *Phys. Status Solidi B*, 2019, **256**(10), 1900047.

36 Z. Luo, A. Lu, T. Liu, J. Song and G. Han, La2O3 substitution in Li-Al-PON glasses for potential solid electrolytes applications, *Solid State Ionics*, 2016, **295**, 104–110.

37 H. Schulz and K. Thiemann, Defect structure of the ionic conductor lithium nitride (Li_3N), *Acta Crystallogr., Sect. A*, 1979, **35**(2), 309–314.

38 U. Alpen, Li_3N: A promising Li ionic conductor, *J. Solid State Chem.*, 1979, **29**(3), 379–392.

39 N. Tapia-Ruiz, A. G. Gordon, C. M. Jewell, H. K. Edwards, C. W. Dunnill and J. M. Blackman, *et al.*, Low dimensional nanostructures of fast ion conducting lithium nitride, *Nat. Commun.*, 2020, **11**(1), 1–8.

40 H. J. Beister, S. Haag, R. Kniep, K. Strössner and K. Syassen, Phase transformations of lithium nitride under pressure, *Angew. Chem., Int. Ed. Engl.*, 1988, **27**(8), 1101–1103.

41 M. Mali, J. Roos and D. Brinkmann, Nuclear-magnetic-resonance evidence for a new phase induced by pressure in the superionic conductor Li_3N, *Phys. Rev. B:Condens. Matter Mater. Phys.*, 1987, **36**(7), 3888.

42 A. Lazicki, B. Maddox, W. Evans, C.-S. Yoo, A. McMahan and W. Pickett, *et al.*, New cubic phase of Li_3N: Stability of the N^{3-} ion to 200 GPa, *Phys. Rev. Lett.*, 2005, **95**(16), 165503.

43 V. Lacivita, N. Artrith and G. Ceder, Structural and compositional factors that control the li-ion conductivity in LiPON electrolytes, *Chem. Mater.*, 2018, **30**(20), 7077–7090.

44 V. Lacivita, A. S. Westover, A. Kercher, N. D. Phillip, G. Yang and G. Veith, *et al.*, Resolving the amorphous structure of lithium phosphorus oxynitride (Lipon), *J. Am. Chem. Soc.*, 2018, **140**(35), 11029–11038.

45 M. A. Marple, T. A. Wynn, D. Cheng, R. Shimizu, H. E. Mason and Y. S. Meng, Local structure of glassy lithium phosphorus oxynitride thin films: a combined experimental and ab initio approach, *Angew. Chem., Int. Ed.*, 2020, **59**(49), 22185–22193.

46 N.-S. Roh, S.-D. Lee and H.-S. Kwon, Effects of deposition condition on the ionic conductivity and structure of amorphous lithium phosphorus oxynitrate thin film, *Scr. Mater.*, 1999, **42**(1), 43–49.

47 B. Fleutot, B. Pecquenard, H. Martinez, M. Letellier and A. Levasseur, Investigation of the local structure of LiPON thin films to better understand the role of nitrogen on their performance, *Solid State Ionics*, 2011, **186**(1), 29–36.

48 C. Solano, M. Dussauze, P. Vinatier, L. Croguennec, E. I. Kamitsos and R. Hausbrand, *et al.*, Phosphate structure and lithium environments in lithium phosphorus oxynitride amorphous thin films, *Ionics*, 2016, **22**(4), 471–481.

49 F. Muñoz, A. Durán, L. Pascual, L. Montagne, B. Revel and A. C. M. Rodrigues, Increased electrical conductivity of LiPON glasses produced by ammonolysis, *Solid State Ionics*, 2008, **179**(15–16), 574–579.

50 B. Fleutot, B. Pecquenard, H. Martinez and A. Levasseur, Thorough study of the local structure of LiPON thin films to better understand the influence of a solder-reflow type thermal treatment on their performances, *Solid State Ionics*, 2012, **206**, 72–77.

51 N. Mascaraque, J. L. G. Fierro, A. Durán and F. Muñoz, An interpretation for the increase of ionic conductivity by nitrogen incorporation in LiPON oxynitride glasses, *Solid State Ionics*, 2013, **233**, 73–79.

52 P. D. Mani, S. Saraf, V. Singh, M. Real-Robert, A. Vijayakumar and S. J. Duranceau, *et al.*, Ionic conductivity of bias sputtered lithium phosphorus oxy-nitride thin films, *Solid State Ionics*, 2016, **287**, 48–59.

53 J. D. LaCoste, A. Zakutayev and L. Fei, A review on lithium phosphorus oxynitride, *J. Phys. Chem. C*, 2021, **125**(7), 3651–3667.

54 X. Yu, J. Bates, G. Jellison and F. Hart, A stable thin-film lithium electrolyte: lithium phosphorus oxynitride, *J. Electrochem. Soc.*, 1997, **144**(2), 524.

55 N. J. Dudney, Solid-state thin-film rechargeable batteries, *Mater. Sci. Eng., B*, 2005, **116**(3), 245–249.

56 H. Sattlegger and H. Hahn, Über das System Li_3N/LiCl, *Z. Anorg. Allg. Chem.*, 1971, **379**(3), 293–299.

57 H. Sattlegger and H. Hahn, Über Versuche zur Umsetzung von Li_3N mit Lithiumhalogeniden, *Naturwissenschaften*, 1964, **51**(22), 534–535.

58 P. Hartwig, W. Weppner and W. Wichelhaus, Fast ionic lithium conduction in solid lithium nitride chloride, *Mater. Res. Bull.*, 1979, **14**(4), 493–498.

59 P. Hartwig, W. Weppner, W. Wichelhaus and A. Rabenau, Lithium Nitride Halides—New Solid Electrolytes with High Li+ Ion Conductivity, *Angew. Chem., Int. Ed. Engl.*, 1980, **19**(1), 74–75.

60 P. Hartwig, A. Rabenau and W. Weppner, Phase equilibria and thermodynamic properties of the Li-N-Cl, Li-N-Br and Li-NI systems, *J. Less-Common Met.*, 1981, **80**(1), 81–90.

61 H. Obayashi, A. Gotoh and R. Nagai, Composition dependence of lithium ionic conductivity in lithium nitride-lithium iodide system, *Mater. Res. Bull.*, 1981, **16**(5), 581–585.

62 R. Marx and H.-M. Mayer, Preparation and crystal structure of ordered and disordered lithium nitride dichloride, Li5NCl2, *J. Solid State Chem.*, 1997, **130**(1), 90–96.

63 R. Marx, Preparation and crystal structure of lithium nitride chloride Li4NCl, *J. Solid State Chem.*, 1997, **128**(2), 241–246.
64 P. Hartwig, W. Weppner, W. Wichelhaus and A. Rabenau, Ionic transport in the lithium nitride bromides, Li6NBr3 and Li1 3N4Br, *Solid State Commun.*, 1979, **30**(10), 601–603.
65 H. Obayashi, R. Nagai, A. Gotoh, S. Mochizuki and T. Kudo, New fast lithium ionic conductor in the Li_3N LiI LiOH system, *Mater. Res. Bull.*, 1981, **16**(5), 587–590.
66 Z. Wang, J. Xia, X. Ji, Y. Liu, J. Zhang and X. He, *et al.*, Lithium anode interlayer design for all-solid-state lithium–metal batteries, *Nat. Energy*, 2024, 1–12.
67 B. Ma, R. Li, H. Zhu, T. Zhou, L. Lv and H. Zhang, *et al.*, Stable Oxyhalide-Nitride Fast Ionic Conductors for all-Solid-State Li Metal Batteries, *Adv. Mater.*, 2024, 2402324.
68 R. Marx, Reindarstellung und Kristallstruktur von Lithiumtrinitridbromid, Li10N3Br/Preparation and Crystal Structure of Lithium Trinitride Bromide Li10N3Br, *Z. Naturforsch. B*, 1995, **50**(7), 1061–1066.
69 R. Marx and H. M. Mayer, Reindarstellung und Kristallstruktur von Lithiumnitriddibromid, Li5NBr2/Preparation and Crystal Structure of Lithium Nitride Dibromide, Li5NBr2, *Z. Naturforsch. B*, 1995, **50**(9), 1353–1358.
70 R. Marx, Time-of-flight neutron diffraction study on lithium dinitride iodide, Li_7N_2I, *Eur. J. Solid State Inorg. Chem.*, 1998, **35**(3), 197–209.
71 L. J. Miara, N. Suzuki, W. D. Richards, Y. Wang, J. C. Kim and G. Ceder, Li-ion conductivity in Li 9 S 3 N, *J. Mater. Chem. A*, 2015, **3**(40), 20338–20344.
72 P. Yu, H. Zhang, F. Hussain, J. Luo, W. Tang and J. Lei, *et al.*, Lithium Metal-Compatible Antifluorite Electrolytes for Solid-State Batteries, *J. Am. Chem. Soc.*, 2024, **146**, 12681–12690.
73 D. Bräunling, O. Pecher, D. M. Trots, A. Senyshyn, D. A. Zherebtsov and F. Haarmann, *et al.*, Synthesis, crystal structure and lithium motion of Li8SeN2 and Li8TeN2, *Z. Anorg. Allg. Chem.*, 2010, **636**(6), 897–1153.
74 R. Marx, F. Lissner and T. Schleid, Li9NS3: Das erste Nitridsulfid der Alkalimetalle in einer Li2O-Typ-Variante, *Z. Anorg. Allg. Chem.*, 2006, **632**(12–13), 2151.
75 W. Schnick and J. Luecke, Lithium ion conductivity of LiPN2 and Li7PN4, *Solid State Ionics*, 1990, **38**(3–4), 271–273.
76 E. M. Bertschler, C. Dietrich, J. Janek and W. Schnick, Li18P6N16—a lithium nitridophosphate with unprecedented tricyclic [P6N16] 18− Ions, *Chem. – Eur. J.*, 2017, **23**(9), 2185–2191.
77 E. M. Bertschler, C. Dietrich, T. Leichtweiß, J. Janek and W. Schnick, Li^+ Ion Conductors with Adamantane-Type Nitridophosphate Anions β-Li10P4N10 and Li13P4N10X3 with X = Cl, Br, *Chem. – Eur. J.*, 2018, **24**(1), 196–205.
78 S. D. Kloß and W. Schnick, Nitridophosphates: A Success Story of Nitride Synthesis, *Angew. Chem., Int. Ed.*, 2019, **58**(24), 7933–7944.
79 W. Schnick, Solid-state chemistry with nonmetal nitrides, *Angew. Chem., Int. Ed. Engl.*, 1993, **32**(6), 806–818.
80 W. Schnick and J. Lücke, Zur Kenntnis von Lithium-phosphor (V)-nitrid. Reindarstellung und Verfeinerung der Kristallstruktur von LiPN2, *Z. Anorg. Allg. Chem.*, 1990, **588**(1), 19–25.
81 W. Schnick and U. Berger, Li10P4N10—A Lithium Phosphorus (v) Nitride Containing the New Complex Anion P4N, *Angew. Chem., Int. Ed. Engl.*, 1991, **30**(7), 830–831.
82 E. M. Bertschler, R. Niklaus and W. Schnick, Reversible Polymerization of Adamantane-type [P4N10] 10− Anions to Honeycomb-type [P2N5] 5− Layers under High-Pressure, *Chem. – Eur. J.*, 2018, **24**(3), 736–742.
83 E. M. Bertschler, R. Niklaus and W. Schnick, Li12P3N9 with Non-Condensed [P3N9] 12−-Rings and its High-Pressure Polymorph Li4PN3 with Infinite Chains of PN4-Tetrahedra, *Chem. – Eur. J.*, 2017, **23**(40), 9592–9599.
84 P. Eckerlin, C. Langereis, I. Maak and A. Rabenau, Über LiPN2, *Angew. Chem.*, 1960, **72**(7–8), 268.
85 R. Marchand, P. L'Haridon and Y. Laurent, Etude cristallochimique de LiPN2: Une structure derivée de la cristobalite, *J. Solid State Chem.*, 1982, **43**(2), 126–130.
86 J. Brice, J. Motte, A. El Maslout and J. Aubry, Synthesis and properties of ternary lithium phosphorus nitride, *C. R. Hebd. Seances Acad. Sci., Ser. C*, 1971, **273**, 744.
87 A. Perret and R. Perrot, Recherches sur le cyanure de lithium, *Helv. Chim. Acta*, 1932, **15**(1), 1165–1171.
88 A. Perret and J. Riethmann, Recherches sur l'équilibre cyanure-cyanamide, dans le cas du lithium, *Helv. Chim. Acta*, 1943, **26**(3), 740–746.
89 M. G. Down, M. J. Haley, P. Hubberstey, R. J. Pulham and A. E. Thunder, Solutions of lithium salts in liquid lithium: preparation and X-ray crystal structure of the dilithium salt of carbodi-imide (cyanamide), *J. Chem. Soc., Dalton Trans.*, 1978, **10**, 1407–1411.
90 M. G. Down, M. J. Haley, P. Hubberstey, R. J. Pulham and A. E. Thunder, Synthesis of the dilithium salt of cyanamide in liquid lithium; X-ray crystal structure of Li 2 NCN, *J. Chem. Soc., Chem. Commun.*, 1978, **2**, 52–53.
91 O. Reckeweg, F. J. DiSalvo, A. Schulz, B. Blaschkowski, S. Jagiella and T. Schleid, Synthesis, Crystal Structure, and Vibrational Spectra of the Anhydrous Lithium Dicyanamide Li[N(CN)2], *Z. Anorg. Allg. Chem.*, 2014, **640**(5), 851–855.
92 O. Reckeweg, M. Conrad, A. Schulz, F. J. DiSalvo and T. Schleid, Synthesis, vibrational spectra and single-crystal structure determination of lithium tricyanomethanide Li [C(CN)3], *Z. Naturforsch. B*, 2018, **73**(3–4), 225–229.
93 J.-H. Her, P. W. Stephens, R. A. Davidson, K. S. Min, J. D. Bagnato and K. van Schooten, *et al.*, Weak Ferromagnetic Ordering of the Li + $[TCNE]^{\bullet-}$ (TCNE = Tetracyanoethylene) Organic Magnet with an Interpenetrating Diamondoid Structure, *J. Am. Chem. Soc.*, 2013, **135**(48), 18060–18063.
94 J. A. Lely and J. M. Bijvoet, The crystal structure of lithium cyanide, *Recl. Trav. Chim. Pays-Bas*, 1942, **61**(4), 244–252.
95 K. Kushida and K. Kuriyama, Origin of direct band gap of Li2CN2 studied by first-principle calculations, *Phys. B*, 2020, **598**, 412442.

96 T. Kimura, C. Hotehama, A. Sakuda, A. Hayashi and M. Tatsumisago, Mechanochemical synthesis and characterization of amorphous Li2CN2 as a lithium ion conductor, *J. Ceram. Soc. Jpn.*, 2019, **127**(8), 518–520.
97 Q. Yang, J. Hu, Z. Yao, J. Liu and C. Li, Durable Li2CN2 Solid Electrolyte Interphase Wired by Carbon Nanodomains via In Situ Interface Lithiation to Enable Long-Cycling Li Metal Batteries, *Adv. Funct. Mater.*, 2022, 2206778.
98 H. Yamane, S. Kikkawa and M. Koizumi, Preparation of lithium silicon nitrides and their lithium ion conductivity, *Solid State Ionics*, 1987, **25**(2–3), 183–191.
99 M. Casas-Cabanas, H. Santner and M. Palacin, The Li–Si–(O)–N system revisited: Structural characterization of Li21Si3N11 and Li7SiN3O, *J. Solid State Chem.*, 2014, **213**, 152–157.
100 H. Yamane, S. Kikkawa and M. Koizumi, High-and low-temperature phases of lithium boron nitride, Li3BN2: Preparation, phase relation, crystal structure, and ionic conductivity, *J. Solid State Chem.*, 1987, **71**(1), 1–11.
101 M. Shigeno, K. Nagao, M. Deguchi, C. Hotehama, H. Kowada and A. Sakuda, *et al.*, New lithium-conducting nitride glass Li3BN2, *Solid State Ionics*, 2019, **339**, 114985.
102 H. Yamane, S. Kikkawa and M. Koizumi, Lithium aluminum nitride, Li3AlN2 as a lithium solid electrolyte, *Solid State Ionics*, 1985, **15**(1), 51–54.
103 K. Cenzual, L. M. Gelato, M. Penzo and E. Parthé, Inorganic structure types with revised space groups. I, *Acta Crystallogr., Sect. B:Struct. Sci.*, 1991, **47**(4), 433–439.
104 J. David, Y. Laurent, J.-P. Charlot and J. Lang, Étude cristallographique d'un nitrure 1 42 53. La structure tétraédrique type wurtzite de Li Si2N3, *Bull. Mineral.*, 1973, **96**(1), 21–24.
105 M. Orth and W. Schnick, Zur Kenntnis von LiSi2N3: Synthese und Verfeinerung der Kristallstruktur, *Z. Anorg. Allg. Chem.*, 1999, **625**(9), 1426–1428.
106 J. Häusler, R. Niklaus, J. Minár and W. Schnick, Ammonothermal Synthesis and Optical Properties of Ternary Nitride Semiconductors Mg-IV-N2, Mn-IV-N2 and Li-IV2-N3 (IV = Si, Ge), *Chem. – Eur. J.*, 2018, **24**(7), 1686–1693.
107 S. Pagano, M. Zeuner, S. Hug and W. Schnick, Single-Crystal Structure Determination and Solid-State NMR Investigations of Lithium Nitridosilicate Li2SiN2 Synthesized by a Precursor Approach Employing Amorphous "Si(CN2)2" (Eur. J. Inorg. Chem. 12/2009), *Eur. J. Inorg. Chem.*, 2009, (12), 1543.
108 J. Lang and J. P. Charlot, System Li_3N-Si3N4, *Rev. Chim. Miner.*, 1970, 7(1), 121–131.
109 R. Juza and W. Schulz, Ternäre Phosphide und Arsenide des Lithiums mit Elementen der 3. und 4. Gruppe, *Z. Anorg. Allg. Chem.*, 1954, **275**(1–3), 65–78.
110 R. Juza, H. H. Weber and E. Meyer-Simon, Über ternäre nitride und oxonitride von elementen der 4. Gruppe, *Z. Anorg. Allg. Chem.*, 1953, **273**(1–2), 48–64.
111 H. Yamane, S. Kikkawa and M. Koizumi, Preparation and electrochemical properties of double-metal nitrides containing lithium, *J. Power Sources*, 1987, **20**(3–4), 311–315.
112 J. David, J. P. Charlot and J. Lang, Double nitrides of lithium and germanium, *Rev. Chim. Miner.*, 1974, **11**(4), 405–413.
113 H. Yamane, S. Kikkawa, H. Horiuchi and M. Koizumi, Structure of a new polymorph of lithium boron nitride, Li3BN2, *J. Solid State Chem.*, 1986, **65**(1), 6–12.
114 F. Pinkerton and J. Herbst, Tetragonal I 4 1/ amd crystal structure of Li 3 BN 2 from dehydrogenated Li-B-N-H, *J. Appl. Phys.*, 2006, **99**(11), 113523.
115 K. Kuriyama, Y. Kaneko and K. Kushida, Synthesis and characterization of AlN-like Li3AlN2, *J. Cryst. Growth*, 2005, **275**(1–2), e395–e399.
116 R. Juza and F. Hund, Die ternären Nitride Li3AIN2 und Li3GaN2. 17. Mitteilung über Metallamide und Metallnitride, *Z. Anorg. Chem.*, 1948, **257**(1–3), 13–25.
117 J. Ding, Q. Wu, Y. Li, Q. Long, Y. Wang and Y. Wang, Li3AlN2—a self-activated yellow light emitting wide-bandgap semiconductor used for LEDs, *J. Am. Ceram. Soc.*, 2017, **100**(4), 1472–1480.
118 H. Yamane, T. Kano, A. Kamegawa, M. Shibata, T. Yamada and M. Okada, *et al.*, Reactivity of hydrogen and ternary nitrides containing lithium and 13 group elements, *J. Alloys Compd.*, 2005, **402**(1–2), L1–L3.
119 G. Goglio, A. Denis, E. Gaudin, C. Labrugère, D. Foy and A. Largeteau, Solvothermal processes for nitride synthesis: examples of Li3GaN2 and graphitic C3N4 elaboration, *Z. Naturforsch. B*, 2008, **63**(6), 730–738.
120 A. P. Purdy, Indium (III) amides and nitrides, *Inorg. Chem.*, 1994, **33**(2), 282–286.
121 R. Niewa, D. A. Zherebtsov and S. Leoni, Li3 [ScN2]: The First Nitridoscandate (III)—Tetrahedral Sc Coordination and Unusual MX2 Framework, *Chem. – Eur. J.*, 2003, **9**(17), 4255–4259.
122 A. P. Palisaar and R. Juza, Ternäre Nitride des Zirkons, Thoriums und Urans, *Z. Anorg. Allg. Chem.*, 1971, **384**(1), 1–11.
123 R. Niewa, H. Jacobs and H. Mayer, Re-evaluation of the crystal structure of lithium zirconium nitride, Li2ZrN2, by neutron powder diffraction, *Z. Kristallogr. – Cryst. Mater.*, 1995, **210**(7), 513–515.
124 R. Niewa, D. Zherebtsov and Z. Hu, Polymorphism of heptalithium nitridovanadate (V) Li7 [VN4], *Inorg. Chem.*, 2003, **42**(8), 2538–2544.
125 D. Vennos and F. DiSalvo, Structure of lithium niobium nitride, *Acta Crystallogr., Sect. C: Cryst. Struct. Commun.*, 1992, **48**(4), 610–612.
126 R. Juza, W. Gieren and J. Haug, Herstellung und Eigenschaften der Ternären Nitride von Vanadin, Niob und Tantal der Zusammensetzung Li_7MeN_4, *Z. Anorg. Allg. Chem.*, 1959, **300**(1–2), 61–71.
127 X. Chen and H. Eick, Synthesis and structure of two new quaternary nitrides: $Li_3Sr_2MN_4$ (M = Nb, Ta), *J. Solid State Chem.*, 1997, **130**(1), 1–8.
128 N. Tapia-Ruiz, M. Segalés and D. H. Gregory, The chemistry of ternary and higher lithium nitrides, *Coord. Chem. Rev.*, 2013, **257**(13–14), 1978–2014.

129 R. Juza, K. Langer and K. Von Benda, Ternary nitrides, phosphides, and arsenides of lithium, *Angew. Chem., Int. Ed. Engl.*, 1968, **7**(5), 360–370.
130 V. K. Tamm, V. Obrosov, N. Batalov, A. Stepanov and Z. Martem'yanova, Electric Properties of Solid Solutions in the Systems Li6MoN4– Li7NbN4 and Li6WN4– Li7TaN4, *Russ. J. Electrochem.*, 2004, **40**(7), 771–775.
131 J. Czochralski, Ein neues verfahren zur messung der kristallisationsgeschwindigkeit der metalle, *Z. Phys. Chem.*, 1918, **92**(1), 219–221.
132 Y. Fujiwara, K. Hoshikawa and K. Kohama, Growth of solid electrolyte LixLa(1−*x*)/3NbO3 single crystals by the directional solidification method, *J. Cryst. Growth*, 2016, **433**, 48–53.
133 T. Swamy, R. Park, B. W. Sheldon, D. Rettenwander, L. Porz and S. Berendts, *et al.*, Lithium metal penetration induced by electrodeposition through solid electrolytes: example in single-crystal Li6La3ZrTaO12 garnet, *J. Electrochem. Soc.*, 2018, **165**(16), A3648.
134 K. Kataoka, H. Nagata and J. Akimoto, Lithium-ion conducting oxide single crystal as solid electrolyte for advanced lithium battery application, *Sci. Rep.*, 2018, **8**(1), 1–9.
135 R. Iwasaki, S. Hori, R. Kanno, T. Yajima, D. Hirai and Y. Kato, *et al.*, Weak anisotropic lithium-ion conductivity in single crystals of Li10GeP2S12, *Chem. Mater.*, 2019, **31**(10), 3694–3699.
136 A. Kumar, S. Dutta, S. Kim, T. Kwon, S. S. Patil and N. Kumari, *et al.*, Solid-State Reaction Synthesis of Nanoscale Materials: Strategies and Applications, *Chem. Rev.*, 2022, **122**(15), 12748–12863.
137 Z. Zhang, Y. Shao, B. Lotsch, Y.-S. Hu, H. Li and J. Janek, *et al.*, New horizons for inorganic solid state ion conductors, *Energy Environ. Sci.*, 2018, **11**(8), 1945–1976.
138 Q. Zhang, D. Cao, Y. Ma, A. Natan, P. Aurora and H. Zhu, Sulfide-based solid-state electrolytes: synthesis, stability, and potential for all-solid-state batteries, *Adv. Mater.*, 2019, **31**(44), 1901131.
139 X. Li, J. Liang, X. Yang, K. R. Adair, C. Wang and F. Zhao, *et al.*, Progress and perspectives on halide lithium conductors for all-solid-state lithium batteries, *Energy Environ. Sci.*, 2020, **13**(5), 1429–1461.
140 C. Wang, J. Liang, J. T. Kim and X. Sun, Prospects of halide-based all-solid-state batteries: From material design to practical application, *Sci. Adv.*, 2022, **8**(36), eadc9516.
141 S. Zhao, Z. Fu and Q. Qin, A solid-state electrolyte lithium phosphorus oxynitride film prepared by pulsed laser deposition, *Thin Solid Films*, 2002, **415**(1–2), 108–113.
142 G. Li, M. Li, L. Dong, X. Li and D. Li, Low energy ion beam assisted deposition of controllable solid state electrolyte LiPON with increased mechanical properties and ionic conductivity, *Int. J. Hydrogen Energy*, 2014, **39**(30), 17466–17472.
143 M. Nisula, Y. Shindo, H. Koga and M. Karppinen, Atomic layer deposition of lithium phosphorus oxynitride, *Chem. Mater.*, 2015, **27**(20), 6987–6993.
144 A. C. Kozen, A. J. Pearse, C.-F. Lin, M. Noked and G. W. Rubloff, Atomic layer deposition of the solid electrolyte LiPON, *Chem. Mater.*, 2015, **27**(15), 5324–5331.
145 H. T. Kim, T. Mun, C. Park, S. W. Jin and H. Y. Park, Characteristics of lithium phosphorous oxynitride thin films deposited by metal–organic chemical vapor deposition technique, *J. Power Sources*, 2013, **244**, 641–645.
146 W. Dai, Y. Qiao, Z. Ma, T. Wang and Z. Fu, All-solid-state thin-film batteries based on lithium phosphorus oxynitrides, *Mater. Futures*, 2022, **1**, 032101.
147 X. Feng, M. Ouyang, X. Liu, L. Lu, Y. Xia and X. He, Thermal runaway mechanism of lithium ion battery for electric vehicles: A review, *Energy Storage Mater.*, 2018, **10**, 246–267.
148 R. Chen, Q. Li, X. Yu, L. Chen and H. Li, Approaching practically accessible solid-state batteries: stability issues related to solid electrolytes and interfaces, *Chem. Rev.*, 2019, **120**(14), 6820–6877.
149 P. Lu, D. Wu, L. Chen, H. Li and F. Wu, Air stability of solid-state sulfide batteries and electrolytes, *Electrochem. Energy Rev.*, 2022, **5**(3), 1–46.
150 X. Chen, Z. Guan, F. Chu, Z. Xue, F. Wu and Y. Yu, Air-stable inorganic solid-state electrolytes for high energy density lithium batteries: Challenges, strategies, and prospects, *InfoMat*, 2022, **4**(1), e12248.
151 W. Li, J. Liang, M. Li, K. R. Adair, X. Li and Y. Hu, *et al.*, Unraveling the origin of moisture stability of halide solid-state electrolytes by *in situ* and *operando* synchrotron X-ray analytical techniques, *Chem. Mater.*, 2020, **32**(16), 7019–7027.
152 Y.-G. Lee, S. Fujiki, C. Jung, N. Suzuki, N. Yashiro and R. Omoda, *et al.*, High-energy long-cycling all-solid-state lithium metal batteries enabled by silver–carbon composite anodes, *Nat. Energy*, 2020, **5**(4), 299–308.
153 S. Lou, F. Zhang, C. Fu, M. Chen, Y. Ma and G. Yin, *et al.*, Interface issues and challenges in all-solid-state batteries: lithium, sodium, and beyond, *Adv. Mater.*, 2021, **33**(6), 2000721.
154 Y. Zhu, X. He and Y. Mo, First principles study on electrochemical and chemical stability of solid electrolyte–electrode interfaces in all-solid-state Li-ion batteries, *J. Mater. Chem. A*, 2016, **4**(9), 3253–3266.
155 Y. Zhu, X. He and Y. Mo, Origin of outstanding stability in the lithium solid electrolyte materials: insights from thermodynamic analyses based on first-principles calculations, *ACS Appl. Mater. Interfaces*, 2015, **7**(42), 23685–23693.
156 S. Jacke, J. Song, G. Cherkashinin, L. Dimesso and W. Jaegermann, Investigation of the solid-state electrolyte/cathode LiPON/LiCoO2 interface by photoelectron spectroscopy, *Ionics*, 2010, **16**(9), 769–775.
157 R. Shimizu, D. Cheng, J. L. Weaver, M. Zhang, B. Lu and T. A. Wynn, *et al.*, Unraveling the Stable Cathode Electrolyte Interface in all Solid-State Thin-Film Battery Operating at 5 V, *Adv. Energy Mater.*, 2022, **12**(31), 2201119.
158 A. Schwöbel, R. Hausbrand and W. Jaegermann, Interface reactions between LiPON and lithium studied by in-situ X-ray photoemission, *Solid State Ionics*, 2015, **273**, 51–54.

159 D. Cheng, T. A. Wynn, X. Wang, S. Wang, M. Zhang and R. Shimizu, *et al.*, Unveiling the stable nature of the solid electrolyte interphase between lithium metal and LiPON via cryogenic electron microscopy, *Joule*, 2020, **4**(11), 2484–2500.

160 Z. D. Hood, X. Chen, R. L. Sacci, X. Liu, G. M. Veith and Y. Mo, *et al.*, Elucidating interfacial stability between lithium metal anode and Li phosphorus oxynitride via in situ electron microscopy, *Nano Lett.*, 2020, **21**(1), 151–157.

161 J. Su, M. Pasta, Z. Ning, X. Gao, P. G. Bruce and C. R. Grovenor, Interfacial modification between argyrodite-type solid-state electrolytes and Li metal anodes using LiPON interlayers, *Energy Environ. Sci.*, 2022, **15**(9), 3805–3814.

162 C. Wang, G. Bai, Y. Yang, X. Liu and H. Shao, Dendrite-free all-solid-state lithium batteries with lithium phosphorous oxynitride-modified lithium metal anode and composite solid electrolytes, *Nano Res.*, 2019, **12**(1), 217–223.

163 T. Wu, W. Dai, M. Ke, Q. Huang and L. Lu, All-Solid-State Thin Film μ-Batteries for Microelectronics, *Adv. Sci.*, 2021, **8**(19), 2100774.

164 S.-H. Lee, P. Liu and C. E. Tracy, Lithium thin-film battery with a reversed structural configuration SS/Li/Lipon/$Li_xV_2O_5$/Cu, *Electrochem. Solid-State Lett.*, 2003, **6**(12), A275.

165 D.-L. Xiao, J. Tong, Y. Feng, G.-H. Zhong, W.-J. Li and C.-L. Yang, Improved performance of all-solid-state lithium batteries using LiPON electrolyte prepared with Li-rich sputtering target, *Solid State Ionics*, 2018, **324**, 202–206.

166 S. Shiraki, H. Oki, Y. Takagi, T. Suzuki, A. Kumatani and R. Shimizu, *et al.*, Fabrication of all-solid-state battery using epitaxial LiCoO2 thin films, *J. Power Sources*, 2014, **267**, 881–887.

167 D. Ruzmetov, V. P. Oleshko, P. M. Haney, H. J. Lezec, K. Karki and K. H. Baloch, *et al.*, Electrolyte stability determines scaling limits for solid-state 3D Li ion batteries, *Nano Lett.*, 2012, **12**(1), 505–511.

168 Y. S. Park, S. H. Lee, B. I. Lee and S. K. Joo, All-Solid-State Lithium Thin-Film Rechargeable Battery with Lithium Manganese Oxide, *Electrochem. Solid-State Lett.*, 1998, **2**(2), 58.

169 C. Yada, A. Ohmori, K. Ide, H. Yamasaki, T. Kato and T. Saito, *et al.*, Dielectric modification of 5V-class cathodes for high-voltage all-solid-state lithium batteries, *Adv. Energy Mater.*, 2014, **4**(9), 1301416.

170 D.-R. Shi, J. Fu, Z. Shadike, M.-H. Cao, W.-W. Wang and Z.-W. Fu, All-Solid-State Rechargeable Lithium Metal Battery with a Prussian Blue Cathode Prepared by a Nonvacuum Coating Technology, *ACS Omega*, 2018, **3**(7), 7648–7654.

171 F. Huang, Z.-W. Fu and Q.-Z. Qin, A novel $Li_2Ag_{0.5}V_2O_5$ composite film cathode for all-solid-state lithium batteries, *Electrochem. Commun.*, 2003, **5**(3), 262–266.

172 H. Xu, Y. Li, A. Zhou, N. Wu, S. Xin and Z. Li, *et al.*, Li_3N-modified garnet electrolyte for all-solid-state lithium metal batteries operated at 40 °C, *Nano Lett.*, 2018, **18**(11), 7414–7418.

173 Y. Niu, Z. Yu, Y. Zhou, J. Tang, M. Li and Z. Zhuang, *et al.*, Constructing stable Li-solid electrolyte interphase to achieve dendrites-free solid-state battery: A nano-interlayer/Li pre-reduction strategy, *Nano Res.*, 2022, 1–10.

174 A. Kızılaslan and H. Akbulut, Assembling All-Solid-State Lithium–Sulfur Batteries with Li_3N-Protected Anodes, *ChemPlusChem*, 2019, **84**(2), 183–189.

175 Q. Cheng, A. Li, N. Li, S. Li, A. Zangiabadi and W. Huang, *et al.*, Stabilizing solid electrolyte-anode interface in Li-metal batteries by boron nitride-based nanocomposite coating, *Joule*, 2019, **3**(6), 1510–1522.

176 A. Baniya, A. Gurung, J. Pokharel, K. Chen, R. Pathak and B. S. Lamsal, *et al.*, Mitigating interfacial mismatch between lithium metal and garnet-type solid electrolyte by depositing metal nitride lithiophilic interlayer, *ACS Appl. Energy Mater.*, 2022, **5**(1), 648–657.

177 H. Wan, Z. Wang, W. Zhang, X. He and C. Wang, Interface design for all-solid-state lithium batteries, *Nature*, 2023, **623**(7988), 739–744.

178 H. Wan, B. Zhang, S. Liu, Z. Wang, J. Xu and C. Wang, Interface Design for High-Performance All-Solid-State Lithium Batteries, *Adv. Energy Mater.*, 2024, 2303046.

179 Y. Li, Y. Wu, Z. Wang, J. Xu, T. Ma and L. Chen, *et al.*, Progress in solvent-free dry-film technology for batteries and supercapacitors, *Mater. Today*, 2022, **55**, 92–109.

180 F. Zhao, Q. Sun, C. Yu, S. Zhang, K. Adair and S. Wang, *et al.*, Ultrastable anode interface achieved by fluorinating electrolytes for all-solid-state Li metal batteries, *ACS Energy Lett.*, 2020, **5**(4), 1035–1043.

181 L. Ye and X. Li, A dynamic stability design strategy for lithium metal solid state batteries, *Nature*, 2021, **593**(7858), 218–222.

182 G. Liu, W. Weng, Z. Zhang, L. Wu, J. Yang and X. Yao, Densified Li6PS5Cl nanorods with high ionic conductivity and improved critical current density for all-solid-state lithium batteries, *Nano Lett.*, 2020, **20**(9), 6660–6665.

183 H. Zheng, S. Wu, R. Tian, Z. Xu, H. Zhu and H. Duan, *et al.*, Intrinsic lithiophilicity of Li–garnet electrolytes enabling high-rate lithium cycling, *Adv. Funct. Mater.*, 2020, **30**(6), 1906189.

184 R. Dubey, J. Sastre, C. Cancellieri, F. Okur, A. Förster and L. Pompizii, *et al.*, Building a Better Li-Garnet Solid Electrolyte/Metallic Li Interface with Antimony, *Adv. Energy Mater.*, 2021, 2102086.

185 D. H. Tan, Y. S. Meng and J. Jang, Scaling up high-energy-density sulfidic solid-state batteries: A lab-to-pilot perspective, *Joule*, 2022, **6**, 1755–1769.

186 J. Schnell, T. Günther, T. Knoche, C. Vieider, L. Köhler and A. Just, *et al.*, All-solid-state lithium-ion and lithium metal batteries–paving the way to large-scale production, *J. Power Sources*, 2018, **382**, 160–175.

187 C. Wang, R. Yu, H. Duan, Q. Lu, Q. Li and K. R. Adair, *et al.*, Solvent-free approach for interweaving freestanding and ultrathin inorganic solid electrolyte membranes, *ACS Energy Lett.*, 2021, **7**(1), 410–416.

188 W. D. Richards, L. J. Miara, Y. Wang, J. C. Kim and G. Ceder, Interface stability in solid-state batteries, *Chem. Mater.*, 2016, **28**(1), 266–273.

189 S. Wang, Q. Bai, A. M. Nolan, Y. Liu, S. Gong and Q. Sun, *et al.*, Lithium Chlorides and Bromides as Promising Solid-State Chemistries for Fast Ion Conductors with Good Electrochemical Stability, *Angew. Chem., Int. Ed.*, 2019, **58**(24), 8039–8043.

190 Y. Zhang, X. He, Z. Chen, Q. Bai, A. M. Nolan and C. A. Roberts, *et al.*, Unsupervised discovery of solid-state lithium ion conductors, *Nat. Commun.*, 2019, **10**(1), 5260.

191 Y. Zhu and Y. Mo, Materials design principles for air-stable lithium/sodium solid electrolytes, *Angew. Chem., Int. Ed.*, 2020, **59**(40), 17472–17476.

192 Y. Xiao, L. J. Miara, Y. Wang and G. Ceder, Computational screening of cathode coatings for solid-state batteries, *Joule*, 2019, **3**(5), 1252–1275.

193 H. Luo, H. Wang, Z. Bi, D. M. Feldmann, Y. Wang and A. K. Burrell, *et al.*, Epitaxial ternary nitride thin films prepared by a chemical solution method, *J. Am. Chem. Soc.*, 2008, **130**(46), 15224–15225.

194 H. T. Chiu, S. H. Chuang, G. H. Lee and S. M. Peng, Low-temperature solution route to molybdenum nitride, *Adv. Mater.*, 1998, **10**(17), 1475–1479.

195 H. Luo, Y. Lin, H. Wang, J. H. Lee, N. A. Suvorova and A. H. Mueller, *et al.*, A chemical solution approach to epitaxial metal nitride thin films, *Adv. Mater.*, 2009, **21**(2), 193–197.

196 D. M. Hoffman, Chemical vapour deposition of nitride thin films, *Polyhedron*, 1994, **13**(8), 1169–1179.

197 F. Wang, C. Xue, H. Zhuang, X. Zhang, Y. Ai and L. Sun, *et al.*, Growth and characterization of the InN film ammonification technique, *Phys. E*, 2008, **40**(3), 664–667.

198 H. Wang, J. Li, K. Li, Y. Lin, J. Chen and L. Gao, *et al.*, Transition metal nitrides for electrochemical energy applications, *Chem. Soc. Rev.*, 2021, **50**(2), 1354–1390.

199 S. Kalnaus, N. J. Dudney, A. S. Westover, E. Herbert and S. Hackney, Solid-state batteries: The critical role of mechanics, *Science*, 2023, **381**(6664), eabg5998.

200 X. Ke, Y. Wang, G. Ren and C. Yuan, Towards rational mechanical design of inorganic solid electrolytes for all-solid-state lithium ion batteries, *Energy Storage Mater.*, 2020, **26**, 313–324.

201 M. J. Wang, E. Kazyak, N. P. Dasgupta and J. Sakamoto, Transitioning solid-state batteries from lab to market: Linking electro-chemo-mechanics with practical considerations, *Joule*, 2021, **5**(6), 1371–1390.

202 F. P. McGrogan, T. Swamy, S. R. Bishop, E. Eggleton, L. Porz and X. Chen, *et al.*, Compliant yet brittle mechanical behavior of Li2S-P2S5 lithium-ion-conducting solid electrolyte, *Adv. Energy Mater.*, 2017, **7**(12), 1602011.

203 J. F. Nonemacher, Y. Arinicheva, G. Yan, M. Finsterbusch, M. Krueger and J. Malzbender, Fracture toughness of single grains and polycrystalline Li7La3Zr2O12 electrolyte material based on a pillar splitting method, *J. Eur. Ceram. Soc.*, 2020, **40**(8), 3057–3064.

204 J. Bates, N. Dudney, B. Neudecker, A. Ueda and C. Evans, Thin-film lithium and lithium-ion batteries, *Solid State Ionics*, 2000, **135**(1–4), 33–45.

205 J. Li, C. Ma, M. Chi, C. Liang and N. J. Dudney, Solid electrolyte: the key for high-voltage lithium batteries, *Adv. Energy Mater.*, 2014, **5**(4), 1401408.

206 E. G. Herbert, W. E. Tenhaeff, N. J. Dudney and G. Pharr, Mechanical characterization of LiPON films using nanoindentation, *Thin Solid Films*, 2011, **520**(1), 413–418.

207 S. Kalnaus, A. S. Westover, M. Kornbluth, E. Herbert and N. J. Dudney, Resistance to fracture in the glassy solid electrolyte Lipon, *J. Mater. Res.*, 2021, **36**, 787–796.

